Physical Modelling of CO_2-Cyclic Solvent Inject in post-CHOPS reservoirs

by

Daniel Felipe Cartagena-Perez

A thesis submitted in partial fulfillment of the requirements for the degree of

Master of Science

in

GEOTECHNICAL ENGINEERING

Department of Civil and Environmental Engineering

University of Alberta

Abstract

This thesis looks for modelling physically the cyclic solvent injection as enhanced oil recovery (EOR) technique used in unconsolidated heavy oil reservoirs, particularly those subjected to Cold Heavy Oil Production with Sands (CHOPS) methods. CHOPS reservoirs are characterized by their low recovery factors (5-15%) due to the challenges posed by unconsolidated sand formations, high sand and water production rates, and limited reservoir energy. The geomechanics of CHOPS reservoirs involve the formation of high-permeability channel-like structures known as wormholes, resulting from sand production during production operations. These geomechanical characteristics contribute to challenges such as reservoir compaction, sand control issues, and formation collapse. In the other hand, the presence of those wormholes limits the applicability of some EOR techniques due to their low efficiency.

This thesis comprises four interconnected papers that address critical aspects of reservoir engineering, geotechnical experimentation, and material characterization to overcome these challenges and provide a set of tools to model the post-CHOPS reservoirs in an experimental environment with the use of a geotechnical centrifuge for physical modelling.

The approach used in this thesis is mainly experimental, aiming to provide tools and materials that enable further investigation into post-CHOPS reservoirs. To achieve a comprehensive understanding of post-CHOPS reservoirs, which present multiple challenges (e.g., geomechanical conditions, sand production, and the presence of wormholes), a new geotechnical centrifuge cell was designed, manufactured, assembled, commissioned, and tested. This new cell has the capability to induce an anisotropic stress state at 30 times Earth's gravity while producing through a central wellbore connected to wormholes. The experiment also involves the use of foamy oil. Additionally, to achieve a better representation of poorly cemented reservoirs, this thesis presents a new procedure to 3D print rocks, along with the mechanical and hydraulic characterization of this material.

The results show that the developed geotechnical centrifuge worked effectively in all its components. Radial flow was confirmed using well testing techniques, and an anisotropic stress state was imposed on the sample, validating the applicability of this new cell. At the same time, the 3D-printed rocks developed in this thesis demonstrated similar elastic parameters to some poorly cemented reservoirs. These rocks exhibited degradation of strength and stiffness with long exposure to canola oil, stability under isotropic creep tests, permeability within the range for Western Canada reservoirs, and an even distribution of the binder.

Thus, this thesis presents two novel contributions to the study of reservoir geomechanics: (i) a new geotechnical centrifuge cell with triaxial stress capabilities and radial flow, and (ii) a new 3D-printed material that emulates poorly cemented reservoirs. Additionally, the reviews include some field cases of CO_2-CSI (Cyclic Solvent Injection) that have never been presented in the technical literature, and the potential applications for the geotechnical centrifuge in reservoir engineering as a programmatic aspiration.

Preface

This thesis is an original work by Daniel Cartagena Pérez. Parts of the research work have been submitted or are ready for journal or conference submission as follow:

- Cartagena-Pérez, D., Rangriz-Shokri, A., Zambrano, G., & Chalaturnyk, R. (2024). Mechanical and Hydraulic Characterization of 3D Printed Rock Analogues of Poorly Cemented Sandstone. *58th US Rock Mechanics/Geomechanics Symposium*. Golden, Colorado: American Rock Mechanics Association - ARMA.
- Cartagena-Pérez, D., Rangriz-Shokri, A., Zambrano, G., Pantov, D., Wang, Y., Chalaturnyk, R., & Hawkes, C. (2024). Scaled Physical Modeling Of Cyclic CO2 Injection In Unconsolidated Heavy Oil Reservoirs Using Geotechnical Centrifuge And Additive Manufacturing Technologies. *SPE Canadian Energy Technology Conference and Exhibition*. Calgary, Alberta: Society of Petroleum Engineers
- Cartagena-Pérez, D. F., Rangriz-Shokri, A., Zambrano–Narvaez, G., Pantov, D., Wang, Y., Hawkes, C., & Chalaturnyk, R. (2023). Geotechnical Centrifuge Modeling of Multiphase Flow and Geomechanics Aspects in Shallow Unconsolidated Heavy Oil Reservoirs. *Gussow*. Banff, Alberta.
- Cartagena-Pérez, D., Rangriz-Shokri, A., Zambrano–Narvaez, G., Pantov, D., Wang, Y., Hawkes, C., & Chalaturnyk, R. (2023). Investigation of Geomechanical Issues during CO2 Injection in CHOPS Reservoirs using a Geotechnical Centrifuge. *EOR Technical Collaboration Program*. Calgary, Alberta.
- Cartagena-Pérez, D., Rangriz Shokri, A., Zambrano, G. & Chalaturnyk, R. (2023). Scaled Physical Modeling of CO_2 Cyclic Injection Process in A Heterogeneous Unconsolidated Sandstone Formation using Additive Manufacturing and Geotechnical Centrifuge Technologies. 15th Annual International Conference on Porous Media. Edinburgh.
- Cartagena-Pérez, D., Rangriz Shokri, A., Pantov, D., Wang, Y., Zambrano, G., Hawkes, C., & Chalaturnyk, R. (2023). *Geotechnical Centrifuge Modeling of CO_2 EOR in CHOPS Reservoirs*. GeoConvention 2023. Calgary.

For all each of those works and the present thesis, I have developed the ideas, standard operation procedudures, commissioned of sensors and mechanisms, carried out of the test, data collection, methodologies, analysis of results, validation, visualization, manuscript composition, implementation of the reviews, and presentation in the conferences.

The present and myself as author have been awared during the present graduate studies with the following distintion:

- Graduate Student Research Excellence Award
- FGSR Travel Award
- InterPore2023 Conference Grant
- Geoconvention 2023 Student Travel Assistance
- GSA Academic Travel Grant

- Mitac Accelerate Program Grant

Dedication

To Bach for keeping me alive

To Kant for keeping me human

Suelo. Nada más
Suelo. Nada menos.
Y que te baste con eso.
Porque en el suelo los pies hincados,
en los pies torso derecho,
en el torso la testa firme,
y allá, al socaire de la frente,
la idea pura, y en la idea pura
el mañana, la llave
—mañana— de lo eterno.
Suelo. Ni más ni menos.
Y que te baste con eso.

-Pedro Salinas

[Ground. Nothing more.
Ground. Nothing less.
Make do with it.
Because your feet are nailed to it
and your torso to them
and on the torso a firm head
and there to the lee of one's brow
the pure thought and in the pure thought
the morrow, the key
– the morrow – of the eternal.
Ground. Neither more nor less.
Make do with it.]

Acknowledgement

The author gratefully acknowledges Dr. Chalaturnyk and Dr. Zambrano for their invaluable technical support and, most importantly, their trust since our first meeting at the remote geomechanics symposium in Medellín.

I would also like to express sincere gratitude to Dr. Rangriz Shokri for his tireless efforts during our weekly meetings. His guidance was instrumental in accelerating this project. I appreciate his belief in our results.

I am also thankful for the technical support provided by members of the Reservoir Geomechanics Research Group at the University of Alberta. I extend special recognition to the staff at GeoCERF facilities for their contributions of expertise and knowledge to this work.

This research was partially funded by Mitacs through the Mitacs Accelerate program. We are grateful to the Heavy Oil Research Network program, managed by the Petroleum Technology Research Centre, Regina, for providing additional financial support. We also acknowledge the NSERC/Energi Simulation Industrial Research Chair in Reservoir Geomechanics in Unconventional Resources for their funding contribution. I extend my sincere gratitude to all our funders for their generosity and ongoing support.

Contents

List of Figures

List of Tables

Chapter 1

Introduction

Cold heavy oil production with sand (CHOPS) is a primary recovery technique, characterized by intentional massive production of sands with heavy oil. This creates high permeable areas or channel-like structures, i.e. wormholes, around the wellbore and in the reservoir that allow the production of heavy oil that otherwise would not be produced due to its high viscosity. The production of oil in CHOPS wellbores stops when the amount of water and sand production makes it unprofitable. Unfortunately, the primary recovery with CHOPS is low, demanding follow-up enhanced oil recovery (EOR) techniques at the post-CHOPS stage of the reservoir.

At this stage of the reservoir's life, the CHOPS reservoir has wormholes (or dilated zones) with higher porosity and permeability compared to the rock matrix. This contrast in permeability makes the implementation of any fluid-displacement-based EOR techniques (e.g. waterflooding or gas flooding) inefficient, simply because the displacing fluid will tend to flow through the higher permeability zones and it results in poor sweeping efficiency. To overcome this issue, the cyclic solvent injection (CSI) process has been proposed in the literature. In CSI, a solvent (e.g. CO_2) is injected into the well, followed by a soaking period; the wellbore is then opened and the fluids around the wellbore are produced.

The implementation of CSI-based post-CHOPS requires an understanding of the flow regime, the impact of preexisting wormholes at the time of the CSI, the impact of the solvent in the rheology of the reservoir fluid, and the influence of the geomechanics constraints in the behavior of the rock and sand production. To understand the complex interplaying of these factors, physical modelling of a CHOPS prototype in the centrifuge environment can help to capture and honor most of the flow and geomechanics parameters involved in the CSI in post-CHOPS reservoirs. This tool provides the researchers with the capability of emulating the same flow regime around a wellbore (i. e. radial flow around a wellbore) and a similar stress regimen than the one existing at the reservoir (Stress anisotropy), these two conditions are qualitatively similar to the ones in actual reservoirs.

Statement of the problem

The physical modelling of the post-CHOPS reservoir that are subjected to CSI demands an effort to better capture the flow and geomechanical issues that are expected for CHOPS reservoirs. The main challenge is how we can obtain a physical and mechanical representation of the post-CHOPS reservoirs at a laboratory condition that are qualitatively similar to the ones at reservoir conditions. The conditions that the physical modelling can help are listed below:

1. Honoring the stress state and stress anisotropy,
2. Including the presence of preexisting wormholes in the reservoir,
3. Mixture of oil with the solvent leads to complex behavior as the foamy oil (i.e. the suspension of bubbles throughout the viscous oil),
4. Good representation of the reservoir rock in terms of its mechanical, petrophysical, and hydraulic properties (e. g. Young's modulus, UCS, porosity, permeability, among others)
5. Capability to reproduce the rock to obtain multiple identical samples, enabling unbiased analysis caused by rock heterogeneity,
6. Radial flow (as opposed to linear flow) around the wellbore to better emulate the conditions of flow and sand production at reservoir scale.

Research Objectives

To address these multiple challenges, we need a comprehensive physical representation of the post-CHOPS reservoir. In this thesis, the objective is to enable experimental study of the CSI process in CHOPS reservoirs using geotechnical centrifuge and additive manufacturing technology (3D printing of rocks with actual sand grains). The objective of this thesis is closely linked with the six challenges that were identified for the physical modeling of post-CHOPS reservoirs. The work considers the design of an experimental set up for the centrifuge environment and analogue rocks to allow the physical modelling of the CSI-based post-CHOPS process, honoring the reservoir boundary conditions in the laboratory environment. Note that the optimization of the CSI processes in post-CHOPS reservoirs is not in the scope of work. Moreover, this study develops a set of experimental tools and procedures for an improved understanding of the fundamental geomechanical aspects of the cyclic solvent injection in poorly cemented rocks.

Scope and methodology

The scope of this research includes the design, commissioning, and test of a brand-new centrifuge cell with the capability of inducing an anisotropic stress state while spinning at hyper gravity environment (e.g. 30 Gs). The new centrifuge cell is capable to manage multiphase fluid flow and sand production, one of its kind in Canada and elsewhere. Additionally, a novel procedure to 3D print rocks is employed that replicates the behavior of poorly cemented rocks; this is an alternative to manufacture the physical models and CHOPS reservoir prototype. In this way, the present thesis offers two solutions: i) to build a tool (geotechnical centrifuge cell) and ii) to obtain a material that replicates the poorly cemented reservoirs.

To achieve the research objective, the following methodology based on scopes and their activities was used in this thesis:

- Scope 1: To build a new cutting-edge centrifuge cell
    - Review the use of geotechnical centrifuge in reservoir engineering.
    - Design the new centrifuge cell.
    - Manufacture a new centrifuge cell. This activity was done by a third machine shop
    - Assemble the new centrifuge cell.
    - Commission of the different mechanisms and sensing parts of the new centrifuge cell at 1G.
    - Commission the test at 30Gs
    - Test a rock with wormholes to emulate the CO_2-CSI in post-CHOPS reservoirs.
- Scope 2: To obtain a material that replicates the poorly cemented reservoirs:
    - 3D print samples at low binder saturation.
    - Characterize it physically with CT scans and thin sections.
    - Characterize the new material mechanically with UCS, triaxial test, and isotropic creep tests.
    - Measure the permeability of the samples at high confining stress.
    - Compare the main petrophysical and mechanical parameters with those for the most representative oil reservoirs in Western Canada.

Thesis Outline

This document is a paper-based thesis. Four papers, presented at different reputable peer-reviewed conferences, and submitted to different journal publications comprise the main chapters of the thesis. Each chapter has its own introduction, literature survey, conclusions, and references. At the end, a list of appendices is provided where the procedural aspects of the experiments are treated with more detail.

In chapter 1, the work that was developed is introduced with its methodology and scopes. In chapter 2, a review of the CO_2-CSI in post CHOPS reservoirs is presented. Its intention is to provide the reader with a physical understanding of rock, fluids, and geomechanics at different scales that involves in the modeling of CSI process. In chapter 3, a review of the use of the geotechnical centrifuge in reservoir engineering is conducted. Also, the perspectives and opportunities of employing this centrifuge tool are pointed out, trying to take some experience in civil engineering and showing their similarity to some of challenges encountered in petroleum and reservoir engineering applications. This chapter looks for closing a gap in the use of the centrifuge tool while providing the reader with the basic physics associated with the physical modelling process using a geotechnical centrifuge. These two papers compose the block of reviews of the current thesis.

In the second block, chapter 4 presents GeoTriax, the new geotechnical centrifuge cell with imposing triaxial stress capabilities. This paper illustrates how the main mechanisms of the centrifuge cell operate. It also describes the procedure and results of one test that was carried out at 30Gs and emulated the CSI in a post-CHOPS reservoir. As a sample, a 3D printed rock with wormholes was used. It also shows all the analysis about production, pressure, flow regime, and geomechanics derived from this test. It must be highlighted that in the best knowledge of the authors, this is one of the first centrifuge cell that is capable to apply a triaxial stress condition in a cylindrical sample while having a whole system to remotely open a wellbore and allow the fluid production. At the same time, this is the first time that a well testing analysis is done in a drainage area replicated at a centrifuge laboratory using scaling-up laws of the geotechnical centrifuge.

Chapter 5 describes the process to obtain a 3D printed rock that emulates the mechanical and hydraulic behavior of poorly cemented heavy oil reservoirs, as observed in the Western Canada. This chapter summarizes the centrifuge tool (GeoTriax) and the sample (3D printed rocks at low binder saturation) that enable us to physically model the complex and fascinating process of the CO_2-CSI in post-CHOPS reservoirs while honoring more realistic boundary conditions, compared to the core flood tests in 1 G environment.

Finally, a set of appendix that contain the standard operational procedure, and the summary of the tests that went wrong is presented.

Finally, to facilitate the view of the reader, the following table summarizes the main structure of this thesis.

Table 1. Summary of the thesis

Chapter	Topic	Type
1	Review of the CO_2-CSI post-CHOPS technique	Review
2	Use of the geotechnical centrifuge in petroleum reservoir engineering	Review
3	Presentation and description of the GeoTriax. Results of test of physical modelling of the post-CHOPS reservoir subjected to CO2-CSI	Research

4	Description of the process to obtain a 3D printed rock that emulated poorly cemented sandstones and its characterization	Research

Chapter 2

Recent Developments of Cyclic Solvent Injection Process to Improve Oil Recovery From Unconsolidated Heavy Oil Reservoirs

A version of this chapter was accepted for presentation at the SPE Conference at Oman Petroleum & Energy Show, Muscat (Oman), 22–24 April 2024.

2.1. Abstract

One of the practical limitations of cold heavy oil production with sand (CHOPS) method in unconsolidated reservoirs is the very low recovery factor (5-15%). To target the remaining 85-95% heavy oil resources, several enhanced oil recovery (EOR) techniques such as cyclic solvent injection (CSI) have been proposed. Due to its potential success in Canada and elsewhere, this paper reviews the technical and efficiency requirements of CSI EOR in post- CHOPS heavy oil reservoirs.

To have an improved understanding of the conditions that result in a successful CSI process, we evaluated the dominant driving mechanisms of CSI at reservoir conditions such as fluid displacement, pressure gradients, non-equilibrium gas dissolution/exsolution, potential formation collapse, and deformation issues; the focus is on the application of CO_2 as a solvent. Limitations of current thermal and non-thermal EOR methods were compared against the CSI in thin oil reservoirs. To complete the assessment, several case studies and lessons learned from CSI applications were included based on the latest laboratory experiments, numerical studies, in addition to the CSI pilot/field tests.

Specific to thin and shallow heavy oil reservoirs with sand production (e.g. CHOPS), the key to recover incremental oil was found to re-energize depleted reservoirs in a cyclic manner, aiming to provide more drive energy by economical gaseous solvents (e.g. CO_2). It was realized that other EOR techniques such as waterflooding, gas flooding, and steam injection can face major issues with flow and heat efficiencies, including fingering and significant heat/solvent losses; this makes CSI a feasible EOR alternative. Regarding the solvent use, laboratory experiences have not been conclusive about what solvent stream could result in an improved oil recovery; however, most of solvents should be designed to either reduce

heavy oil viscosity, or strengthen the nucleation and stability of the injected solvent bubbles in the heavy oil reservoir (i.e. foamy oil behavior). To this end, successful field scale CO_2 EOR applications have been reported in several post-CHOPS oil reservoirs. Although progress has been made, numerical modelling still faces challenges to properly model the main CSI driving mechanisms, including fluid-solvent interaction and deformation of subsurface reservoirs. Moreover, field implementation indicates that highly productive wells during primary production from unconsolidated reservoirs might also outperform during a follow up CSI process.

This work addresses the recent improvements in application of CSI EOR to develop heavy oil reservoirs, especially for thin and poorly consolidated sandstones that were subject to CHOPS. The findings of this paper, including the limitations and requirements of different recovery techniques, enable more effective design of field scale CO_2 EOR operation in depleted heavy oil reservoirs.

Keywords

Cyclic Solvent Injection, Heavy Oil Reservoirs, Enhanced Oil Recovery (EOR), CO2, Field Scale CO_2 EOR, Unconsolidated Reservoirs.

2.2. Introduction

Heavy oil resources continue to show a significant demand in the global energy market. Despite a decline in energy consumption due to the COVID-19 pandemic, fossil fuels (i.e. oil and gas) remain dominant players, accounting for 55.9% of the global primary energy market [1]. Heavy oil production is still essential for some countries, such as Canada. The Canada Energy Regulator [2] reported that heavy oil exports have played a major role in Canada's export participation. In 2020, the total volume of heavy oil export was estimated at 2.81 million barrels per day, with 90% of Canada's heavy oil, originating from Alberta's heavy oil reservoirs, which amounted to 2.53 million barrels per day.

The Lloydminster area, which straddles Alberta and Saskatchewan, represents a key area in the energy framework of Canada [3]. The western region of Canada is estimated to contain a total of 5201 million m^3 of heavy oil resources. Given the abundance of such resources and the unceasing energy demand, it is imperative to employ innovative techniques to recover these resources from the subsurface. Notably, approximately 80% of heavy oil reservoirs in the Western Canada are less than 5 meters thick [4]. For instance, in the Lloydminster area, around 95% of the oil reserves are found within sands with a maximum thickness of 10 meters, highlighting the significant proportion of oil located in thin and medium-thick reservoirs (Fig 2-1).

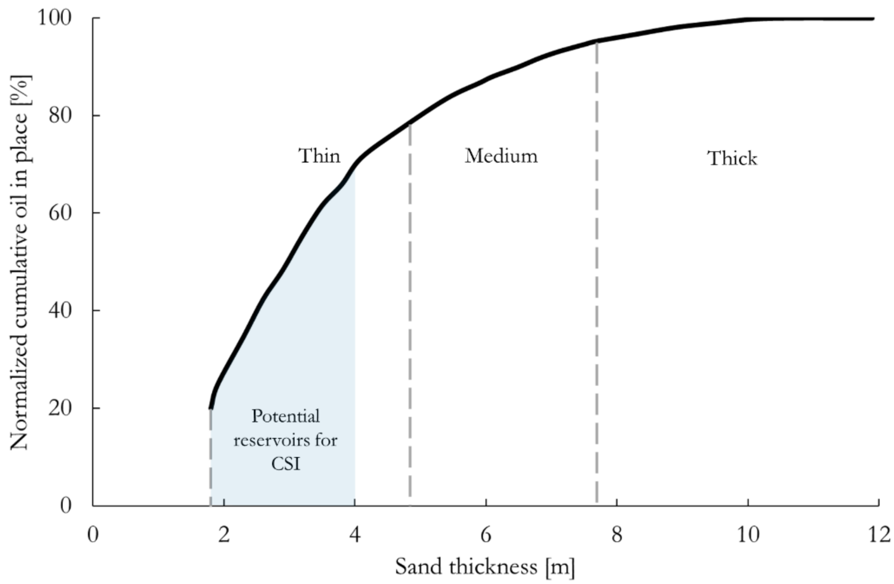

Fig 2-1. Estimated distribution of oil in place vs sand thickness in the Lloydminster area. Modified after [5].

According to Dusseault [6], a typical Canadian heavy oil reservoir is composed of quarzose sand zones with porosities ranging from 28% to 32%, an average connate water saturation of 25%, and permeabilities between 1 to 4 Darcies. The viscosities of heavy oil in such reservoirs vary from 500 to 50,000 cp, while the oil API gravity ranges from 10° to 16° [3]. Despite the high permeability of these unconsolidated reservoirs, the oil properties pose significant challenges for fluid production. A summary of the typical properties of Canadian CHOPS reservoirs is provided by [7] in Table 2-1.

Table 2-1. Typical properties of Canadian CHOPS reservoirs, modified after [7]

Property	Value
Depth (m)	480
Net pay (m)	5
Porosity (%)	33
Permeability (darcies)	2 to 4
Oil saturation (%)	80
Initial reservoir pressure (kPa)	2750
Reservoir temperature (°C)	20
Dead-oil viscosity (cp)	25000
Formation compressibility (kPa^{-1})	$5x10^{-6}$
Wormhole radius (m)	0.05

2.3. Recovery Techniques in Thin Unconsolidated Heavy Oil Reservoirs

Due to its high viscosity, production from heavy oil reservoirs requires additional driving mechanisms than only fluid expansion with pressure drawdown. The theoretical relationship between viscosity and flow velocity is established by the Darcy law:

$$v = -\frac{k}{\mu}\frac{dP}{dx} \tag{2-1}$$

where v is the Darcy velocity, k is the permeability of the porous media, μ is the fluid viscosity, and dP/dx is the pressure gradient. From (2-1), $v \propto \mu^{-1}$ which mean that higher viscosity is detrimental to fluid flow. Here, fluid viscosity is basically defined as the fluid resistance to flow. A decrease in oil viscosity, an enhancement in formation permeability, or an increase in viscous forces and pressure gradient can be achieved through fluid and sand production, fluid injection such as waterflooding, steam assisted gravity drainage, polymer flooding, in-situ combustion, and solvent-based recovery techniques (e.g. vapex - vapor extraction), among others.

2.3.1. Cold Production with Sand

CHOPS (Cold Heavy Oil Production with Sand) is a primary heavy oil recovery technique that involves the deliberate initiation and continuous sand production to significantly increase the permeability of the target formation. In this technique, the low rock consolidation (very common in heavy oil reservoirs with unconsolidated/poorly cemented sandstones and friction angle of 15°) is used to detach the grain from the formation matrix by the action of viscous forces and effective stresses to increase oil production [6]. Some authors have noted that the sole action of viscous forces is not sufficiently large to detach the sand grains [8].

Compared to other recovery techniques, CHOPS is a relatively low-cost technology because it does not require any fluid injection (increase in heat, pressure, or add diluents). Most authors agree that CHOPS can achieve a recovery factor of 5% to 15% by the end of its primary production lifetime [9]-[11]. Field experience in the Lloydminster area also suggests an average recovery of 8% of the original oil in place for CHOPS reservoirs [3]. This provides a potential to recover the remaining 90% oil in place through follow up enhanced oil recovery techniques, such as CO_2 injection. However, the design of a successful CO_2 injection process to re-energize CHOPS reservoirs requires an understating of fluid flow and geomechanical issues that govern the behavior of deformable heavy oil reservoirs.

Table 2-2 summarizes the main recovery mechanisms in thin unconsolidated heavy oil formations; some of major recovery mechanisms will be further described in the next section.

Table 2-2. Production Mechanisms of CHOPS based on [6].

Mechanism	Description
Gravitational forces	The most direct effect of gravity is the weight of the overlanding rock layers and soil strata (vertical stress) that might have impacts on yielding and dilation.
Pressure gradient	Large viscous forces help oil and sand flow towards the production well
Foamy oil behaviour	Systematic nucleation of dissolved gas and non-equilibrium release of gas bubbles causes fluid expansion, but a continuous gas phase is not formed due to high oil viscosity. The mixture of oil and dispersed gas bubbles also improves the fluid and sand production.
Sand production	The influx of sand into the wellbore (either continuously or in batches) improves the permeability of the reservoir; fluid and sand are lifted to the surface using progressive cavity pumps.
Wellbore skin	Potential cavities, created around the wellbore during CHOPS, reduce the wellbore skin by mechanical action since any blockage, for instance due to the precipitation of asphaltenes, fine-grained particles, or mineral deposits, is removed.

Foamy Oil Behaviour. Due to high oil viscosity (order of 10000 – 25000 cp), the formation of dispersed gas bubbles is one of the main flow characteristics and drive forces in CHOPS [6],[7]. Foamy oil drive mechanism has been extensively studied in the literature [12]-[16]. Fig 2-2 illustrates a sequence of images from a fluid depletion experiment in which a 2D view of the heavy oil sample, saturated with gas, was subject to fluid depletion at a rate of 300 kPa/min from 1200 kPa to 100 kPa. Fig 2-2 visualizes the non-equilibrium nature of the foamy oil drive; the released gas bubbles initially do not form a single gas phase, and remain dispersed in the oil which causes significant fluid expansion; compare the total fluid column with respect to the initial oil level, depicted by red line.

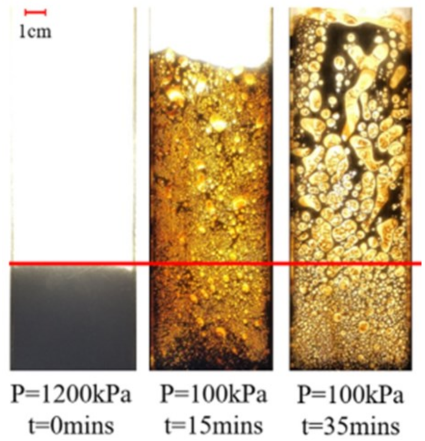

Fig 2-2. Pictures of the behavior of foamy oil, modified after [17].

Wang et al. [17] described the evolution of the foamy oil in three main stages: i) expansion, ii) peaking, and iii) decay. Basically, the bubbles within the foamy oil expand during depletion and push the oil out of the reservoir. Some authors noted the dependency of foamy oil on the magnitude of the pressure depletion rate (e.g. [18]). The strength of foamy oil behavior and depletion rate in heavy oil has direct impact on the established pore pressure during fluid production phase. It is also worth mentioning that a lower pressure drop could lead to a more lasting foamy oil peak and declining phases. Fig 2-3 shows a visual microscale confirmation of fluid flow through porous media due to foamy oil driving mechanism [19].

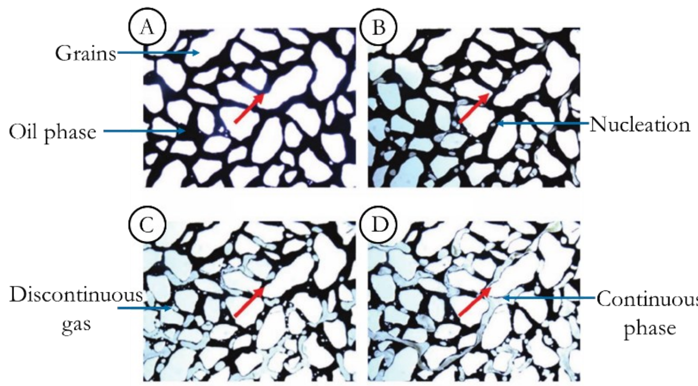

Fig 2-3. Foamy oil within porous medium. The red arrow shows the Flow direction. a) oil phase flow at 6.2MPa, b) and c) foamy oil flow at 5.0 MPa and 3.8 MPa respectively, c) a continuous gas phase is evident. Modified after [19]. A similar experiment is carried out by [14]

Formation of High Permeability Channels. Wormhole in the context of heavy oil and sand production refers to a zone in which there is no grain-to-grain contact [6]; that lack of contact between grains translates into high porosity and permeability channels [20]. The formation of high permeability channels (i.e. wormhole network) has a few advantages.

First, since wormholes have a higher permeability, it is a preferential route for the fluid flow from the inner reservoir to reach to the wellbore. If this feature is described in terms of pressure, the wormhole network can be understood as an isobaric line within the reservoir [7]. It means, that the high permeability of wormhole network creates the condition in which fluid can flow at low pressures. Fig 2-4 shows the pressure distribution during depletion of a reservoir that contains wormholes (represented through numerical multi-lateral wells). Dark blue color represents low pore pressures, imposed as the bottomhole pressure constraint, and it is transmitted throughout the geometry of the wormholes within the reservoir. Such pressure distributions could be confirmed by well testing [21]-[23].

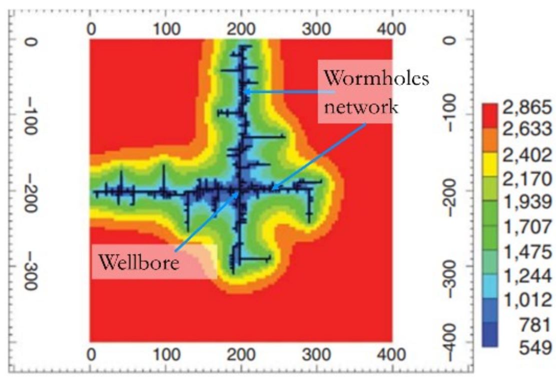

Fig 2-4. Pressure distribution for a reservoir with wormholes during depletion. Modified after [7]

Second, the wormhole network enhances the productivity and injectivity qualities of the reservoir; in the context of fluid injection processes, such as CSI, the injection performance is strongly improved. Additionally, creation of high-permeability channels increases the fluid access and contact area of the injected fluid within reservoir compared to the case when a fluid is injected into an intact reservoir.

In the context of petroleum geomechanics, the growth of the wormhole network is governed by the yielding of the sandstone [6],[24]. Due to the loss of confining stress as a result of the non-grain contact state in the cavity zone, the radial stress σ_r decreases while the tangential stress σ_θ increases. Fig 2-5 shows a stress state diagram as a function of the radial distance into a reservoir with a cavity. The shear stress increases because the difference between the radial and tangential stresses is higher until the yielding is reached. Experimental studies have shown that under anisotropic stress state, the wormholes tend to grow in the direction of the lower horizontal stress [25].

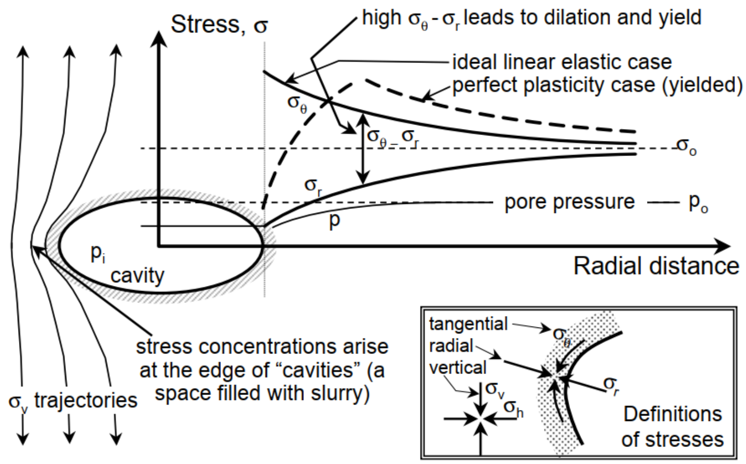

Fig 2-5. Stress state around a cavity. Taken from [6]

Those geomechanical phenomena result in an increase in porosity due to the removal of mass (i.e. sand grains) in a constant bulk volume. Table 2-3 shows the porosity estimations based on data and reported measurement in the literature.

Table 2-3. Experimental observation of increase in porosity due to sand production

#	Reference	Initial Porosity [%]	Final porosity [%]
1	[26] –Sandstone low density	36.31	85.61
2	[26] –Max. density of 1860 kg/m3	36.31	79.86
3	[26] – Experiment 2, Low density sandstone density	31.03	71.85
4	[26] – Experiment 2, max density of 1860 kg/m3	31.03	70.65
5	[26] – Experiment 3, max density of 1860 kg/m3	31.03	85.47
6	[26] – Experiment 3, max density of 1860 kg/m3	31.03	83.86
7	[27] – Silica well sorted	41.08	57.30
8	[27] – Silica poorly sorted	32.2	41.65
9	[27] – Silica well sorted 2	40.82	53.87
10	[27] – Silica no fine fraction	38.4	48.6
11	[27] – Husky field	38.2	62
12	[28] *	20.56	60
13	[29]	21.80	52.99
14	[30]	37	46
15	[31] *	32	60

16	[20] ξ	32	52
	Mean	33.18	63.23
	Standard Deviation	5.69	14.01

* Used for numerical modelling; ξ results obtained from history matching

A look at the CHOPS literature suggests an average initial porosity of 38.13% (standard deviation of 3.5%) for different sandstones. The final porosity has an average of 51.67% (a standard deviation of 9.2%). Similarly, some authors have noted an increase in the formation permeability due to sand production from 3 to 67 Darcies [27],[32].

2.3.2. Waterflooding in Heavy Oil Reservoirs

Although the most common practice for heavy oil and bitumen recovery are thermal techniques [4], the costs associated with steam generation, greenhouse gas emission, and upgrading facilities may affect the viability of thermal EOR projects. This makes viscosified waterflooding an alternative for some heavy oil reservoirs [33]. In waterflooding process, the viscosity difference between injected water and in-situ oil often creates adverse mobility ratios with a negative impact on oil recovery factor and sweep efficiency [33]. The mobility ratio can be described as follows:

$$M = \frac{\lambda_{displacing\ phase}}{\lambda_{displaced\ phase}} = \frac{k_{rw}}{k_{ro}} \frac{\mu_o}{\mu_w} \tag{2-2}$$

where M is the mobility ratio, λ is the mobility of the phase, $k_{rw,o}$ are the relative permeabilities of water or oil, and $\mu_{w,o}$ is the viscosity of water or oil. From equation (2-2), it is apparent that if $\mu_o \gg \mu_w$ then $M \gg 1$, a condition that leads to fingering where fully water-saturated channels connects the injection and production wells [34], bypassing oil in the pore space, and ultimately leading to poor oil recovery; further phenomenal explanation can be found in the work of [35]. Fig 2-6 shows an early breakthrough due to fingering that can be experienced in heavy oil reservoirs.

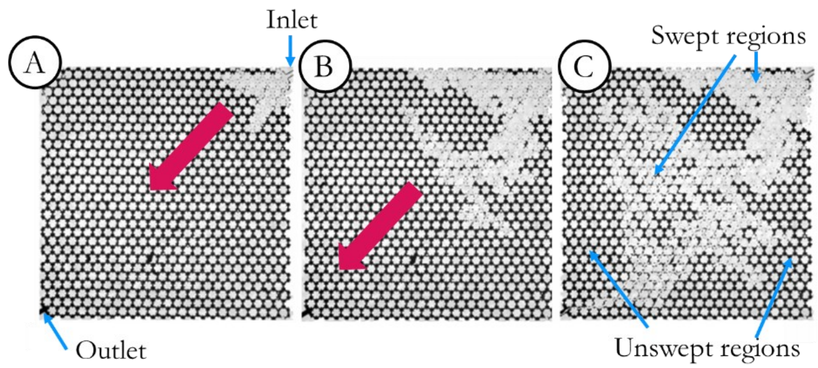

Fig 2-6. Displacement of the front of water and fingering effect. Modified after [33]. A) displacement time equal to 120 s, b) displacement time equal to 360 s, and c) displacement time equal to 720s. The dark pink arrow shows the direction of the flow.

2.3.3. Thermal EOR in Heavy Oil Reservoirs

The most applicable thermal EOR technique for heavy oil in Canada is steam-assisted gravity drainage (SAGD). SAGD involves the use of a pair of parallel horizontal wells for the injection of steam into the reservoir. This is intended to reduce the heavy oil viscosity by heating the oil using the latent heat of steam in the reservoir. Reduction in oil viscosity is the main reason behind all variations of thermal EOR methods, such as steam flooding, and cyclic steam stimulation (CSS). Table 3 is based on [4] who conducted numerical simulations to compare the efficiency of various thermal EOR techniques; they compared the thermal EOR results with cold production without sand in thin reservoirs (<10 m).

Table 2-4. Performance of SAGD vs. cold production recovery techniques in thin reservoirs, after [4]

Case	**Operating time (year)**	**Cumulative oil production (m^3)**	**cEOR (GJ/m^3)**	**Recovery factor (%)**
Cold production	5	406	0	0.5
SAGD	4	30194	32.9	37.3

The simulation results revealed an adverse cumulative energy-oil ratio (cEOR), which is a measure of energy input required to produce a unit volume of oil. An economically reasonable cEOR is typically around 10 GJ/m^3, corresponding to a cumulative steam-oil ratio (cSOR) of 4 m^3/m^3 [4]. The simulations showed high cEOR (three times larger than typical values) can be attributed to high heat loss to underburden and overburden formations in thin formations (less than 10 m thick). In a 10 m thick reservoir, heat loss was calculated to be 10%, while in a thinner reservoir of 4 m, the heat loss increased by 40%.

Considering the limitations of waterflooding and thermal techniques in thin unconsolidated heavy oil formations, the implementation of follow up recovery methods such as Cyclic Solvent Injection (CSI) has been proposed to improve the recovery from heavy oil reservoirs.

2.4. Cyclic Solvent Injection Process

Cyclic solvent injection process is intended to target the large amounts of oil, remained in the reservoir through solvent diffusion. CSI technique is applied when either the reservoir is too thin (<10m) for thermal EOR methods, or heavy oil is too viscous to cause adverse mobility ratio during flooding process. Specific to CHOPS reservoirs, solvent access to the reservoir can be through high permeability channels and taking advantage of its high contact area with reservoir [36]. The CSI technique can also be thought of as an in-situ upgrading technology because it changes the composition and properties of the heavy oil at reservoir conditions [37]. The CSI involves alternating between solvent injection, soaking, and oil production phases, using a variety of solvents such as CH_4, CO_2, alkali metal silicide, among others [38].

During the injection phase, the wellbore is used to inject the solvent or mixture of solvents into the heavy oil reservoir. This phase results in an increase of the pore pressure around the wellbore and reduction of the effective stress as an immediate consequence. In field practice, the injection is applied until the initial pressure of the reservoir is reached; but in some instances, the injection can go beyond initial reservoir pressure [5].

The injection phase is followed up by a soaking period in which the wellbore is shut in. The soaking phase is a critical step to dissipate the pore pressure and to allow the slow process of solvent diffusion occur within the heavy oil reservoir. Solvent diffusion can permanently reduce the oil viscosity. In Table 2-5, viscosity on Lloydminster's oil varies from 7600 mPa at 20°C to 2000 mPa due to the application of propane as diluent (i.e. a viscosity reduction of 74%). A similar response is observed on Athabasca where bitumen's viscosity changes from 700000 mPa.s at 20°C to 80-100000 mPa.s after the application of toluene.

Table 2-5. Oil Properties and Their Change after Solvent Treatment. Taken from [37]

Oil	Crude oil properties		Solvent	Dissolving conditions			Dissolved oil properties			References
	μ (mPa.s)	ρ (g/m^3)		T (°C)	P (kPa)	Mixture rate (%)	μ (mPa.s)	ρ (g/m^3)	Viscosity reduction rate	
Lloydminster	7600 (20 °C)	0.979 (16 °C)	propane	20	100		2000		0.75	R.M. Butler and I.J.Mokrys, 1998
Athabasca	148–27.9 (104 °C –148 °C	1.1014–0.990 (90 KPa, 10 °C –50 °C)	propane	10 –90	863–7934	5.2–26.1	8.6–223	0.791 –0.953		A.Badamchi-Zadeh et al., 2009
			propane and CO_2	10 –25	3309 –5110	propane 13.5 CO_2 11.0	21.9–49.4	0.904 –0.920		A.Badamchi-Zadeh et al., 2009
				10 –25	2716	propane 24 CO_2 6.2	11.6–23.7	0.840 –0.856		
Cold Lake/ Lloydminster	70,000 (20 °C)		ethane	15	100–2600	0.3–0.6	80–10000		0.86–0.89	T.W.J Frauenfeld et al., 2002
			propone	15	100–600	0.3–0.65	20–10000		0.98–0.99	
Athabasca bitumen	700,000 (20 °C)		toluene	20	100	50–100	2000–100000		0.85–0.99	IGOR J. Mokrys and Roger M. Bulter, 1989
Frog Lake	18,600 (21.6 °C)		butane	20	120–200	55–80	8–140		0.99	Ali Yazdani and Brij B. Maini, 2007
Du84, Liaohe	400,000 (60 °C)		toluene	60	100	2–20	291.8 –215,000		0.25–0.99	Wei Li, 2013
			diesel	60	100	2–20	960–258,000		0.1–0.99	
Gao3624, Liaohe	600 (50 °C)		CO_2	50	100		150		0.78	Hongmei Zhang, 2002
Fengcheng, Xinjiang	21,584 (25.6 °C)	0.984 (25.6 °C)	propane	23	905		4362		0.80	Yanhong Li, 2014

Once the soaking period has allowed the interaction between the injected solvent and heavy oil to occur for a sufficient time, the wellbore is opened to production. A mixture of in situ fluids (both water and oil with solvent) is produced. The production stage lasts until the oil rate becomes uneconomical, or the costs of water management gets unacceptable [5].

A comparison of CSI with a continuous solvent injection is done in Table 2-6

Table 2-6. Differences between continuous and cyclic solvent injection, modified after [39].

	Continuous solvent injection	**Cyclic solvent injection**
Operation Strategy	Two types: Vapex and Lateral SVX	Huff – n- puff
Driving Mechanisms	▪ Gravity (Traditional Vapex) ▪ Constant pressure may apply for lateral SVX	▪ Gravitational forces ▪ Pressure gradient ▪ Foamy oil flow ▪ Sand influx ▪ Reduction of skin
EOR Mechanisms	▪ Viscosity reduction ▪ Asphaltene precipitation ▪ Diffusion and dispersion based mass transfer	▪ Viscosity reduction ▪ Asphaltene precipitation ▪ Diffusion and dispersion based mass transfer

	▪ Capillarity mixing	▪ Capillary mixing ▪ Foamy oil
Rules of wormholes	Establish communication between the injector and the producer. They may cause solvent quick breakthrough	Increase contact area for solvent and crude oil. Help the diluted oil flow to the producer
Main challenges	▪ Low mass transfer rate ▪ Small gravity head (For thin-net pay reservoirs)	▪ Pressure depletion ▪ Viscosity regains
Geomechanics implications	▪ Continuous decrease of the effective stress and tensional failure ▪ Stability of the wormholes	▪ Cyclic loading and fatigue of the rock. ▪ Stability of the wormholes

To analyze further details about CSI and CO_2 as solvent, the following part of this review will be split into three sections: Experimental approach, field pilot projects and experiences; and modeling and numerical descriptions.

2.4.1. Recent CSI Experimental Studies

Coskuner et al. [3], explored how different solvents (e.g. heptane, distillate) may help to achieve a higher recovery factor. The general laboratory procedure was to place saturated rock samples with oil inside glass container, and add hot water and solvent. This experimental process was done in multiple time steps to emulate the cyclic nature of solvent injection. Experimental data suggested recovery factors ranging from 42% to 88%; it is very likely that these high recovery factors will not be achieved in field application of solvent injection. In these experiments, the solvent was in contact with all faces of the submerged rock sample, and the complexity of fluid flow regimes, dispersion, reservoir heterogeneity, and limited access to huge amount of solvents at reservoir conditions were not considered.

The impact of some of the characteristics of physical model (reservoir volumes, wormholes and high-permeability channels, and their spatial location within the reservoir) was addressed by [39] using an experimental design. To capture the possible effects, [39] varied the diameter of the test sample, the position of the wormholes, and the vertical and horizontal orientations of the sample. Their experimental results showed the impact of reservoir-wormhole geometry, the length and relative positions of the wormholes with respect to the reservoir limits on the final oil recovery factor. They concluded that the presence of longer high-permeability channels and wormholes is effective in delivering solvent to access the lower-permeability portion of the reservoir; this provides increased access for solvent to dilute heavy oil in the reservoir matrix and ultimately increases oil recovery factor in shorter time. This means that the in such geological settings, higher permeability zones and wormholes not only improve the total recovery, but also increases the oil rate in production phase [39]. This was also confirmed through visual inspection of the sample during experiments where lower oil saturation near high-permeability zone suggested more oil production.

Although Du et al. [39] used a broad range for their experimental study, further analysis is required to understand the impact of observed cavities in unconsolidated sandstone reservoirs, changes in in-situ stresses and heterogeneities during cyclic loading/unloading of solvent injection process. These geometries have been experimentally shown to induce different flow regimes that may impact the final recovery [26].

In addition to the impact of the reservoir discontinuities, other empirical works are available in the literature that focus on the driving mechanisms during cyclic solvent injection. In [11], the impact of parameters such as gravity, pressure depletion rate, solvent composition, and initial oil saturation are studied. The tests were conducted on the oil from Cold Lake formation and CH_4 was injected into the samples subject to primary production. The follow up CSI process was done in the sand pack at low pressure (2.76 MPa); the sand pack was scanned before the primary production and after the end of each cycle of solvent injection to obtain fluid saturation profiles. The experiments showed the bubble nucleation and foamy oil behaviour as the key driving mechanisms. From linear decrease in pressure and low gas-oil ratio at the beginning of the test, the expansion of the fluid in response to the drawdown was found to mainly contribute to oil production. Once the sample reached the bubble point, the recovery factor was improved with the foamy oil flow in which the dispersed gas bubbles helped to maintain the sample pressure for an extended time. It seems that the first cycle of each test was the one with the highest impact on recovery factor because the main driving forces (especially foamy oil behaviour) were strongly active during the first cycle, when no continuous gas phase was present. Similar observations have also been observed at field scale.

The composition and type of solvent stream for CSI are other highly-debated topics in the literature. For EOR applications in heavy oil reservoirs, solvent type is sometimes selected based on the intended recovery mechanisms. For instance, a reservoir may benefit from activating foamy oil drive while reduction of oil viscosity is a priority for another EOR project. As a result, a wide diversity exists on the type of solvent to meet specific EOR requirements in different regions. Cost of solvent is another issue to be considered for the success of CSI process. In current literature, popular gaseous solvents are methane, propane, carbon dioxide, or a combination of them.

Huerta et al. [40] proposed to take advantage of some produced gases like CO_2 and H_2S; in some fields, a stream of CO_2 and H_2S (known as acid gas) is a usual production sub-product, but they pose operational challenge in terms of management and safety, so disposal of CO_2 and H_2S in geological formations is a more common practice than their use for EOR purposes. [40] studied the impact of cyclic injection of acid gas on oil recovery factor through a set of experiments where multiple tests are carried out with two cycles. They used pure CO_2 solvent (as reference), CO_2 72%-CH_4 28%, CH_4 70%-C_3H_8 30%, and CO_2 90%-H_2S 10%. The experimental results showed that a combination of CO_2 and H_2S offers a better performance than pure CO_2 or any methane/propane mixture. Mixtures of CO_2 and propane showed the best results in terms of oil recovery. An interesting observation was that regardless of the solvent composition, all the experiments confirmed that most of oil recovery is achieved through the first cycle. This observation has been reported in other different experimental studies and field tests.

In a more detailed experimental design, [36] used a 1.5 m long sand-pack sample to study solvent injection and key parameters related to fluid expansion, gas dissolution and foamy oil behaviour using a combination of gaseous solvents including methane, propane, and carbon dioxide. Soh et al. [36] observed that some gases can function as "mainly diluents" to reduce oil viscosity while other gases can act as "foamy helpers" to provide the right conditions to establish foamy oil flow. Previously, [40] suggested that the mixture of methane/propane could be a good performer to increase oil recovery. However, the results from [36], specifically for heavy oil reservoir, implied that solvents with noticeable mixing properties (e.g. propane) are not recommended to be used with the solvents that aid the formation of foamy oil (e.g. CH_4 or CO_2). This might suggest that the type and concentration of solvent is case specific to the heavy oil reservoir and that laboratory experiments are required to understand the interaction of solvent-heavy oil at reservoir pressure and temperature before conducting any CSI field test.

The physical modelling of the post-CHOPS CSI has recently found a new dimension with the use of geotechnical centrifuge to model the drainage area of heavy oil reservoirs. [41] developed a geotechnical centrifuge cell that allows the integration of triaxial stresses with 3D printed samples that contained wormholes. The results of this work, highlight the pivotal role that geomechanics has during the post-CHOPS phase of the reservoir when CSI is applied.

2.4.2. Recent Development in Numerical Modeling of CSI

Most of literature on modeling CSI process in unconsolidated heavy oil reservoirs have focused their effort on two main topics, namely i) numerical modelling of solvent-heavy oil interactions that includes foamy oil behaviour and non-equilibrium dissolution/exsolution processes, and ii) numerical modeling of wormholes and high-permeability channels within the reservoir after cold production with sand.

Proper representation of the dissolution/exsolution process seems to directly impact the numerical evaluation of CSI performance in heavy oil reservoirs [42]. In general, the non-equilibrium behavior for the gas dissolution into heavy oil can be described as:

$$SG \rightarrow SG + SL \tag{2-3}$$

Where SG is the solvent in gaseous phase, SL is the solvent in liquid phase. Similarly, the dissolution at non-equilibrium behavior is represented as:

$$SG + SL \rightarrow 2SL \tag{2-4}$$

Non-equilibrium can be thought of as a delay in the gas dissolution/exsolution process, compared to equilibrium phase behaviour in which dissolved gas could releases into free phase, for instance due to pressure depletion at an instant. The modeling can be achieved through multiple Arrhenius kinetic reaction types of modeling for release of dissolved gas, to dispersed gas, to free gas. [42] compared the impact of non-equilibrium and instant equilibrium phase behaviour on the solubility for CSI process for a solvent mixture of CO_2 and propane (Table 2-7). They reported significant differences in oil recovery, solvent recovery, and solvent-to-oil ratio (Fig 2-7). Non-equilibrium phase behaviour resulted in larger bottomhole pressures and higher cumulative oil production. The observed differences were explained through the advection, diffusion, dispersion, and dissolution of non-equilibrium mixing process.

Table 2-7. Comparative impact of non-equilibrium and instant equilibrium simulation of the solubility. Taken from [42]. Simulations are run for a CSI process with solvent of 72%CO2 and 28% propane.

	Cumulative oil (cm^3)	**Propane recovery (%)**	**Carbon dioxide recovery (%)**	**Net solvent/Oil ratio (liquid cm^3/cm^3)**
Nonequilibrium	1698	72.8	64.1	0.60
Instant Equilibrium	809	92.3	97.4	0.34

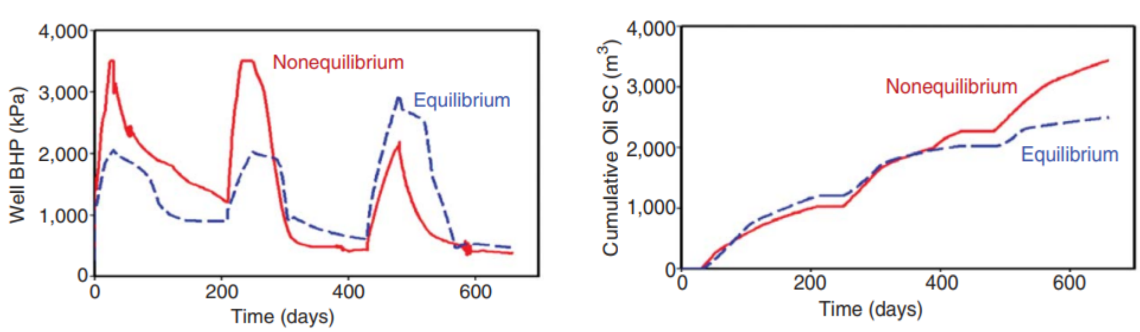

Fig 2-7. bottom hole pressure (left) and cumulative oil (right) vs. time on the CSI process with non-equilibrium and instant equilibrium. Taken from [42]

In addition to modelling of solvent-heavy oil interactions, it is important that the modeling tools are capable to include, and history match the presence of wormholes and high-permeability zones with field data during cold heavy oil production phase; this step is required prior to numerically simulating the CSI process [42]. Different modeling approaches are presented in the literature. Rivero et al. [43] suggested the use of an effective permeability model that represents the wormholes and high-permeable zones. Rangriz Shokri et al. [44] used partial dual-permeability models, in which the matrix represents the intact reservoir, and the fractures represent the wormhole domain. Haddad et al [45] employed dilated-zone model with wormholes and cavities represented as dilated zones around the wellbore. In a numerical study, Chang et al. [42] illustrated that the selected method to represent the reservoir and high-permeability zones affects the cumulative oil production and recovery factor, predicted for primary production and follow-up EOR scenarios.

In summary, large-scale simulation of CSI scenarios in heavy oil reservoirs could face many other numerical challenges, including longer simulation run times, difficulty to model sand production and wormhole growth, and upscaling issues of the laboratory results when foamy oil behavior from bulk fluid phase (e.g. PVT cell) is used to represent foamy oil flow in the porous media (e.g. [44],[46],[29]). Given the range of these modeling uncertainties, numerical simulations are still required to assess and optimize the performance of CSI process in unconsolidated heavy oil reservoirs [32], [47]-[49]. Optimization parameters for the CSI process include type and concentration of solvents, injection rate and pressure, duration of injection, soaking, and production phases, number of cycles, and incremental oil production per cycle. Available literature on numerical simulation of CSI also suggests highest oil recovery in the early cycles and a general reduction tend in cumulative oil production in the subsequent cycles (Fig 2-8); this is consistent with previous laboratory experiments and field tests (e.g. [50]).

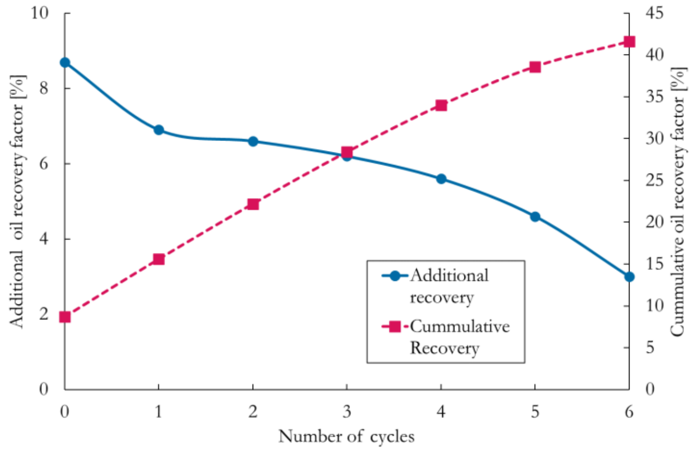

Fig 2-8. A declining trend in incremental oil recovery factor with the number of CSI cycles, modified after [49]

2.4.3. Recent CSI Pilot Projects and Case Studies

In this section, field cases from the Lloydminster area, Canada, will be described with emphasis on some CHOPS wells from the following reservoirs: Nexen Plover Lake, Husky Mervin, Devon Manatokan East, and Husky Lashburn. Our focus is on the application of gaseous hydrocarbon solvents and CO_2. However, CSI projects that employed other gases, such as nitrogen are also available in literature [51].

Overall, the performance of CSI in an unconsolidated heavy oil reservoir is closely related to its primary production history of that reservoir; this due to the fact that large volumes of sand might have been produced with oil during primary production and that affect the creation of high permeability regions and wormholes within the reservoir. Fig 2-9 illustrates the typical behavior of a CHOPS well in Lloydminster area. Initial production begins with an increase in oil and sand production rates; the reason to allow some sand production along with heavy oil is to increase oil rate and to accelerate production. With more production, sand production significantly declines; the oil is produced until the water production makes oil recovery from that particular well uneconomical [5]. During the primary production, compaction of unconsolidated formation and other geomechanical issues are responsible for 30% of the production drive energy.

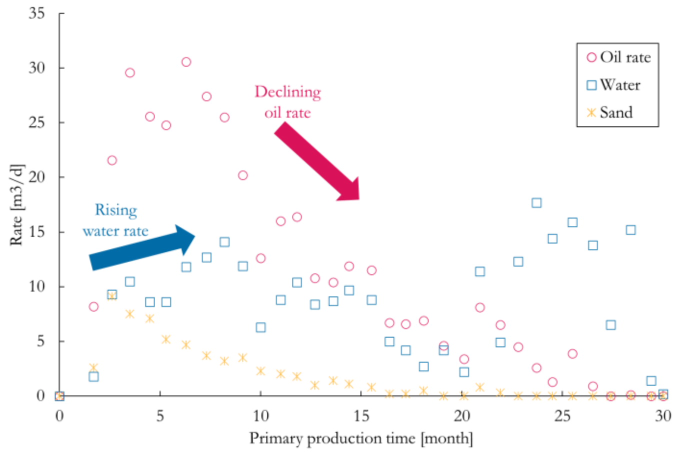

Fig 2-9. Typical production behavior from a CHOPS well at the Lloydminster area. Modified after [5]

Case Study of the Nexen Plover Lake. In this field project, a propane-based CSI was applied. The wellbore experienced high water rate and low oil production prior to the first cycle; this has made the production from this well uneconomical. The injection of propane during CSI was sufficient to increase the oil rate six times the pre-CSI rate. It was reported that most of the injected propane was recovered from the produced reservoir fluids [5]. This retrieval of solvent added to the economic viability of the project. It is worth to mention that one of the key challenges that determines the economic success of CSI field implementation is the high cost of solvents and existence of the possibility to retrieve back the injected solvents. During CSI process, a reduction in oil viscosity was observed due to the use of injected propane in the reservoir [5]. A direct consequence of this oil viscosity reduction was a decrease in the water cut that resulted from an improved mobility ratio.

A description of the production record is shown in Fig 2-10.

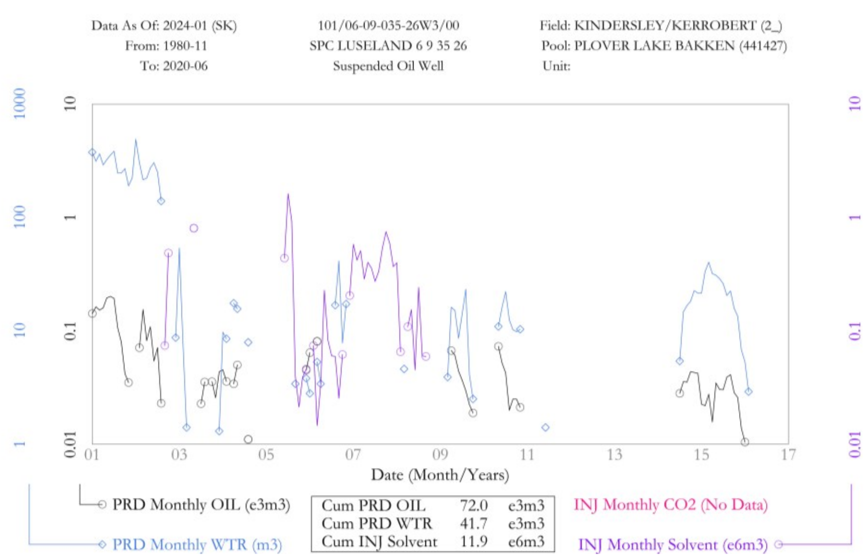

Fig 2-10. Production record of Nexen Plover Lake 3-9.

Case Study of the Husky Edam. This project employed a combination of methane-propane injection. The oil recovery during the primary production is 11000 m^3, and after the first 5 cycles of CSI, an additional 5500 m^3 oil could be produced; this translates to 50% of the initial oil recovery [5]. Each CSI cycle has resulted in high oil rate that declined with time during production phase [5]. The field observation suggested that the water cut decreased not only just within each cycle, but also showed a decreasing general trend over a total of 5 cycles. This was believed to be due to continuous change in heavy oil properties (e.g. viscosity) caused by the solvents that positively affected the mobility ratio. Further research is required to address wettability alteration in the reservoir because of solvent use during the CSI process. Recently, there is evidence of multiple cycles of CO_2 injection (Since 2019) with a total injection of almost 5.3 x 10^6 m^3 of CO_2, showing the transition in the solvents.

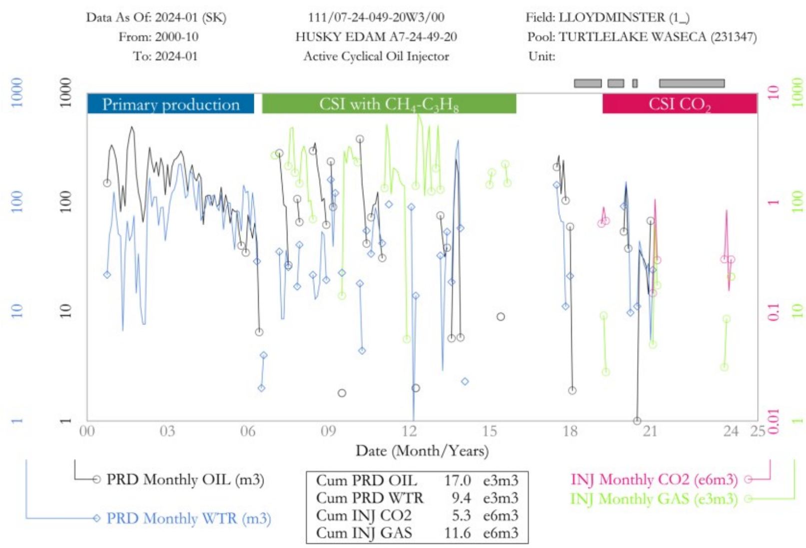

Fig 2-11. Production record for Waseca 7A-24 on the Husky Edam.

Case Study of the Husky Mervin. This pilot project is of special interest, because of the CO_2 use. The first well (Mervin 05-36) injected pure CO_2 in the first two cycles (Fig 2-12). The primary recovery of this well was 11700 m^3; the recovery improvement during the first and the second cycles of a follow up CSI operation was over 14% and 10% of the primary recovery, respectively. From the same reservoir, another well (Mervin 15-01 Colony - Fig 2-13) presented a different response to the application of CSI. This well had a higher primary oil production of about 51000 m^3 (4.4 times higher than the Mervin 05-36); this probably indicates a more developed network of wormhole and high permeability channels due to sand production. The CSI process added incremental oil production about 60% of the primary recovery in the first cycle, and 73% in the second cycle. The high recovery factor observed during the CSI cycles suggests that a productive CHOPS well may potentially perform better during CSI operation [5]. This could be associated with larger reservoir contact area to solvents (e.g. extended wormhole network and high permeability channels due to sand influx) that had been created during primary production. A third case (Mervin 12-31) offered insights on the impact of CSI on water cut (Fig 2-14). The well was productive with a primary recovery of 59000 m^3, but with a high water cut of 80% [5]. The high water cut was observed in all the CSI cycles which might be interpreted as a limited action of the injected CO_2 in gas phase on the mobility ratio.

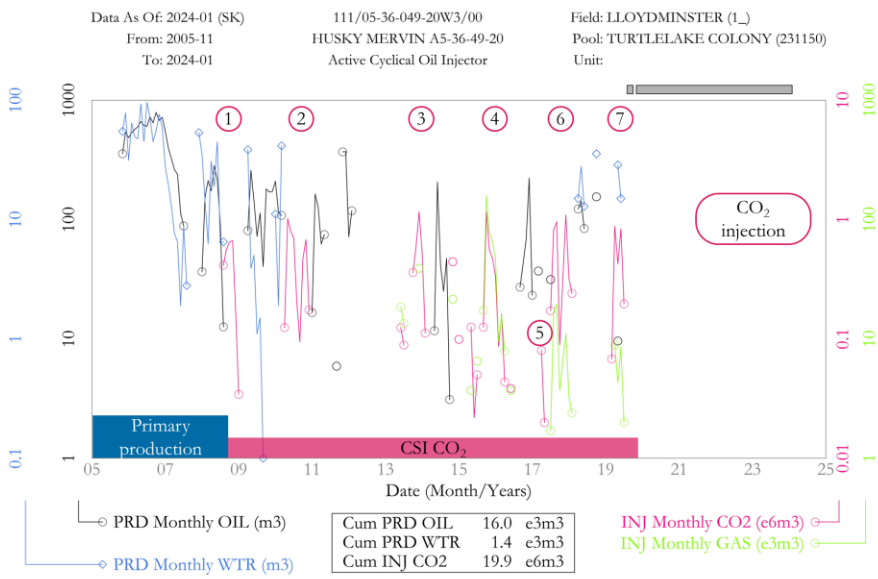

Fig 2-12. Mervin 05-36 production record.

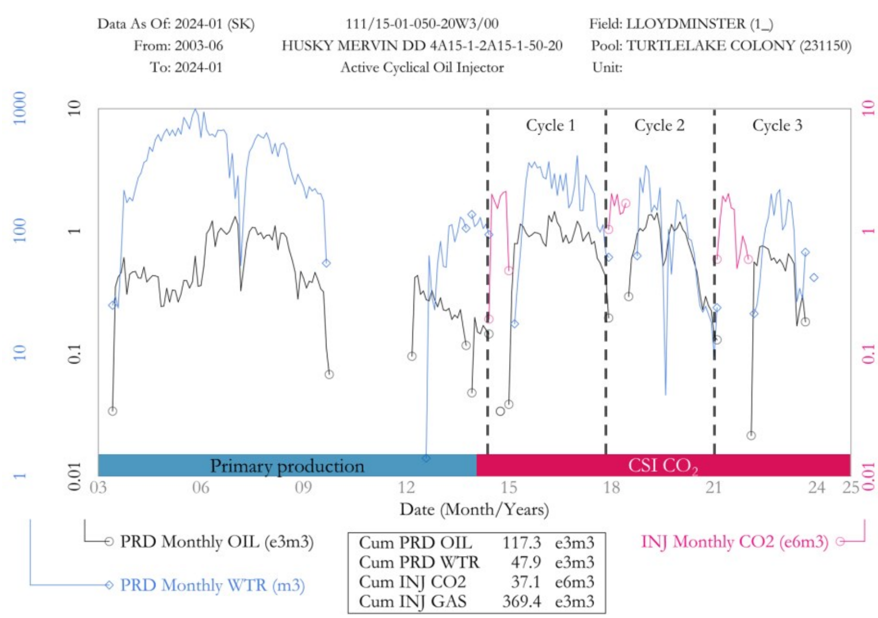

Fig 2-13. Production record of Mervin 15-01.

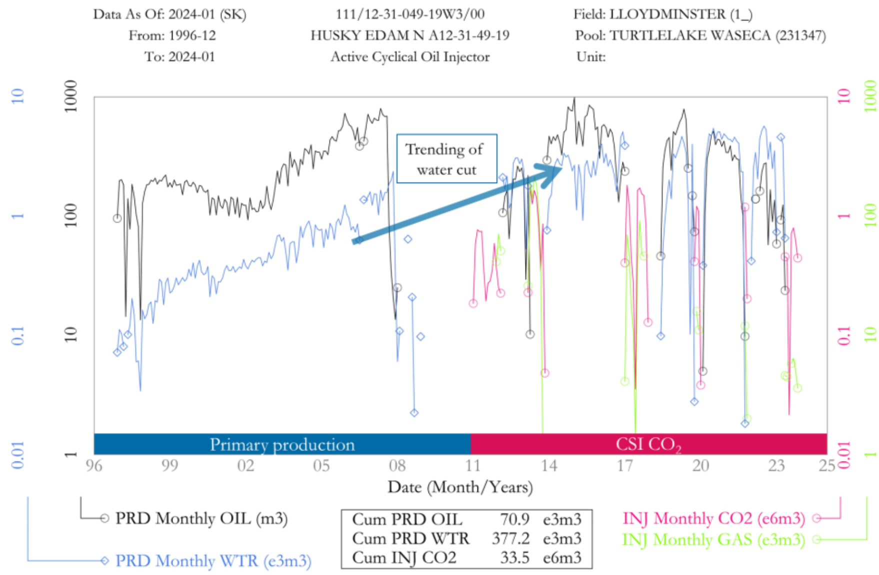

Fig 2-14. Production record for Mervin 12-31.

Case Study of the Husky Lashburn. This project was also involved the cyclic injection of CO_2 (Fig 2-15). In this reservoir, the behavior of each cycle seems to decline with high initial oil rate and low water cut. The water cut during CSI cycles was high which again suggests CO_2 injection in gas phase may not help to improve the mobility ratio. Field operational data indicated that 40% of the injected CO_2 remained in the reservoir [5]; the increasing trend of stored CO_2 eventually help to transition from CO_2 EOR to permanent CO_2 storage.

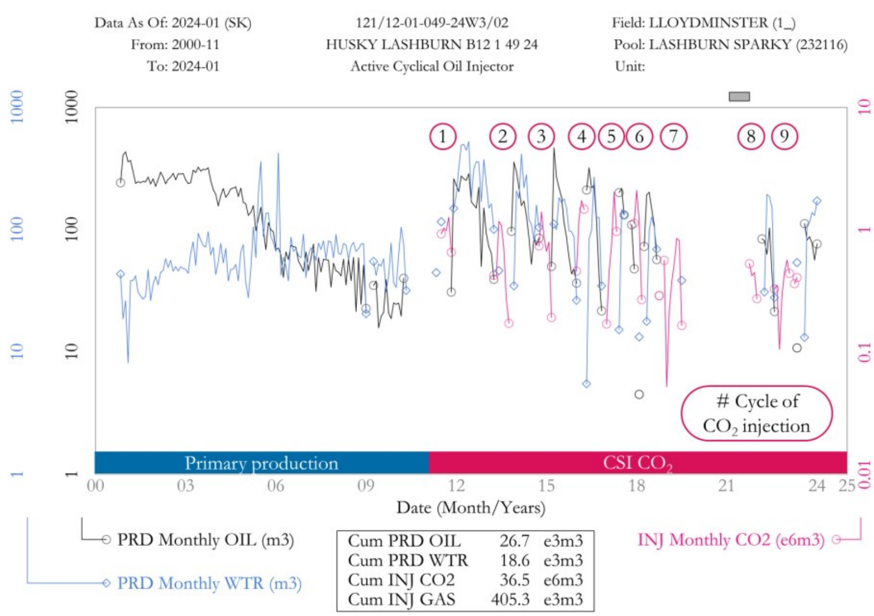

Fig 2-15. Production record for Sparky 12-01.

Case Study of the Dee Valley. This project has at least 6 wellbores (05-10-049-22W3, 06-10-049-22W3, 10-09-049-22W3, 14-09-049-22W3, 15-09-049-22W3, 16-09-049-22W3) where CO_2-CSI has been applied taking advantage of the proximity of the wellbores (Fig 2-16). All the wells were subject to cyclic injection of CO_2 at the beginning of 2015 with approximately 3 or 4 cycles until the end of 2018 or beginning of 2019.

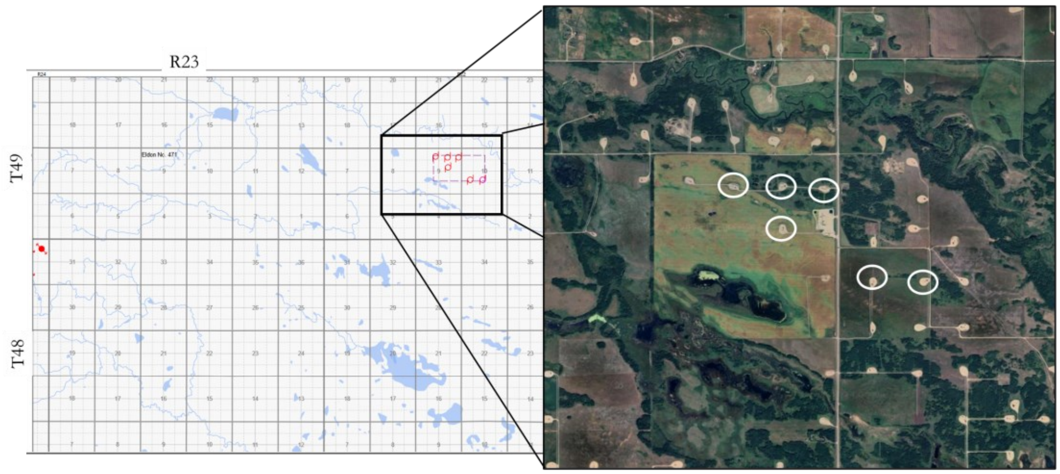

Fig 2-16. Layout and location of the CSI wellbores.

The wells display a characteristic pattern observed in CHOPs reservoirs during primary production, marked by a decline in oil rate and an increase in water cut, necessitating the implementation of a CSI program. CO_2 injection in one of these wells commenced in 2015, resulting in an equal water cut compared to the end of primary production but also an increased oil rate (**Fig *2-17***). Over the next 3 years, three cycles of CO_2 injection were carried out until 2024, leading to peaks in oil production equivalent to some of the highest levels during primary production and progressively increasing the water cut with subsequent cycles, which challenge again the possibility of a favorable mobility ratio for the oil with the injection of CO_2.

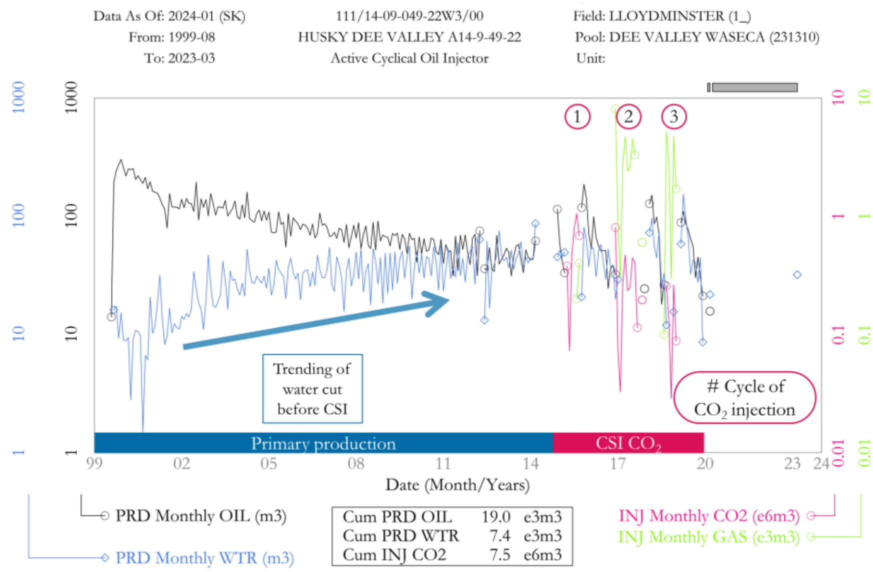

Fig 2-17. Record production for wellbore 121/12-01-049-24W3 at Dee Valley.

2.5. Conclusions and Remarks

Looking at the recent development of CSI process in thin unconsolidated heavy oil reservoirs, it appears that the popularity of cyclic solvent injection (as opposed to VAPEX and continuous solvent injection) has increased as a follow up EOR technique after cold production. Other IOR/EOR methods including waterflooding, gas flooding, and thermals (e.g. SAGD, CSS) can face efficiency issues with fingering, sweep efficiency, and significant heat loss; that again makes CSI a feasible EOR alternative to consider for thin heavy oil reservoirs. Regarding the solvent type and concentration, laboratory experiments are not conclusive to achieve high recovery factors; however, most of solvents either act to reduce heavy oil viscosity or to increase the strength of the foamy oil behavior (non-equilibrium nucleation and stability of the dispersed bubbles). Of interest, injection of CO_2 in gas phase has been employed at field scale in different reservoirs with some success to improve recovery factor. Numerical simulations still need to overcome modeling challenges to properly address the complex interplay of solvent-heavy oil reactions, foamy oil flow, sand production, and stress-deformations during loading/unloading cycles of CSI. Progress has been made to integrate kinetic reactions to model non-equilibrium phase behaviour. The lessons learned from field implementation of CSI indicated that highly productive wells during primary cold production are probably good performer during follow-up CSI operations, which confirms the important role of creating high-permeability channels and wormhole network so solvents can access more of intact portions of reservoir. A common observation from numerical simulations, laboratory experiments, and field tests is that the first CSI cycles are more effective to improve oil recovery; the additional recovery after each cycle decreases, meaning that field development strategies should be focused on first cycles of CSI.

2.6. Acknowledgement

This work was partially supported by Mitacs through the Mitacs Accelerate program. We gratefully acknowledge the Heavy Oil Research Network program, managed by the Petroleum Technology Research Centre, Regina for providing partial funding of this research project. We gratefully acknowledge the NSERC/Energi Simulation Industrial Research Chair in Reservoir Geomechanics in Unconventional Resources for additional funding. The authors also acknowledge the generous access to the software GeoScout.

2.7. References

[1] BP, "Statistical Review of World Energy," 2020.

[2] Canada Energy Regulator, "Crude Oil Annual Export Summary – 2020," 2021. [Online]. Available: https://www.cer-rec.gc.ca/en/data-analysis/energy-commodities/crude-oil-petroleum-products/statistics/crude-oil-summary/crude-oil-annual-export-summary.html. [Accessed: 26-Jul-2021].

[3] G. Coskuner, K. Naderi, and T. Babadagli, "An enhanced oil recovery technology as a follow up to cold heavy oil production with sand," Journal of Petroleum Science and Engineering, vol. 133, pp. 475–482, 2015.

[4] D. W. Zhao, J. Wang, and I. D. Gates, "Thermal recovery strategies for thin heavy oil reservoirs," Fuel, vol. 117, pp. 431–441, Jan. 2014.

[5] G. Coskuner and H. Huang, "Enhanced oil recovery in post-CHOPS cold heavy oil production with sand heavy oil reservoirs of Alberta and Saskatchewan part 2: Field piloting of cycling solvent injection," Society of Petroleum Engineers - SPE Canada Heavy Oil Conference 2020, CHOC 2020, vol. 3, 2020.

[6] M. B. Dusseault, "CHOPS: Cold Heavy Oil Production with Sand in the Canadian heavy oil industry," Waterloo, 2002.

[7] C. M. Istchenko and I. D. Gates, "Well/wormhole model of cold heavy-oil production with sand," SPE Journal, vol. 19, no. 2, pp. 260–269, 2014.

[8] E. Fjær, R. M. Holt, P. Horsrud, A. M. Raaen, and R. Risnes, Petroleum Related Rock Mechanics. Elsevier, 2008.

[9] V. Fattahpour, M. Roostaei, M. Mahmoudi, M. Soroush, S. A. Hosseini, and M. Anderson, "Standalone sand control evaluation: Developing a large-scale high temperature sand retention test apparatus," in SPE Canada Heavy Oil Conference 2020, 2020.

[10] K. Naderi, N. Romaniuk, and B. Ozum, "Improvement of the CHOPS process efficiency," in SPE Kuwait Oil and Gas Show and Conference, 2015.

[11] M. Plata, J. Bryan, and A. Kantzas, "Experimental study of heavy oil recovery mechanisms during cyclic solvent injection processes," in Proceedings - SPE Annual Technical Conference and Exhibition, 2018, no. June, pp. 24–26.

[12] X. Li, X. Sun, Z. Yang, H. Gong, T. Li, and X. Shi, "Experimental study on chemical-assisted methane flooding for foamy oil reservoirs after primary production," Journal of Petroleum Science and Engineering, vol. 216, p. 110803, Sep. 2022.

[13] P. Luo, S. Li, K. D. Knorr, and P. Nakutnyy, "A New PVT Apparatus for Automatic Measurement of Foamy Oil Generation and Stability," in PE Canada Heavy Oil Technical Conference, CHOC 2018, 2018, vol. 2018-Janua.

[14] B. Maini, "Foamy Oil Flow in Primary Production of Heavy Oil under Solution Gas Drive," in Annual Technical Conference and Exhibition, 1999.

[15] C. Shen, M. L. Hamm, and M. Bdair, "Improving cold heavy oil development at peace river with the understanding of foamy-oil dynamics," in SPE Kuwait Oil and Gas Show and Conference, 2015.

[16] M. Wu, X. Lu, J. Yang, Z. Lin, and F. Zeng, "Experimental analysis of optimal viscosity for optimizing foamy oil behavior in the porous media," Fuel, vol. 262, p. 116602, Feb. 2020.

[17] H. Wang, F. Torabi, F. Zeng, and H. Xiao, "A novel visualization approach for foamy oil non-equilibrium phase behavior study of solvent / live heavy oil systems," vol. 272, no. March, 2020.

[18] Z. Du, F. Zeng, and C. Chan, "Effects of pressure decline rate on the post-CHOPS cyclic solvent injection process," in Society of Petroleum Engineers - SPE Heavy Oil Conference Canada 2014, 2014, vol. 3, pp. 1979–1996.

[19] T. Lu, Z. Li, W. Fan, and S. Li, "CO2 huff and puff for heavy oil recovery after primary production," Greenhouse gases science and tecnology, vol. 6, pp. 288–301, 2016.

[20] S. Yang and D. Yang, "Integrated characterization of wormhole network by use of a modified pressure-gradient-based (PGB) sand failure criterion and ensemble-based history matching during CHOPS processes," Journal of Petroleum Science and Engineering, no. October 2021, p. 109777, Nov. 2021.

[21] L. Jiang, J. Liu, T. Liu, and D. Yang, "Characterization of Dynamic Wormhole Growth and Propagation During CHOPS Processes by Integrating Rate Transient Analysis and Pressure-Gradient-Based Sand Failure Criterion," in SPE Canadian Energy Technology Conference, 2022.

[22] X. Lei and Z. Gang, "A novel approach for determining wormhole coverage in CHOPS wells," in PE Heavy Oil Conference Canada 2012, 2012, vol. 2, pp. 1531–1549.

[23] L. Xiao and G. Zhao, "Integrated study of foamy oil flow and wormhole structure in CHOPS through transient pressure analysis," in SPE Heavy Oil Conference Canada, 2013, vol. 3, pp. 1946–1960.

[24] H. Yu and J. Y. Leung, "A Sand-Arch Stability Constrained Dynamic Fractal Wormhole Growth Model for Simulating Cold Heavy-Oil Production with Sand," SPE Journal, vol. 25, no. 06, pp. 3440–3456, Dec. 2020.

[25] K. Oldakowski and R. P. Sawatzky, "Direction of wormholes growth under anisotropic stress," in SPE Canada Heavy Oil Technical Conference, 2018.

[26] M. Pereira, "A Physical Model to Assess Sand Production Processes during Cold Heavy Oil Production with Sand," University of Saskatchewan, 2021.

[27] B. Meza-Díaz, R. Sawatzky, and E. Kuru, "Sand on Demand: A Laboratory Investigation on Improving Productivity in Horizontal Wells Under Heavy-Oil Primary Production—Part II," SPE Journal, vol. 17, no. 04, pp. 1012–1028, Dec. 2012.

[28] B. Mathur, A. Y. Dandekar, S. Khataniar, and S. L. Patil, "Life after CHOPS: Alaskan heavy oil perspective," in SPE Western Regional Meeting Proceedings, 2017, vol. 2017-April, pp. 914–927.

[29] J. Chang, J. Ivory, and M. London, "History matches and interpretation of CHOPS performance for CSI field pilot," in Society of Petroleum Engineers - SPE Canada Heavy Oil Technical Conference 2015, CHOC 2015, 2015, pp. 526–544.

[30] K. Oldakowski and R. P. Sawatzky, "Wormhole stability under post chops conditions," Society of Petroleum Engineers - SPE Canada Heavy Oil Technical Conference, CHOC 2018, vol. 2018-Janua, 2018.

[31] A. Mohamad-Hussein et al., "Geomechanical modelling of cold heavy oil production with sand," Petroleum, Mar. 2021.

[32] A. Rangriz Shokri and T. Babadagli, "A sensitivity analysis of cyclic solvent stimulation for post-CHOPS EOR: Application on an actual field case," SPE Economics and Management, vol. 8, no. 4, pp. 78–89, 2016.

[33] B. Yadali Jamaloei, R. Kharrat, and F. Torabi, "Analysis and correlations of viscous fingering in low-tension polymer flooding in heavy oil reservoirs," Energy and Fuels, vol. 24, no. 12, pp. 6384–6392, 2010.

[34] Z. Lin, "Experimental Study About Radial Viscous Fingering in Heavy Oil Reservoir," University of Regina, 2020.

[35] J. G. Maas, N. Springer, A. Hebing, J. Snippe, and S. Berg, "Viscous fingering in CCS - A general criterion for viscous fingering in porous media," International Journal of Greenhouse Gas Control, vol. 132, p. 104074, Feb. 2024.

[36] Y. Soh, A. Rangriz-Shokri, and T. Babadagli, "Optimization of methane use in cyclic solvent injection for heavy-oil recovery after primary production through experimental and numerical studies," Fuel, vol. 214, no. November 2017, pp. 457–470, 2018.

[37] Y. Li et al., "A review of in situ upgrading technology for heavy crude oil," Petroleum, vol. 7, no. 2, pp. 117–122, 2021.

[38] P. H. Krumrine, M. Lefenfeld, and G. A. Romney, "Investigation of post CHOPS enhanced oil recovery of alkali metal silicide technology," in SPE Heavy Oil Conference Canada 2014, 2014, vol. 3, pp. 1634–1650.

[39] Z. Du, F. Zeng, and C. Chan, "An experimental study of the post-CHOPS cyclic solvent injection process," Journal of Energy Resources Technology, Transactions of the ASME, vol. 137, no. 4, pp. 1–15, 2015.

[40] M. Huerta, J. M. Alvarez, E. Jossy, and K. Forshner, "Use of acid gas (CO2/H2S) for the Cyclic Solvent Injection (CSI) process for heavy oil reservoirs," Society of Petroleum Engineers - SPE Heavy Oil Conference Canada 2012, vol. 2, pp. 912–921, 2012.

[41] D. F. Cartagena-Pérez et al., "Scaled Physical Modeling of Cyclic CO 2 Injection in Unconsolidated Heavy Oil Reservoirs Using Geotechnical Centrifuge and Additive Manufacturing Technologies," in 2024 SPE Canadian Energy Technology Conference and Exhibition, 2024.

[42] J. Chang and J. Ivory, "Field-scale simulation of cyclic solvent injection (CSI)," Journal of Canadian Petroleum Technology, vol. 52, no. 4, pp. 251–265, 2013.

[43] J. A. Rivero et al., "Modeling CHOPS Using a Coupled Flow-Geomechanics Simulator With Nonequilibrium Foamy-Oil Reactions: A Multiwell History Matching Study," in SPE Annual Technical Conference and Exhibition, 2010.

[44] A. Rangriz Shokri and T. Babadagli, "An approach to model CHOPS (cold heavy oil production with sand) and post-CHOPS applications," in Proceedings - SPE Annual Technical Conference and Exhibition, 2012, vol. 3, no. 1, pp. 2305–2316.

[45] A. S. Haddad and I. Gates, "Modelling of Cold Heavy Oil Production with Sand (CHOPS) using a fluidized sand algorithm," Fuel, vol. 158, pp. 937–947, Oct. 2015.

[46] B. Vanderheyden, B. Jayaraman, X. Ma, and D. Zhang, "Multiscale Simulation of CHOPS Wormhole Networks," in SPE Reservoir Simulation Symposium, 2013.

[47] H. Ma, G. Yu, Y. She, and Y. Gu, "A new hybrid production optimization algorithm for the combined CO2-cyclic solvent injection (CO2-CSI) and water/gas flooding in the post-CHOPS reservoirs," Journal of Petroleum Science and Engineering, vol. 170, no. January, pp. 267–279, 2018.

[48] M. Zhang, Z. Du, F. Zeng, and S. Xu, "Upscaling study of cyclic solvent injection process for post-chops reservoirs through numerical simulation," in Society of Petroleum Engineers - SPE Heavy Oil Conference Canada 2014, 2014, vol. 3, pp. 1651–1669.

[49] J. J. Martinez Gamboa and J. Y. Leung, "Design of field-scale cyclic solvent injection processes for post-CHOPS applications," Canadian Journal of Chemical Engineering, vol. 97, no. 1, pp. 123–132, 2019.

[50] J. Chang, J. Ivory, and G. Beaulieu, "Pressure maintenance at post-CHOPS cyclic solvent injection (CSI) well using gas injection at offset well," in SPE Heavy Oil Conference, 2014, vol. 2, pp. 1387–1409.

[51] X. Tang, C. Yu, Y. Bai, H. Lu, and M. S. Mohamed, "Field Trial of Nitrogen-Assisted Cyclic Steam Stimulation in Post-CHOPS Wells, Case Study in Sudan," in SPE Thermal Well Integrity and Production Symposium, 2022.

Chapter 3

A Summary of Geotechnical Centrifuge Applications in Petroleum Engineering

3.1. **Abstract**

This paper presents a review of the applications of geotechnical centrifuge technology in petroleum engineering, exploring its principles, scaling laws, and various experiments conducted to address complex challenges in the petroleum industry. The geotechnical centrifuge has been used for physical modeling of sand production, caprock integrity, thermal oil recovery, and wellbore stability. The paper discusses centrifuge scaling laws that govern the relationship between prototype and model parameters, emphasizing their significance in achieving accurate representation of a physical sample, for instance a reservoir prototype. Additionally, it provides a review of several centrifuge experiments conducted to investigate dynamic reservoir behavior, seismicity, thermal fluid recovery, and rock failure mechanisms. The paper also explores how a broader applications of geotechnical centrifuge technology in civil engineering can be extrapolated to address flow and deformation issues encountered in reservoir engineering problems. These include dynamic reservoir properties, changes in fluid saturation, and flow patterns around wellbore. The review demonstrates the potential of the geotechnical centrifuge in understanding multiphase flow processes in deformable porous media.

Keywords

Geotechnical Centrifuge, Reservoir Engineering, Sand Production, Caprock Integrity, Scaling Laws, Thermal Recovery, Wellbore Stability, Multiphase Flow, Physical Modeling

3.2. Introduction

Modelling geomechanical reservoir response due to changes in pore pressure and temperature during fluid production/injection is still a challenge faced by reservoir engineers. A part of the modelling can be done through numerical tools while experimental approaches and field data can be useful to capture the physics of complex thermo-hydromechanical phenomena. In this work, we review the use of the geotechnical centrifuge, as a particular experimental tool, to physically model the fluid flow in porous media, reservoir deformations, and rock failure modes. The first part of the review is devoted to show the physics behind the geotechnical centrifuge, its fundamental principles, followed by its application to reservoir engineering problems. Among others, specific emphasis is on sand production, and caprock integrity that have been physically tested in literature with the use of the geotechnical centrifuge. The paper inquiries about the potential applications of the geotechnical centrifuge to different areas of reservoir engineering, pointing out the recent studies that have been conducted by civil engineers. This section discusses how new technologies from other engineering disciplines can be implemented to improve our understanding of the porous media.

3.3. Principles of Geotechnical Centrifuge Technology

The centrifuge modelling places a scale prototype of the soil into a geotechnical centrifuge to upscale its behavior [1]. The physical principle of the centrifuge modelling is the similarity of the stress state between the prototy and the model. This principle was articulated with engineering problems by 1896 by Phillips in front of the French Academy of Sciences [2], and lately in the 50's obtained a wider welcome into problem where stresses and selfweight were key elements [3].

In geotechnical engineering is broadly accepted that the behavior of the rock under shear conditions depends on the level of effective confinemet at which the sample is subjected [4]-[6]. A sample will experience a dilation behavior if the shearing happens at a relatively low confining stress (low *p'*) such as that in small model tests at 1G, compared to a second sample is with the same density, thereford the same void ratio (*e*), but subjected to the shearing stress under high comfining stress (Fig 3-1). In this case, the sample will contract. This divergency between the two behavior is covered by the capability of the centrifuge to emulate the distribution of stresses in the prototype but in a model that is more hadlable at a laboratory scale [7].

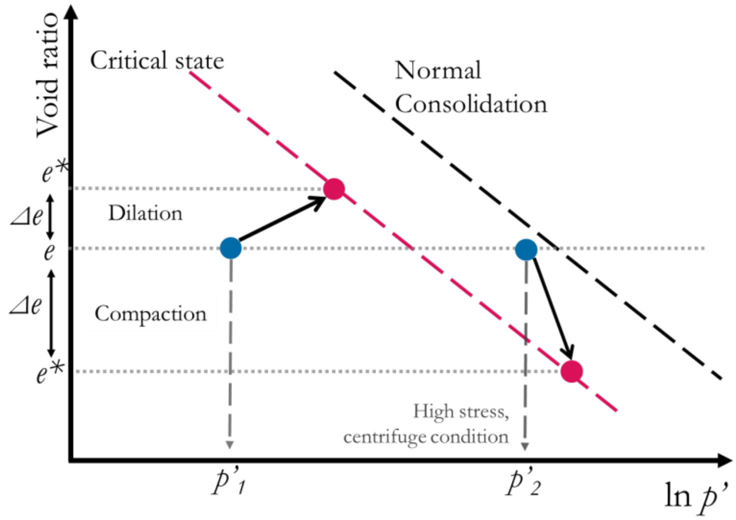

Fig 3-1. Response to shear stress at different mean stress. Modified from [7]

The centrifuge created the enhanced gravity environment under the concept of the uniform circular motion, when a body travels around a circle or circular path at a constant speed. In other words: "the basic premise of centrifuge modelling is that we test a 1/N scale model of a prototype in the enhanced gravity field of a geotechnical centrifuge" [1]. Fig 3-2 illustrates the uniform circular motion of a body at constant angular speed $\dot{\theta}$ (Change of the angle [θ] with time):

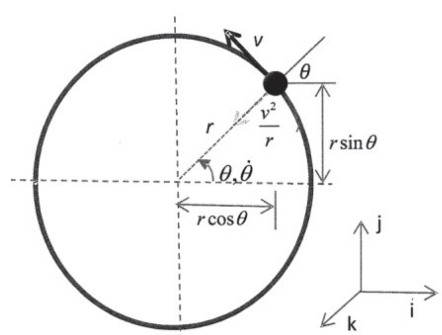

Fig 3-2. Diagram of uniform circular motion. Taken from [1]

In this geometry, taking the distance from the center to the prototype mass as constant (r), the acceleration can be calculated as [8]:

$$a = r\dot{\theta}^2 \qquad (3\text{-}1)$$

where a is the acceleration, r is the radius from the center to the mass, and $\dot{\theta}$ is the angular speed. This expression is valuable to understand the enhanced gravity field which is direct function of the radius. At the same angular speed, a centrifuge with a larger arm can induce a high acceleration. With the same logic, a centrifuge with a given arm's length can accelerate the sample directly with the square of the angular speed. This concept of acceleration in Eq. (3-1) can produces an ehanced gravity environment that can be expressed as:

$$r\dot{\theta}^2 = Ng \tag{3-2}$$

where N is the number of times the gravity is enhanced, and g is the accelaration gravity as 9.81 m/s². Fig 3-3 illustrates how the same soil structure can be represented by different modeling geometries depending upon the enhanced gravity field (N).

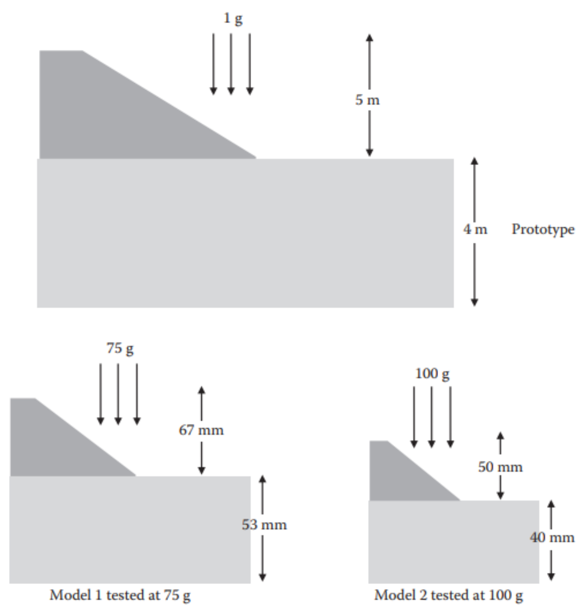

Fig 3-3. Prototype and models at different enhanced gravity fields. Taken from [1]

As the soil structure and geometry of the models is subjected to scale, in the same way some physical measurements need to be adjusted. Those adjustments are called scaling laws. The scaling laws are relationship between the magnitude of the prototype and the model [1]. The scaling laws are based on the enhanced gravity field written as Ng as shown in the Fig 3-4.

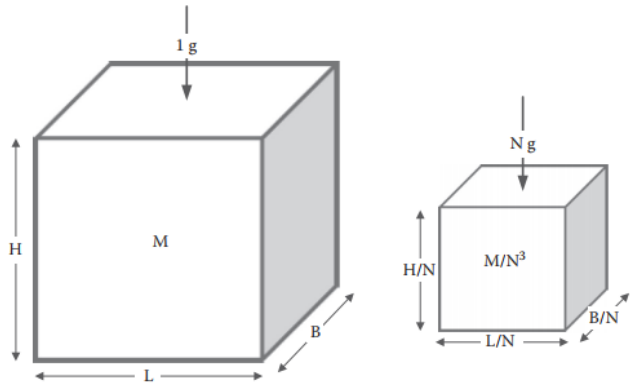

Fig 3-4. Scale law applied to a volume. Taken from [1]

Table 3-1 summaries the scaling laws for several physical parameters.

Table 3-1. Scaling laws based on [9]

Parameter	Scale factor	Units
Linear dimension, l	1 : N	m
Displacements, z	1 : N	m
Porosity, φ	1 : 1	-
Intrinsic permeability, k	1 : N	m^2
Hydraulic conductivity, K	1 : 1	ms^{-1}
Hydraulic gradient, i	$1 : N^{-1}$	Pam^{-1}
Stress, σ	1 : 1	Nm^{-2}
Strain, ε	1 : 1	-
Density, ρ	1 : 1	kg m^{-3}
Temperature, T	1 : 1	°C
Pressure, P	1 : 1	Nm^{-2}
Area, A	$1 : N^2$	m^2
Volume, V	$1 : N^3$	m^3
Gravity, g	$1 : N^{-1}$	ms^{-2}
Viscosity, μ	1 : 1	cp
Time (consolidation), T	$1 : N^2$	s
Time (dynamic), t	1 : N	s

Some authors, such as [10], have discussed the use of the scaling laws and their extension to dynamic processes like fluid flow through porous media, validating the mathematical relationship between models and prototypes.

3.4. Applications of Geotechnical Centrifuge in Petroleum Engineering

This section introduces research conducted by various authors using a geotechnical centrifuge to investigate complex phenomena in oil reservoirs. Their results and analyses help to enhance our understanding of flow-deformation mechanisms and dynamic reservoir behavior; they also identified knowledge gaps and areas where additional research is required.

3.4.1. Experimental Modeling of Sand Production

Vaziri & Lemoine [2] conducted pioneering tests aimed at comprehending sand production utilizing a geotechnical centrifuge. Their study involved the design and fabrication of a cell featuring a central wellbore surrounded by sand. The produced sand during centrifuge spin was directed to a load cell, which quantified the mass of the sand. The experimental setup is visually depicted in Fig 3-5 [12].

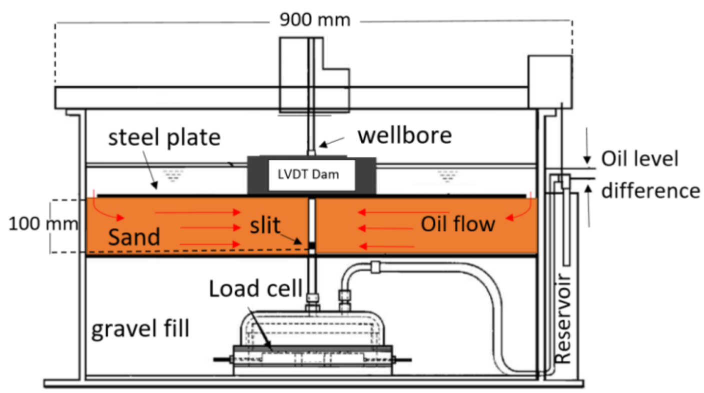

Fig 3-5. Setup used to study the sand production. Taken from [13] who modified it after [12].

The experiment was performed under a hyper-gravitational force of 24 G, and upon physical examination, the emergence of a conical cavity around the wellbore was observed as a consequence of production of the loose sand. This distinctive cavity is emphasized in [13]. Additionally, a region exhibiting plastic strain was identified and correlated with the observed subsidence. Notably, a comparable behavior was theoretically posited by Dusseault [14] in the context of extensive sand production in CHOPS reservoirs (Cold Heavy Oil Production with Sand). In this technique, the heavy oil is produced at rates that yield the reservoir resulting in a massive production of sand. With the production of sand, some cavities, so called "wormholes", are produced from the wellbore and extending to the reservoir [15]. Those wormholes are understood as high permeable channels that allow a better production.

This experiment focuses on understanding the failure mechanism of loose sand surrounding a wellbore. [12] emphasize that the intention of this experiment was not to replicate every aspect of reservoir conditions. Instead, it successfully captured the fundamental components of failure, such as the extension of wormholes or cavities in a granular material (Fig 3-6).

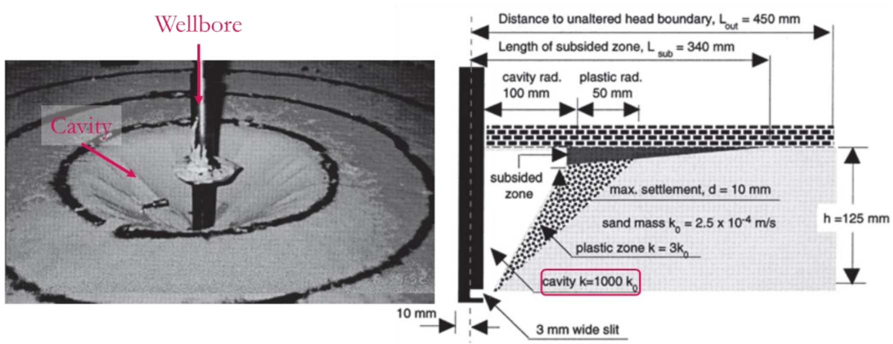

Fig 3-6. Cavity in the sample (left) and scheme of the cavity after spinning (right). Modified from [12]

In more recent experiments, Pereira [13] and Layeghpour [16] employed a beam geotechnical centrifuge to investigate sand production in CHOPS reservoirs, drawing inspiration from Canadian heavy oil reservoirs. Their experimental setup featured a tub with a central wellbore; a depiction of this configuration is provided in Fig 3-7.

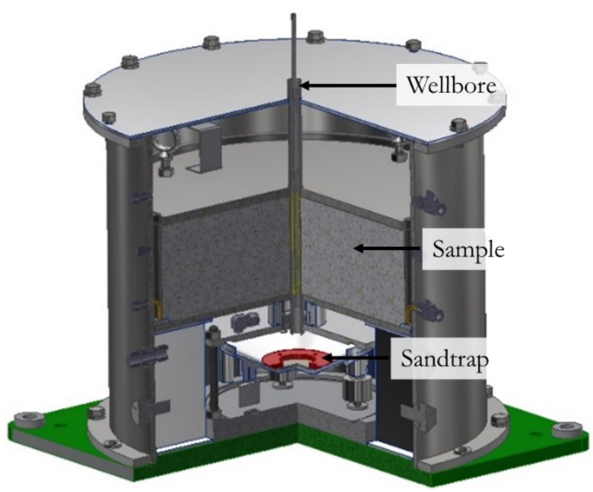

Fig 3-7. View of the cell used by [13] and, [16]

Following an extensive series of tests, [13] and, [16] consistently observed the formation of a distinct cavity around the wellbore after sand production in all cases. Remarkably, these cavities exhibited an inverse conical shape, aligning with the experimental findings by [11], [12], [17]. These experimental observations from geotechnical centrifuge tests have challenged the previously assumed concept of wormholes or erosional channels as the primary mechanisms for yielding during massive sand production, as experienced in CHOPS reservoirs.

The experimental methodologies employed by [12], [13] and, [16], utilizing physical representations of loose sand reservoirs during massive sand production, exemplify the potent capabilities of geotechnical centrifuge modeling. This approach enables engineers to examine the dynamics of fluid drainage area at the field scale inside research laboratories, providing insights into the fundamentals of yielding and failure mechanisms.

3.4.2. Experimental Modeling of Caprock Integrity

The caprock is the geological formation over the reservoir and usually has a lower permeability serving as the top "sealing" of the reservoir. The mechanical and hydraulic integrity of the caprock holds significant importance across various oil production techniques, ranging from primary recovery methods to Enhanced Oil Recovery (EOR) practices including thermal and solvent injections [18]. More recently, caprock integrity has become a crucial topic to assure that sealing capability of underground formations involved in carbon sequestration efforts [19]. Addressing caprock integrity is paramount for geoenergy industry and regulatory bodies, as it ensures that operations are conducted under safe conditions, implying that fluids are effectively trapped within the intended porous media.

The implications of thermal EOR through Steam Assisted Gravity Drainage (SAGD) operations on caprock integrity, utilizing a geotechnical centrifuge model was study in [20]. To model the deflection mechanism induced by the steam chamber over the caprock layer (representing the Clearwater shale), a mechanical device known as GeoCDM was included in the centrifuge experimental cell. This device was activated when the model was subjected to hyper-gravity conditions.

Under hyper-gravity conditions, the rise of steam chamber (modeled using the GeoCDM) induced shearing effects at different time scales; the process simulated the shearing caused by the steam chamber throughout the life of the heavy oil reservoir. Fig 3-8 illustrates the resulting shearing cracks and bands in the shale model, showcasing the effects after 15 years of constant bending. This observation is noteworthy because conducting a typical laboratory test for a period of 10 years would be nearly impractical for many engineering research. However, the capability of the geotechnical centrifuge to scale up the model size and reduce time makes such experiments feasible.

Fig 3-8. a) Physical representation of the shearing in the caprock obtained with the centrifuge modelling, and b) Maximum total shear strain

3.4.3. **Off-shore engineering**

Offshore oil production and reservoir engineering heavily rely on the stability and reliability of platforms. An established practice in achieving this stability involves the utilization of anchors to secure offshore platforms to the seabed [21]. In a physical modeling study on anchors, [21] conducted tests to assess their resistance by embedding them into normally consolidated clay, representing the seabed (see Fig 9-a). The findings indicate that heavier anchors exhibit increased resistance against pulling forces. Moreover, these results contribute to establishing essential benchmarks for design considerations through the application of physical modeling.

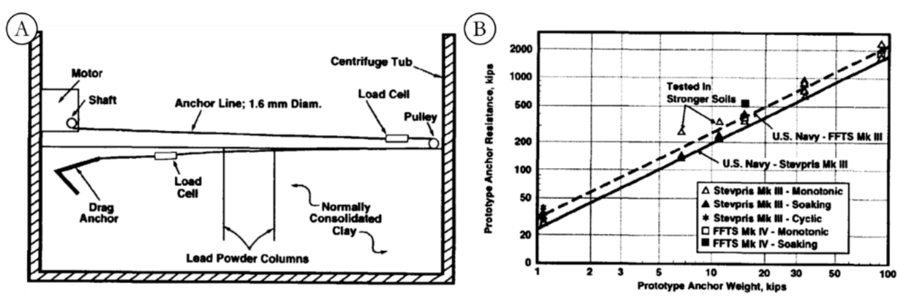

Fig 3-9. a) Diagram of the testing setup for the anchor. b) Anchor resistance. Taken from [21]

3.5. **Opportunities**

In this section, the primary objective is to illustrate various applications of the centrifuge across diverse problems, predominantly within civil engineering, while emphasizing their potential relevance to reservoir engineering issues. Consequently, solutions and insights derived from civil engineering applications may find analogous applications in reservoir engineering experiments. The application of centrifuge technology has been broadened to encompass a range of areas, particularly in comprehending the behavior of porous media.

3.5.1. **Study of the Reservoir Properties and Their Changes**

One of the primary applications of the geotechnical centrifuge lies in comprehending the interaction among granular material, porous space, and fluid flow within it. [22] devised a cell to investigate one-directional flow through partially saturated samples. The experimental design featured a soil column with a height of 300 mm, spun at 50 and 100 Gs. This setup effectively represented prototype samples of 15 and 30 meters in height, showcasing the geotechnical centrifuge's capability to model porous media columns with thicknesses akin to many reservoirs. This scalability is a notable advantage of the geotechnical centrifuge for studying and understanding oil reservoirs.

When coupled with the analysis of flow and distribution within porous media, as demonstrated by [22], it becomes possible to derive saturation profiles in a reservoir, exemplified in Fig 3-10-A. Another advantage lies in the ability to conduct experiments that would otherwise be impractical in a conventional laboratory setting. Fig 3-10-B illustrates the normalized flow rate over prototype time, which spans approximately 30,000 hours (nearly 3.5 years). Such prolonged tests would pose significant challenges under normal laboratory conditions but become feasible thanks to the hyper-gravity of the centrifuge and the scaling of time in prototypes. This presents an opportunity window for reservoir engineering to engage in physical modeling of long-term flow scenarios.

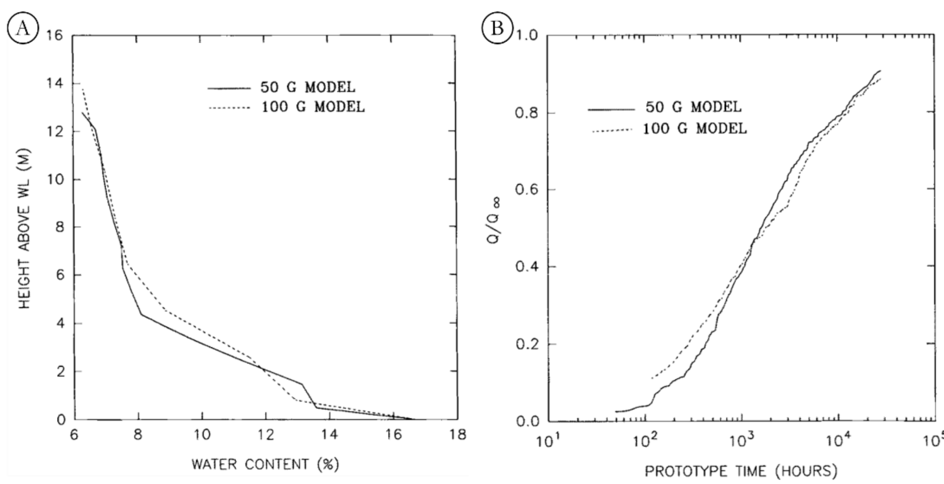

Fig 3-10. a) saturation profiles, and b) normalized flowrate. Taken from [22]

In the work by [23], a similar methodology is employed to examine unsaturated soils and their hydraulic conductivity. This problem shares similarities with multiphase flow dynamics within reservoirs, where relative permeabilities are associated with different fluids. The investigation of unsaturated soils has also been applied to comprehend the movement of contaminants in the upper layers of the soil [24]. A parallel approach could be envisioned for modeling the tracing of substances throughout a reservoir.

Motivated by the study of multiphase flow of contaminants in unsaturated porous media, a European network of experimental research was established [25]. At the University of Cambridge, the network conducted a test involving multiple inclined layers of sand in unsaturated soils. The experiment entailed injecting water into the top layer and recording the pressure and fluid distribution, depicted in Fig 3-11. The plume exhibited in Fig 3-11-B bears a resemblance to the typical shape of a steam chamber used in the study of Steam Assisted Gravity Drainage (SAGD) but inverted. This experiment and its outcomes draw a compelling parallel with the experimental approaches that reservoir engineers could adopt for physical modeling of multilayered reservoirs, enabling the exploration of flow patterns and saturation distribution in more realistic models.

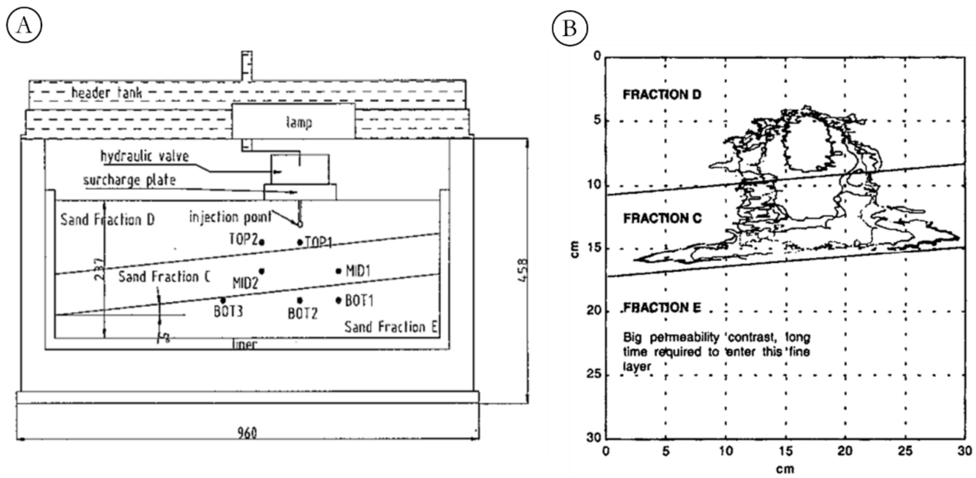

Fig 3-11. A) Experimental setup with multiple layers of sand. B) Plume developed through the different layers of sand. Taken from [25]

In the study conducted by [26], an attempt is made to model changes in multiple layers when a surcharge is applied over various types of soils. Their experiment focuses on detecting consolidation (increase in density) in a double-porosity clay setup. Spanning the model over a prototype time of nearly 40 years, they applied a surcharge at year 23 to observe changes in settlement. The results, presented in Fig 3-12, clearly indicate that the surcharge has a noticeable impact on the settlement of the entire system.

This approach holds promise for application in reservoir engineering, particularly in comprehending complex phenomena such as subduction that encompasses a substantial geomechanical component. The utilization of physical modeling over an extended prototype time spanning several years provides an avenue to capture and understand such intricate processes.

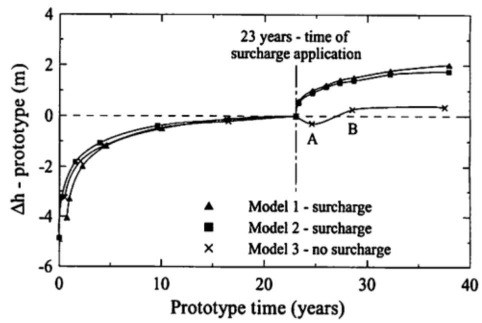

Fig 3-12. Settlement as change in the height of the prototype. Taken from [26]

3.5.2. **Study of Dynamic Reservoir Behavior and Seismicity**

The convergence of civil and reservoir engineering is evident in the investigation of the dynamic behavior of rock masses. [27] conducted an experiment where horizontal layers of soils are subjected to "squeezing" to emulate the deformation typical in fold-thrust regimes, as illustrated in Fig 3-13. The ability to replicate such regional phenomena holds potential for understanding the activation and reactivation of faults. This becomes particularly promising when incorporating fluid flow elements to simulate the physics involved in the reactivation of faults and seismic events within oil reservoirs.

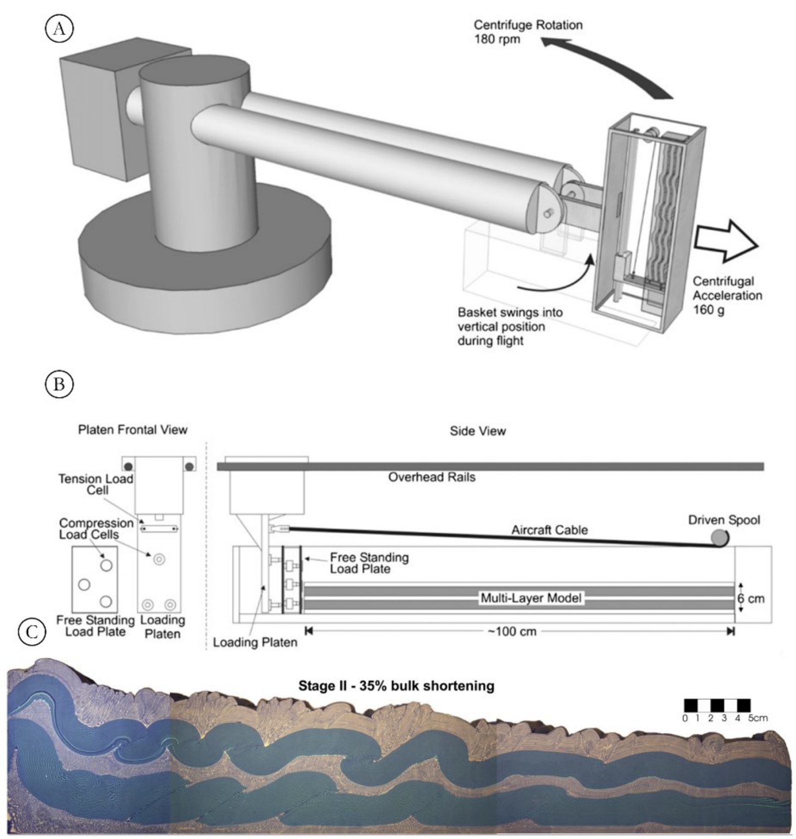

Fig 3-13. Setup and result of the study of fold-thrust regimes in a centrifuge. Taken from [27]

A similar methodology was employed by [28], where a jack ascends a wedge, displacing layers of sand positioned at its summit to simulate movement along a fault. The experimental setup is detailed in Fig 3-14. In Fig 3-14-C, the consequences of the fault displacement are observable as plastic strain in the pipe. This approach has potential use in reservoir engineering problems for studying intricate wellbore-reservoir systems, akin to those found in naturally fractured reservoirs with horizontal wellbores, e.g. shale resources.

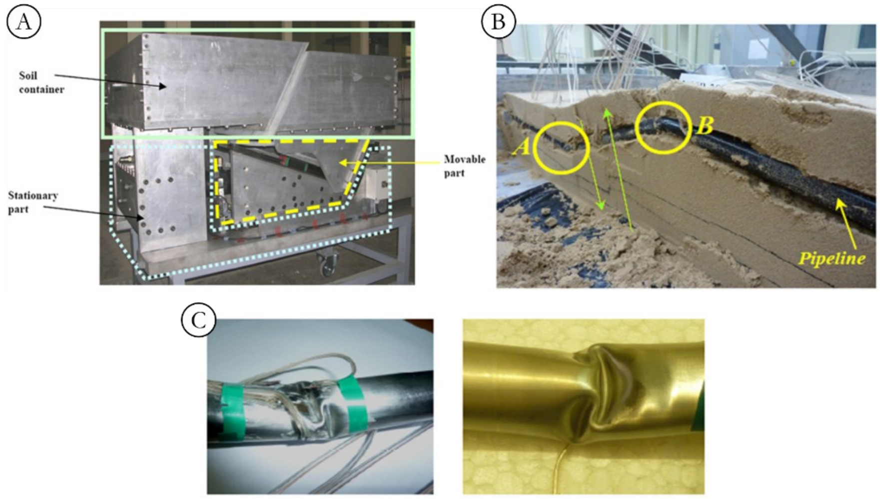

Fig 3-14. a) mechanical description of the faulting mechanism. b) image that shows the embedded pipeline and its deformation, and c) deformations of the pipeline at both ends of the shearing plane. Taken from [28]

3.5.3. **Thermal Recovery**

It is widely acknowledged that thermal Enhanced Oil Recovery (EOR) has a direct impact on geomechanics, influencing the stress state within the reservoir [29]. The alterations associated with thermal stresses can be tracked through the temperature distribution and subsequent strain. [30] conducted a test wherein a thermal probe is placed in the center of a circular sample measuring 118 mm. Multiple thermocouples are arranged radially to gauge the temperature front over time and distance, as depicted in Fig 3-15-(a).

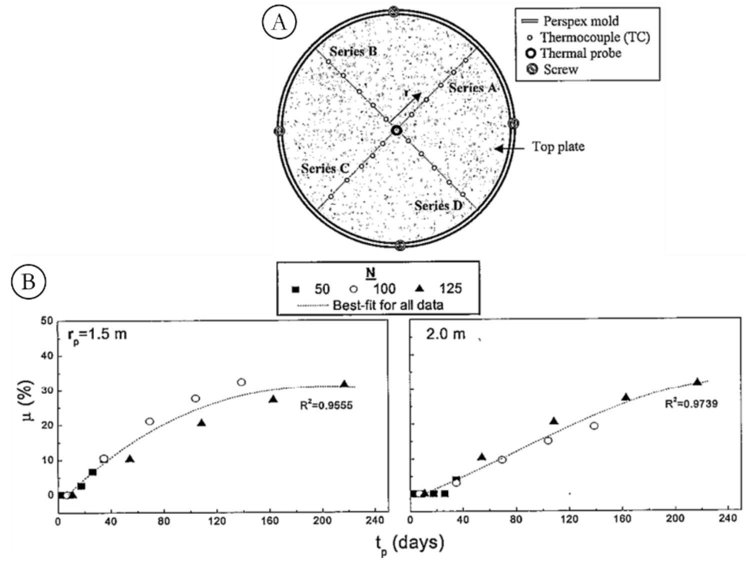

Fig 3-15. a) setup and disposition of the thermocouples into the sample, b) change in temperature (μ) with time.

Similar models could be employed to simulate thermal EOR by heating the fluids around a wellbore to reduce their viscosity. The geotechnical centrifuge proves advantageous as it enables larger samples and prolonged periods of prototype physical modeling, as illustrated in Fig 3-15-(b) with a modeling duration of 7.7 months. More comprehensive models, incorporating induced anisotropies that demand attention, as described by [26], could be effectively physically modeled using the centrifuge. This opens up a broad spectrum of possibilities for exploring complex experimental phenomena, such as heat transfer in porous media.

3.5.4. **Wellbore integrity**

Wellbore stability is a complex phenomenon involving not only the mechanical stability of the wellbore but also the interactions with surrounding reservoirs and field stresses [31], [32]. One prevalent issue in this domain is erosion, which may occur if certain fluids migrate between the casing and cementation or between the cementation and the formation [33]. Fig 3-16 illustrates various paths that a stream of CO_2 might take to leak from a reservoir. Additionally, on the right side of the image, there is a diagram illustrating seepage under a dam that could lead to erosional effects at the exit point.

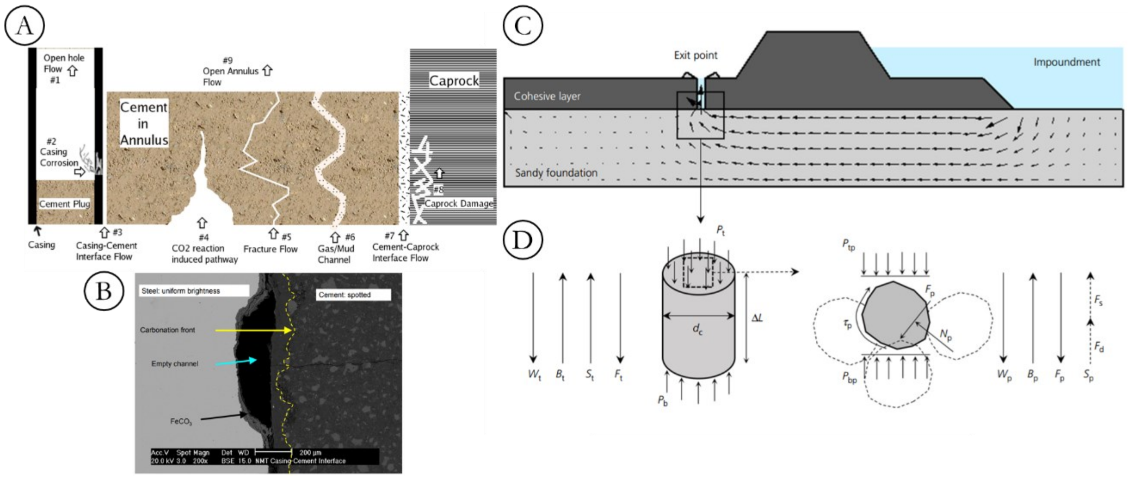

Fig 3-16. Erosional phenomena at different scales. a) different paths that would lead to CO2 leaking, b) image of a leak path between the cementation and the casing, c) General seepage in a dam and its exit point, d) Analysis of forces in the erosional process. Taken from [34] and [35].

In a study by [35], the impact of upward flow on the integrity of dams and the potential formation of erosional channels was investigated. The researchers conducted a centrifuge experiment employing a cylindrical sample, inducing linear flow from the bottom to the top under various hyper-gravity scenarios (10, 20, and 30 G). These experiments not only evaluated the impact of upward flow on erosional piping but also allowed for the observation of how erosional channels changed with this flow pattern, as depicted in Fig 3-17.

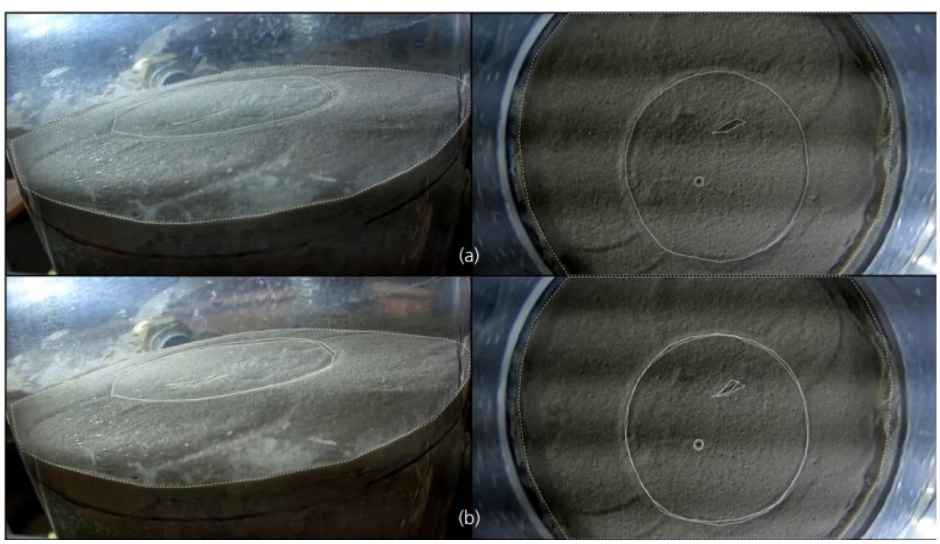

Fig 3-17. Areal and lateral view of the erosional channel. Taken from [35]

3.6. **Limitations of Geotechnical Centrifuge**

Despite its simple physics and extensive capabilities, the implementation of geotechnical centrifuge technology for reservoir engineering comes with several limitations, including:

1. **Cost**: Geotechnical centrifuge facilities are expensive to establish, operate, and maintain. Their implementation necessitates substantial civil construction to ensure safe operation, contributing to the limited availability of centrifuge facilities worldwide.
2. **Remote Operation**: As most centrifuge experiments occur at high speeds, devices such as valves need to be remotely operated during hyper-gravity. This limitation restricts access to the centrifuge while it is spinning, requiring careful experiment planning or, more realistically, a trial-and-error approach.
3. **Self-Weight Systems**: Devices relying on self-weight mechanisms, such as solenoid valves, may not function properly at hyper-gravity levels because the weight is scaled multiple times, affecting their functionality.

3.7. **Conclusions**

The utilization of geotechnical centrifuge technology in reservoir engineering has emerged as a powerful tool, providing unique insights into intricate phenomena such as sand production, caprock integrity, thermal recovery, and wellbore stability. The capability to replicate enhanced gravity conditions, combined with the application of scaling laws, facilitates the bridging of gaps between laboratory experiments and real-world reservoir challenges. The reviewed experiments not only yield valuable data on failure modes and mechanisms but also offer a deeper understanding of the dynamic behavior of reservoir systems over extended periods.

Despite certain limitations and associated costs, the geotechnical centrifuge stands as a crucial asset in the reservoir engineer's toolkit, promising continuous advancements and innovative solutions to address the evolving demands of the oil and gas industry. In conclusion, the comprehensive review of geotechnical centrifuge technology in reservoir engineering underscores its multifaceted contributions to the field. The discussed experiments, ranging from sand production studies to caprock integrity assessments, highlight the versatility and adaptability of the centrifuge in addressing diverse challenges. The incorporation of scaling laws provides a systematic approach to ensuring accurate physical modeling, enhancing the reliability of the obtained results.

As we look ahead, the potential applications of geotechnical centrifuge technology extend beyond current boundaries, promising exciting opportunities for further exploration and discovery in reservoir engineering. Researchers, engineers, and practitioners are encouraged to leverage this technology to unlock new insights, optimize operational strategies, and contribute to the sustainable development of reservoirs in the ever-evolving energy landscape.

3.8. **References**

[1] G. Madabhushi, Centrifuge modelling for civil engineers. 2017.

[2] R. Phillips, "Computes Reudus de l'Academie des Sciences." Paris, p. 68, 1869.

[3] P. H. Joseph, H. H. Einstein, and R. V. Whitman, "A literature review of geotechnical centrifuge modeling with particular emphasis on rock mechanics," 1988.

[4] M. Budhu, Soil mechanics and foundations, 3rd ed. John Wiley & Sons, 2010.

[5] J. M. Duncan, S. G. Wright, and T. L. Brandon, Soil strength and slope stability, 2nd ed. New Jersey: Wiley, 2014.

[6] B. Das and N. Sivakugan, Fundamentals of geotechnical engineering. Boston: Cengage Learning, 2017.

[7] C. W. W. Ng, "The state-of-the-art centrifuge modelling of geotechnical problems at HKUST," Journal of Zhejiang University SCIENCE A, vol. 15, no. 1, pp. 1–21, Jan. 2014.

[8] R. N. Taylor, Geotechnical Centrifuge Technology, 1st ed. London: Taylor & Francis, 1995.

[9] E. M. J. S. Lemoine, "Modelling Sand Production in a Geotechnical Centrifuge," Dalhousie University, 1999.

[10] R. Butterfield, "Scale-modelling of fluid flow in geotechnical centrifuges," Soils and Foundations, vol. 40, no. 6, pp. 39–45, 2000.

[11] H. H. Vaziri and L. Lemoine, "Strong support for significant productivity boost through sand production," in 4th North American Rock Mechanics Symposium, NARMS 2000, 2000, pp. 295–302.

[12] H. H. Vaziri, S. Thallak, and R. Phillips, "Centrifuge tests to identify mode of sand production and its effect on production," International Journal of Rock Mechanics and Mining Sciences, vol. 35, no. 4–5, p. 75, 1998.

[13] M. Pereira, "A Physical Model to Assess Sand Production Processes during Cold Heavy Oil Production with Sand," University of Saskatchewan, 2021.

[14] M. B. Dusseault, "CHOPS: Cold Heavy Oil Production with Sand in the Canadian heavy oil

industry," Waterloo, 2002.

[15] C. M. Istchenko and I. D. Gates, "Well/wormhole model of cold heavy-oil production with sand," SPE Journal, vol. 19, no. 2, pp. 260–269, 2014.

[16] S. Layeghpour, "Geotechnical centrifuge experiments to improve understanding of sand production from heavy oil reservoirs," University of Saskatchewan, 2021.

[17] P. Ian, V. Hans, W. Stephen, M. Zissis, C. John, and I. Ion, "Predicting and Managing Sand Production: A New Strategy," in Proceedings of SPE Annual Technical Conference and Exhibition, 2003, pp. 3949–3961.

[18] B. G. do. S. Costa, M. A. Jaculli, J. R. P. Mendes, and D. Colombo, "Evaluation of rock integrity during well drilling activities using reliability analysis," Journal of Petroleum Science and Engineering, vol. 200, p. 108405, May 2021.

[19] I. Okamoto, X. Li, and T. Ohsumi, "Effects of Supercritical CO2 on the Integrity of Cap Rock," in Greenhouse Gas Control Technologies - 6th International Conference, Elsevier, 2003, pp. 483–488.

[20] S. Jia, "Bean Centrifuge Modelling of Caprock Integrity," University of Alberta, 2021.

[21] J. D. Murff, "The geotechnical centrifuge in offshore engineering," Proceedings of the Annual Offshore Technology Conference, vol. 1, pp. 675–689, 1996.

[22] A. B. Cooke and R. J. Mitchell, "Soil column drainage modelling using a geotechnical centrifuge," Geotechnical Testing Journal, vol. 14, no. 3, pp. 323–327, 1991.

[23] D. N. Singh, S. J. Kuriyan, and V. Madhuri, "Application of a Geotechnical Centrifuge for Estimation of Unsaturated Soil Hydraulic Conductivity," Journal of Testing and Evaluation, vol. 29, no. 6, pp. 556–562, 2001.

[24] D. N. Singh and A. K. Gupta, "Falling Head Hydraulic Conductivity Tests in a Geotechnical Centrifuge," Journal of Testing and Evaluation, vol. 29, no. 3, pp. 258–263, 2001.

[25] O. Oung et al., "Investigation of a european network of geotechnical centrifuge on multiphase flow," International Journal of Physical Modellin in Geotechnics, vol. 1, pp. 01–14, 2005.

[26] J. Nayser, E. Pooley, and S. Springman, "Modelling of double porosity clays in a mini-centrifuge," International Journal of Physical Modellin in Geotechnics, vol. 1, pp. 15–22, 2009.

[27] T. E. Noble and J. M. Dixon, "Structural evolution of fold-thrust structures in analog models

deformed in a large geotechnical centrifuge," Journal of Structural Geology, vol. 33, no. 2, pp. 62–77, 2011.

[28] M. Rojhani, M. Moradi, M. H. Ebrahimi, A. Galandarzadeh, and S. Takada, "Recent developments in faulting simulators for geotechnical centrifuges," Geotechnical Testing Journal, vol. 35, no. 6, pp. 924–934, 2012.

[29] M. B. Dusseault, "Stress Changes in Thermal Operations," in SPE International Thermal Operations Symposium, 1993.

[30] S. Krishnaiah and D. N. Singh, "Centrifuge Modelling of Heat Migration in Soils," International Journal of Physical Modellin in Geotechnics, vol. 3, pp. 39–47, 2004.

[31] M. D. Zoback, Resevoir Geomechanics, 1st ed. New York: Cambridge University Press, 2007.

[32] E. Fjær, R. M. Holt, P. Horsrud, A. M. Raaen, and R. Risnes, Petroleum Related Rock Mechanics. Elsevier, 2008.

[33] G. E. King and R. L. Valencia, "Well Integrity for Fracturing and Re-Fracturing: What Is Needed and Why?," in SPE Hydraulic Fracturing Technology Conference, 2016.

[34] B. Carey, "Wellbore integrity and CO2 sequestration." .

[35] W. Ovalle-Villamil and I. Sasanakul, "Assessment of centrifuge modelling of internal erosion induced by upward flow conditions," International Journal of Physical Modelling in Geotechnics, vol. 21, no. 5, pp. 251–267, 2021.

Chapter 4

An Approach to Model Cyclic CO_2 Injection Process in Poorly Cemented Heavy Oil Reservoirs Using a Novel Geotechnical Centrifuge Cell and 3D Printed Rocks

A version of this chapter was accepted for presentation at the GeoConvention 2023, Calgary (AB), 15-17 May 2023; the 15th Annual International Conference on Porous Media - Interpore, Edinburgh (Scotland), 22-25 May 2023; the EOR Technical Collaboration Program – International Energy Agency, Calgary (AB), 26-28 September 2023, the GUSSOW 2023, Banff (AB), 10-12 Octuber 2023, and the SPE Canadian Energy Technology Conference and Exhibition, Calgary (AB), 13-14 March 2024.

4.1. Abstract

Achieving successful CO_2 injection in shallow heavy oil reservoirs requires an understanding of the flow dynamics involving gaseous solvent interaction, subsurface deformation, and drainage behavior around the wellbore. This work outlines the design of an instrumented scaled laboratory experiment, conducted within a 2-meter radius beam geotechnical centrifuge. The primary objective is to emulate the cyclic CO_2 injection into a 3D printed sandstone specimen (i.e. a CHOPS reservoir prototype), honoring key boundary conditions such as radial flow and triaxial stress state.

Sand production during the early CHOPS lifetime (Cold Heavy Oil Production with Sands) eventually results in high-permeability channel-like structures, known as wormholes. In this study, we employed additive manufacturing technology (i.e. 3D printing with actual silica grains) to represent wormholes in unconsolidated sandstone formation (i.e. CHOPS prototype). The experimental setup involved the design and construction of a centrifuge cell, to simulate the multi-phase cyclic CO_2 injection process at the reservoir scale. To emulate the vertical stress from overburden rocks at the top of a shale caprock layer, a loading system was designed into the centrifuge cell. Stress anisotropy in horizontal stresses was introduced through an 8-arm horizontal loading system, similar to a triaxial cell configuration.

Additionally, a sand trap and production unit were included in the experimental setup to collect the collapsed sands and the produced fluids.

In the process of establishing residual water saturation, the CHOPS reservoir prototype underwent sequential saturation with water, dead oil, and live oil (prepared by dissolving CO_2). The experiment initiated with the 400 kg setup spinning inside the geotechnical centrifuge until it reached a stable rotational speed of 120 revolutions per minute; this is equivalent to 30 times gravitational acceleration. The perforations of a scaled wellbore within the reservoir prototype were opened to allow fluid and sand production. We noted that an increase in cohesion of the 3D printed rock reduced the rock failure during the production period, even in the presence of substantial seepage forces and pressure gradients. Structural changes around high-permeability zones and near the wellbore were linked to stress concentration. We additionally included a comparative analysis of formation collapse during heavy oil production with and without CO_2 injection.

The outcomes of our scaled physical experiments offer valuable insights into fluid flow and rock deformation during CO_2 injection into heavy oil reservoirs. The utilization of a geotechnical centrifuge and additive manufacturing technology establishes a platform for experimental exploration of multi-scale, multi-physics processes, addressing challenges related to sampling, flow, and deformation in subsurface systems. In addition to understanding CO_2 injection in heavy oil reservoirs, our modeling approach can be used for broader applications, including H_2 storage and safe disposal of radioactive wastes in subsurface formations.

Keywords

Geotechnical Centrifuge, Triaxial stress state, Radial flow, 3D printing, Erosional channels, CHOPS

4.2. Introduction

The hydrocarbon production from poorly cemented reservoirs subjected to Cold Heavy Oil Production with Sand (CHOPS) induces the formation of erosional channels and dilation zones within the reservoir, primarily due to the substantial production of sand [1]. This leads to significant changes in petrophysical and mechanical parameters, including permeability, porosity, compressibility, fluid saturation, and the rock fabric itself [2]. Despite being a cost-effective technique, CHOPS typically recovers only around 10% of the oil in place [3], prompting engineers to explore enhanced oil recovery methods such as cyclic solvent injection (CSI). In the post-CHOPS stage of the reservoir development, the existing wormholes pose formidable challenges for implementing additional recovery techniques [4]–[6]. Several researchers propose that employing cyclic solvent injection, specifically using CO_2 as solvent, could prove beneficial in enhancing oil recovery [7]. However, successfully adopting this approach requires a better comprehension of the interplay among the wellbore, drainage area, wormholes, multiphase flow, and geomechanical constraints.

Several researchers (e.g. [1] and [8]), suggested that the sand production may create a liquefied sand cavity of a couple of meters around the well, resembling piping or erosional channels, as illustrated in Fig 4-1.

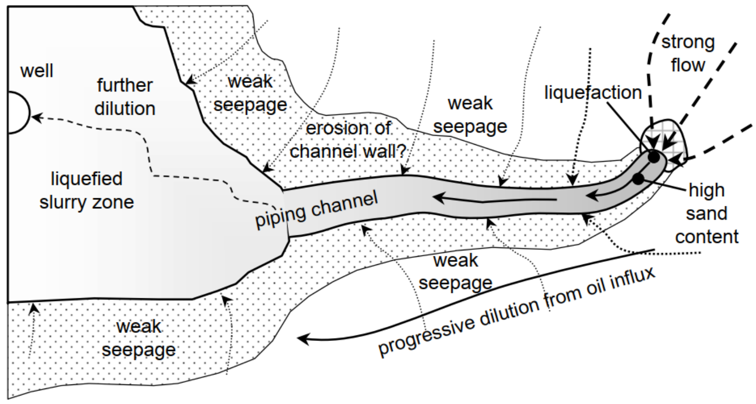

Fig 4-1. Conceptual approach to the morphology of an erosional channel during CHOPS. Taken from [1]

These elongated cavities generate an overburden and radial stress redistribution in the vicinity of the wellbore [1], [9], which is difficult to accurately replicate in small physical models for experimental studies of post-CHOPS reservoirs [10]. Moreover, simulating the erosional channels, commonly referred to as "wormholes", adds another layer of complexity. Given many challenging geomechanical intricacies, a successful laboratory test of any follow up EOR application in post-CHOPS requires to represent a drainage area surrounding the wellbore (scaling-up a laboratory-controlled model), with inherited wormholes and stress anisotropy. Such representation of a drainage area is possible thanks to the use of a geotechnical centrifuge which scales-up the behavior of a model to a prototype size. Unlike the limitations of small physical models commonly employed by researchers, laboratory testing in a centrifuge offers a distinct advantage. It allows for the comprehensive capture of data concerning the formation and behavior of the wormholes only at the perforation but also in the vicinity of the wellbore. This method proves especially valuable as it provides information about the wormholes at scales similar to those encountered in field operations, considering the centrifuge scaling factor [8]. Consequently, this paper aims to incorporate established engineering tools such as a geotechnical centrifuge along with modern technologies (i.e. 3D printing of rocks) to replicate the drainage area, stress distribution, and wormholes during CSI in post-CHOPS reservoirs.

We first summarize the design of the new geotechnical centrifuge cell that can apply triaxial stresses in a cylindrical sample, one of its kind in the world. Subsequently, we introduce the 3D printing process for the post-CHOPS sample, followed by an explanation of experimental procedure to perform cyclic CO_2

injection. Lastly, we discuss the results (e.g. flow regime, geomechanical implications) obtained using the new centrifuge cell. It is noteworthy that this study revolves around the transformation, implementation, and synergy of geotechnical tools, specifically the centrifuge cell and 3D printing of rocks. The distinctive value of this work lies in showcasing a state-of-the-art piece of equipment, potentially applicable in other scenarios that require inclusion of stress states and fluid flow through porous media in the vicinity of wellbore.

4.3. Research Methodology

4.3.1. Design of Centrifuge Cell – GeoTriax

The GeoTriax is a geotechnical centrifuge cell to facilitate the precise application of triaxial stresses to the sample during hyper-gravity spinning conditions of up to 30Gs. This centrifuge cell consists of several interdependent components, functioning together to establish robust and reliable boundary conditions for more accurate results. An in-house design by authors, the GeoTriax serves as a housing unit for the sample, providing boundary conditions and enabling fluid flow. It is placed within the geotechnical centrifuge located at the University of Alberta (Technical description of the 2 meter beam centrifuge is done by [11]), as shown in Fig 4-2-a, the cell dimensions are approximately 85.5 cm in height (including the Parker motors) and 72.5 cm in diameter (including the stress actuators). The net weight of the GeoTriax is approximately 350 kg. It is primarily constructed using steel ASTM A515 (QT-100), with certain components made of aluminum 7075-T6 and rubber (e.g., such as o-rings and the membrane). Fig 4-2-b illustrates a closer look at its parts.

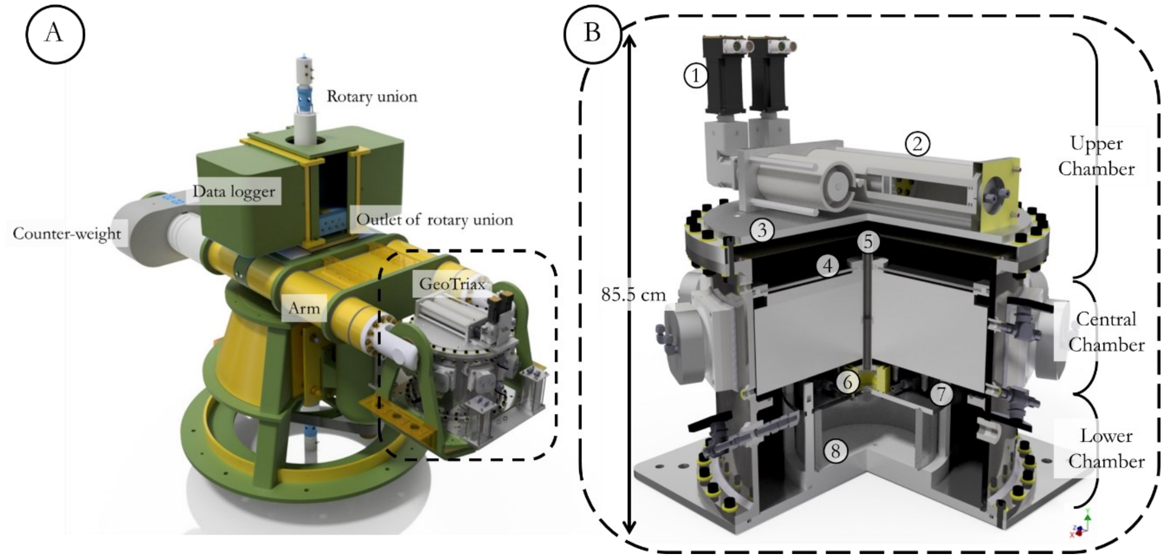

Fig 4-2. a) GeoTriax at the Centrifuge and b) Internal view of GeoTriax. (1) Parker step motor, (2) Piston to displace hydraulic oil, (3) Cell's cap, (4) Membrane, (5) Remotely activated wellbore, (6) Wellbore's activator, (7) Pressure transducer, and (8) Sand-trap

GeoTriax offers two main independent capabilities: one mechanism to apply stresses and another mechanism to enable fluid flow within the sample. These systems can operate independently to provide a wide range of research possibilities. These mechanisms are articulated into three chambers: a main central chamber that houses the sample, an upper chamber responsible for inducing vertical stress, and a lower chamber that contains the sand trap.

Central chamber.

Within this chamber, the CHOPS sample is securely held during the saturation and spinning processes. It features a wellbore in the center of the physical model and eight surrounding stress actuators that apply confining stresses to the sample. Fig 4-3 shows the central chamber, its physical structure and components.

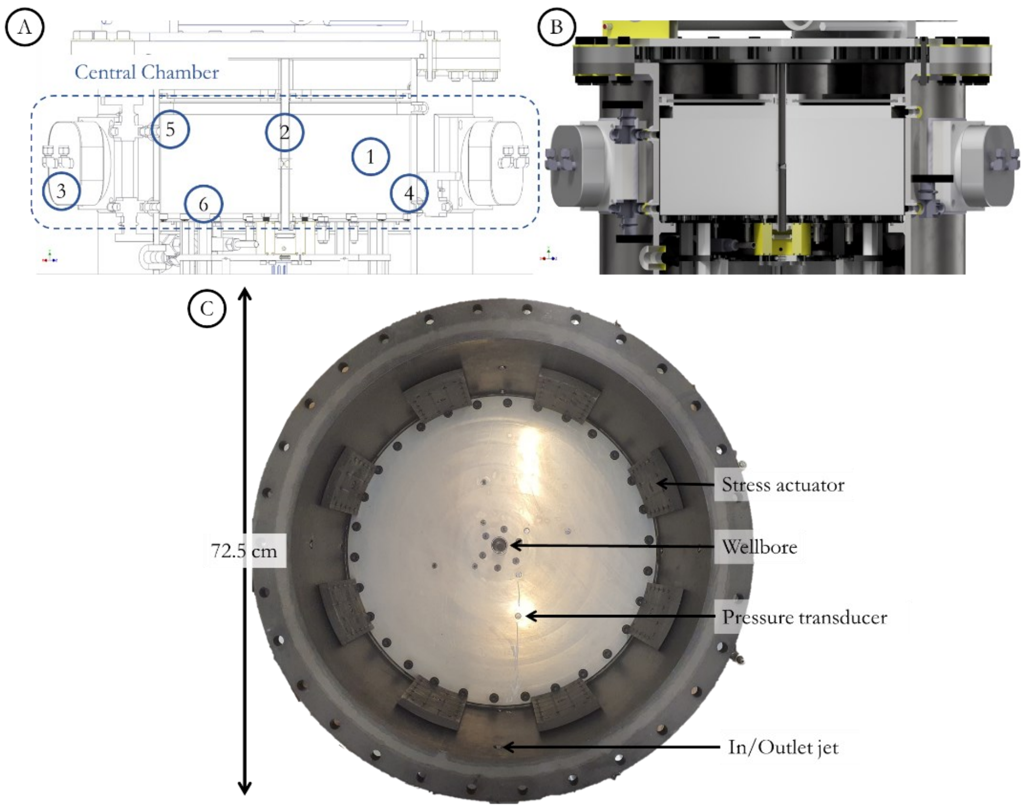

Fig 4-3. a) Central chamber diagram and b) render. The parts in the medium chamber are (1) the sample, (2) the wellbore at the center, (3) Stress actuator, there are 8 around the sample, (4) out/inlet valve used to saturate at the bottom of the sample, (5) Out/inlet valve useful for saturation purposes at the top of the sample, and (6) Plate where the sample is placed. It also holds the pressure transducers. c) Plantar view of the central chamber

The stress actuators play a crucial role in the functioning of the central chamber. These actuators are responsible for applying controlled stresses to the sample in the horizontal plane with a capacity up to 6MPa and 21.6 mm of displacement, thus, GeoTriax can induce stress anisotropy into a cylindrical sample. Fig 3-4 offers a detailed view of the stress actuators, illustrating their design and configuration within the chamber.

As depicted in Fig 3-4, the stress actuators consist of pistons that are driven by injecting an incompressible fluid (i.e. hydraulic oil) at high pressure using the Parker motor BE233DJ-NPSN (gear head RX60-100-S2). The injected fluid exerts pressure on the piston, which in turn applies stress to the sample. To streamline the system, four stress actuators are connected to a Parker motor, while the remaining four are connected to a second Parker motor; such configuration allows to create a true triaxial state. This relationship between the applied pressure over the stress actuator and the stress that is submitted by this to the sample was calibrated as documented in the appendix A.

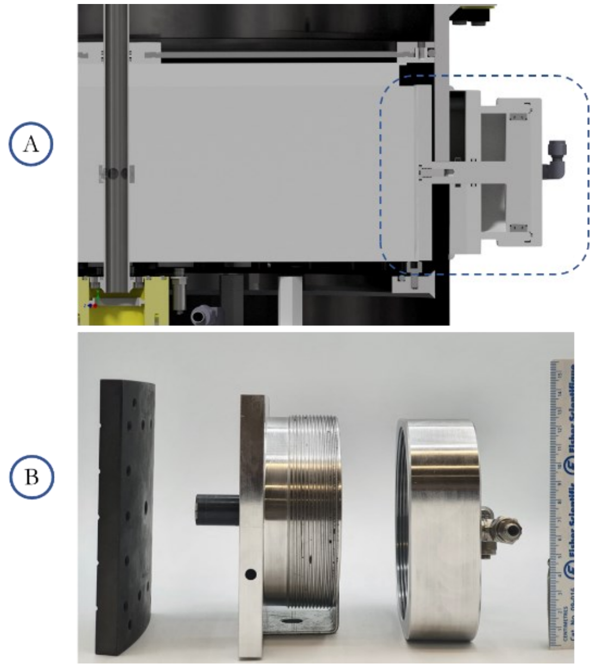

Fig 4-4 a) Detail of stress actuator in a virtual representation and b) an actual one

The second mechanism of the central chamber is related to the opening of the wellbore, which consists of two concentric tubes. The external tube is in direct contact with the sample and features open perforations. The inner wellbore, highlighted in green color in Fig 3-5, is equipped with two sets of perforations. The first set includes pore stones, which allow the flow of fluids while preventing the passage of solid particles into the wellbore. The second set comprises open perforations that, when aligned with the external wellbore's perforations, enables the passage of fluids and solids into the sandtrap and production system.

To activate the displacement of the inner tube, a pressurized fluid is introduced to the piston system. This pressurized fluid exerts downward force on the piston, causing the entire inner tube to descend and aligns the open perforations, the maximum displacement is about 23 mm. This system is engineered to enable sample saturation with the use of the porous stone perforations, that are permeable allowing to flow through them but retaining the sand until the hyper-gravity test.

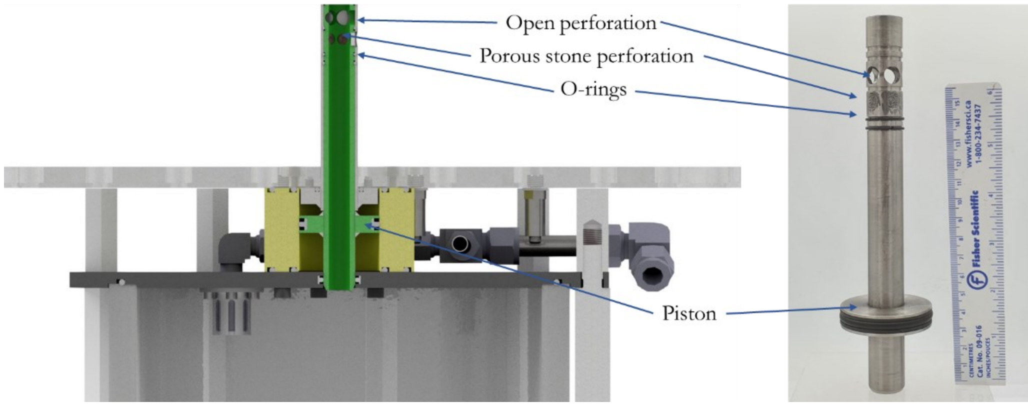

Fig 4-5. Description of the wellbore opening mechanism. Virtual render (left) and actual inner wellbore (right)

Upper Chamber.

The upper chamber applies a vertical stress to the CHOPS sample. It is essentially an empty space that is pressurized pneumatically until the desired pressure is achieved. Fig 3-6 illustrates the components of the upper chamber. Over this chamber, the parker motors and pistons to push the stress actuators are placed. Upon pressurization of the upper chamber, the membrane is activated to function as a barrier between the upper chamber and the main central chamber. The membrane exerts force against the CHOPS sample and generates the vertical stress required for the experiment (Fig 3-6)

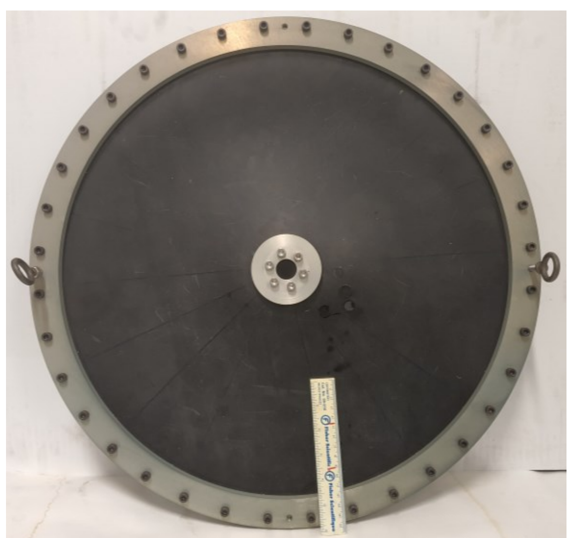

Fig 4-6. Membrane made of Fabric-Reinforced Multipurpose Neoprene Sheet, 3/16" Thick

Lower chamber.

The lower chamber of the GeoTriax accommodates the sandtrap (Fig 3-2), which serves as the initial receptacle for the collected fluids and solids. This element is fabricated with aluminum 7075-T6 + ASTM

A514 (QT-100) and Acrylic. It also houses the pressure transducer, which measures the pressure within the central chamber.

The primary function of the lower chamber is to perform the mechanical separation of sand from the produced fluids. This separation takes place at the exit of the sandtrap, indicated as part A in Fig 3-7. A filter is employed in this process to effectively separate and remove the sand particles from the fluids. The lower chamber also contains dedicated positions for the pressure transducers model AV800 with a maximum capacity of 7MPa (Output 5mV/V, Span Tolerance <±2mV) (Fig 3-7-b), to monitor the pressures within both the sample and the sandtrap. All the pressure transduces used in this test were calibrated as reported in appendix a.

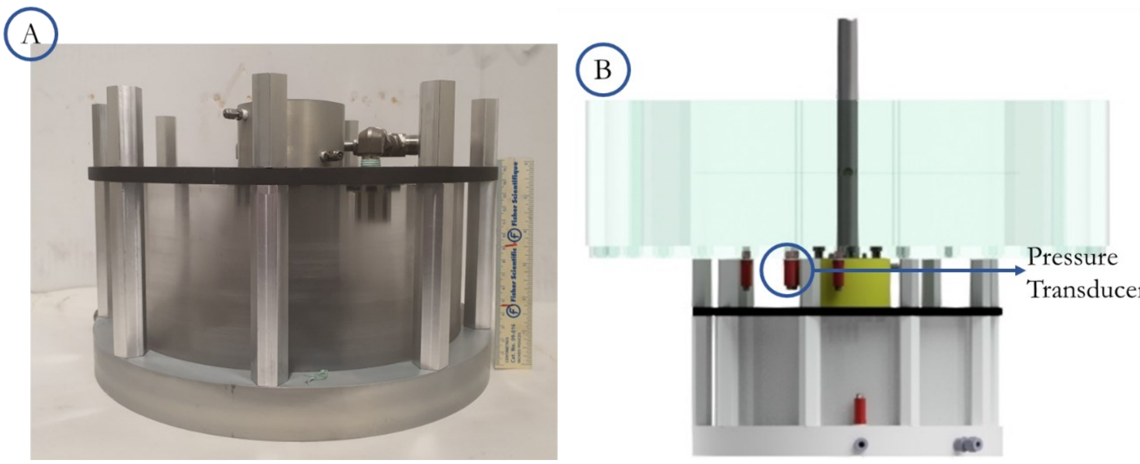

Fig 4-7 a) Sand trap and b) position of pressure transducers

Before a test, the integrity of the whole cell was tested in set of commissioning tests as reported in appendix b

4.3.2. 3D printing of the post-CHOPS reservoir model

Utilizing binder jetting technology, the sample employed in the testing is fabricated to obtain an accurate representation of the inherited wormholes from the CHOPS production. The representation of the wormholes as high permeable channels has been always challenging from a physical representation perspective, and this difficultity may be overcome thanks to the use of 3D printing of rock analoges. The GeoPRINT facility developed by the Reservoir Geomechanics Research Group (RG)^2 is equipped with the Ex-One M-Flex printer. The fabrication procedure for this sample follows the methodology outlined in [12]. The 3D printing technology enables to digitally design the CHOPS sample with pre-determined wormholes, and seamlessly translate that design into actual rock sample to perform laboratory experiments.

The CHOPS model is a 3D printed specimen with a binder saturation of 10%. It includes the presence of 16.58 cm wormholes with a diameter of 2 mm, representing the discontinuities and dilated features, expected in actual post-CHOPS reservoirs. To include the presence of the wormholes, the Computed Assitanted Draw file used to print the sample contains two void cavities where sand without binder will be deposit. The diameter of those wormholes was calculated to an equivalent of 5 cm during the hyergravity environment at 30 Gs following the diameters reported in some simulations (As shown in the Chapter 1). In the tested model, a generic prototype with simplified wormholes was used to simulate the behavior of a post-CHOPS reservoir. More complex patterns and petrophysical properties can be the subject of future studies.

Fig 3-8-a illustrates the dimensions of the 3D printed model, the wellbore and wormholes.

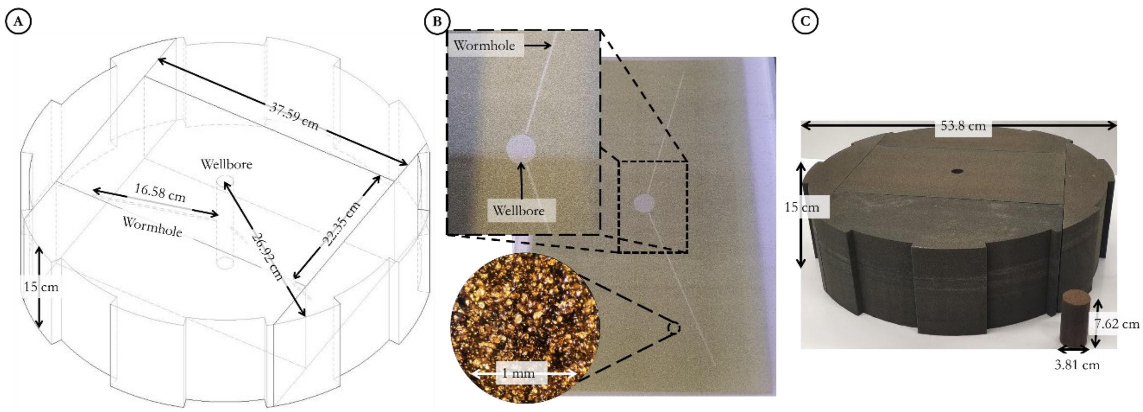

Fig 4-8. a) Sample diagram and its measurements. b) A layer of the sample during printing, highlighting the wormholes and wellbore. c) The whole 3D printed sample and next to it, a standard sample is displayed for comparison purposes

Due to the size limitations of the printer box, the sample was printed as five individual pieces, which collectively formed the complete post-CHOPS model. Fig 3-8-c provides a visual representation of the printed sample in comparison to a typical 1.5 x 3 inch core sample; also shown is a single layer during the printing process (Fig 3-8-b), where the included wormholes and a single wellbore can be observed. The sample used in the experiment includes pre-designed lateral areas for the eight stress actuators.

According to Gomez [13], with a binder saturation level of 10%, the sample exhibits a porosity of 46.7%. Its unconfined compressive strength (UCS) measures at 14.78 MPa, with a peak strain of 1.06%. The Young's modulus is estimated to be 1.70 GPa, and the Poisson's ratio is determined to be 0.19. These properties provide valuable insights into the mechanical behavior of the sample under testing conditions. Studies on samples with a higher binder saturation of 20% have demonstrated a permeability range of

800 to 1000 mD under low effective confining stress conditions [12] with permeability decrease at higher the effective stress.

4.3.3. Experimental Procedure of CSI Post-CHOPS

In this test, CO_2 was dissolved in canola oil to prepare live oil at high pressure and to saturate the CHOPS sample. To prepare the CO_2 saturated live oil, we built a fluid mixing and injection unit (Fig3-9-a) by connecting a set of 8 accumulators with a combined capacity of more than 9 liters, and pushed by a Quizix Pump Serie 6000. The fluid mixing and injection unit is connected to the fluid supply line for the GeoTriax. Each accumulator is equipped with individual valves that assure precise control over the injection process. To prepare the live oil, the accumulators were initially filled with canola oil (i.e. dead oil). Subsequently, CO_2 was injected into the accumulators at a pressure of 3 MPa. The whole mixing and injection unit was capable to be rotated upside-down in 30 minutes intervals to facilitate the dissolution of CO_2 into canola oil. The mixing process was repeated multiple times until the internal pressure of the accumulators stabilized. A sample was collected from the accumulator and flashed into a low-pressure visual vessel to confirm the quality of saturated oil (Fig 3-9-b).

Fig 3-9-b shows the release of the dissolved CO_2 within the saturated oil sample when it transitions from a high-pressure state to a relatively lower pressure. Under laboratory conditions, the bubbles of dissolved CO_2 move slowly and vertically towards the surface because of buoyancy. The saturation process of the post CHOPS model starts by injecting the foamy oil into the sample until a stable pore pressure of approximately 2.2 MPa is reached. The saturation process and increase of pore pressure are conducted in steps with increasing the confining stresses in order to maintain an isotropic stress state at 2.5 MPa.

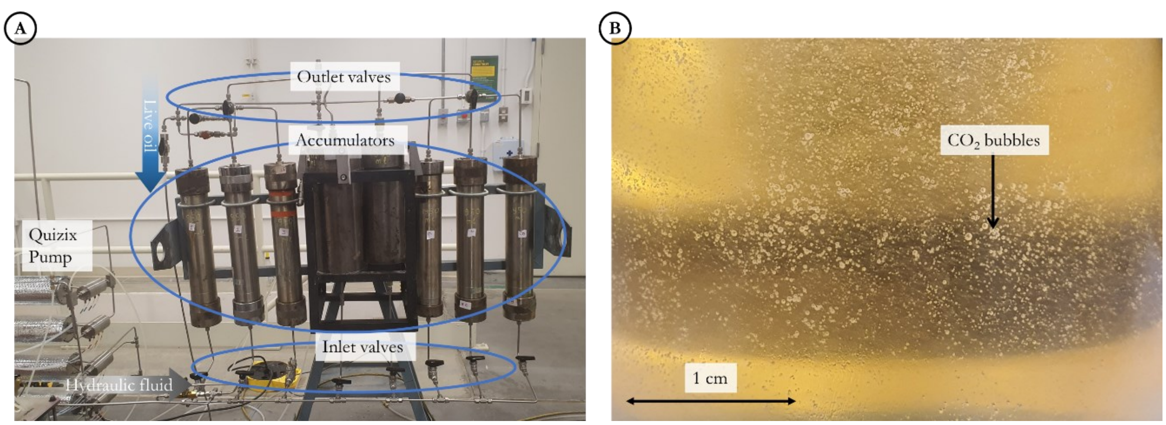

Fig 4-9 a) Accumulators, and b) Saturated oil sample, flashed into a low pressure visual vessel, exhibits foamy oil behaviour

Following the complete saturation of the sample with live oil, the GeoTriax cell was carefully placed into the geotechnical centrifuge using a crane. Subsequently, all the sensors were connected to the central data acquisition system, ensuring comprehensive monitoring during the spinning process to produce the hyper-gravity effect. The spinning process was initiated at 30 Gs (120 rpm). Once a constant acceleration was achieved and the system was confirmed to be stable, the wellbore was remotely opened to initiate the fluid production phase. At hyper-gravity, the bubbles in the foamy oil scale up, as does the pore space, maintaining the size ratio they had in the prototype.

It is important to point out that the size of the bubbles is a function of the pressure. During the test, and thanks to the geometry of the sample and the radial flow, the fluid has a pressure distribution that leads to a bubble size distribution. It means that the bubbles near the wellbore are larger than those at far way from it.

The foamy oil produced during the test is collected and stored in external acrylic accumulators that are affixed to the GeoTriax cell. Continuous monitoring of pressure in the GeoTriax cell and these accumulators ensures accurate data acquisition and a better understanding of the production phase under hyper-gravity conditions. Further details about the experimental procedure can be found in appendix c. Additionally, in appendix d, there is a list of tests that went wrong and the main cause of failure for references of the reader.

4.4. Results and Discussion

4.4.1. Review and Analysis of Fluid Production

Throughout the entire spinning process (hyper-gravity environment), the pressure within the GeoTriax apparatus was monitored using four pressure transducers (PTs) positioned beneath the sample, along with an additional PT located in the sand trap. The recorded pressure data from both the sample and the external accumulators provide insights into the pressure variations during the spinning process (Fig 3-10). The corresponding gravity multiplier is also depicted in Fig 3-10 as a reference for the experimental conditions.

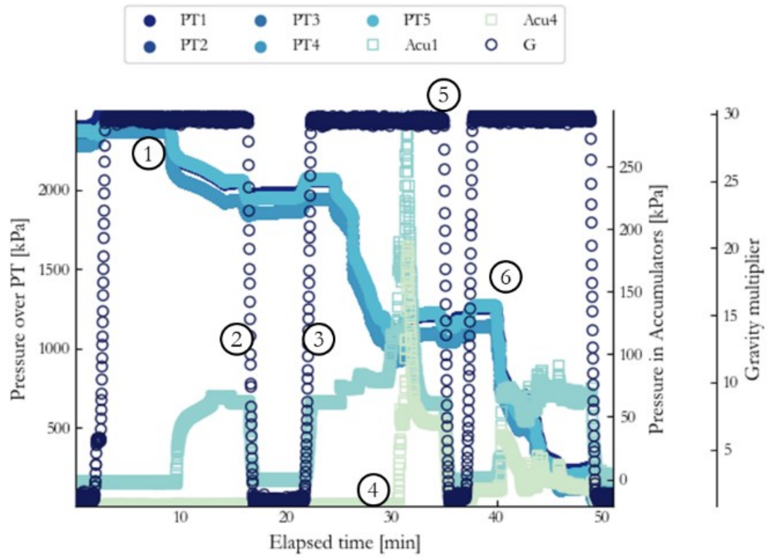

Fig 4-10. Pressure behavior during the spinning at 30G's

Around the 10-minute mark, the wellbore was opened, leading to the release of reference pressure from the back pressure regulator. This orchestrated sequence triggered the onset of production, resulting in an observable elevation in hydrostatic pressure within the external acrylic accumulator 1 (Acu1), placed to collect produced fluids. Simultaneously, the pore pressure experienced a decrement (marked as Point 1 in Fig 3-10). A brief intermission, designated as Point 2, was employed to assess the integrity of the system's sealing characteristic by observing constant pore pressure in the GeoTriax cell. The spinning was recommenced, which resulted in a discernible surge in flow and a noticeable change in the pressure of Acu1. At the 30-minute mark, the fluid progressively filled in each succeeding accumulators; four external acrylic accumulators were attached to GeoTriax to collect the produced fluids. This is evident as the pressure in the final accumulator, Acu4, experienced a notable increase (Point 4). At Point 5, all four external accumulators reached their full capacity, that could be confirmed through the dedicated streaming system. A temporary pause ensued, halting the geotechnical centrifuge to empty the four accumulators. The experiment then entered a "second spin", in which the gravity conditions remained at a constant 30Gs, while production resumes with heightened momentum.

An intriguing observation can be seen in Fig 3-10 that relates to the declining trend of pressure within the external accumulators. Note that the pressure in the accumulators is estimated based on the cumulative fluids column in the accumulator registered by the pressure transducers (PTs). To investigate this experimental observation, video images of the accumulator behavior during spinning were used to calculate the pressure attributed to the fluid column at 30Gs by measuring the height of the fluid columns. The calculated pressure was compared with the pressure measurement obtained from the PTs. The results are illustrated in Fig 3-11, which provide a perspective on the dynamics of the pressure from fluid column and the measurement from the PTs. It is important to emphasize that the available information pertains specifically to two out of the four accumulators. Specifically, data was collected from the initial and final accumulators where dedicated PTs and video cameras were positioned to record and monitor the fluid production phase.

The increase and decrease of pressure in the fluid column (Fig 3-11) seem to be related to the variability of density within the foamy oil during production phase. The density variation is caused due to the exsolution of CO_2 while the fluid behaves as foamy oil. The amount of disconnected CO_2 bubbles leads to a reduction in fluid density, and the recorded pressure; the exsolution of CO_2 from oil seems to be a transient process.

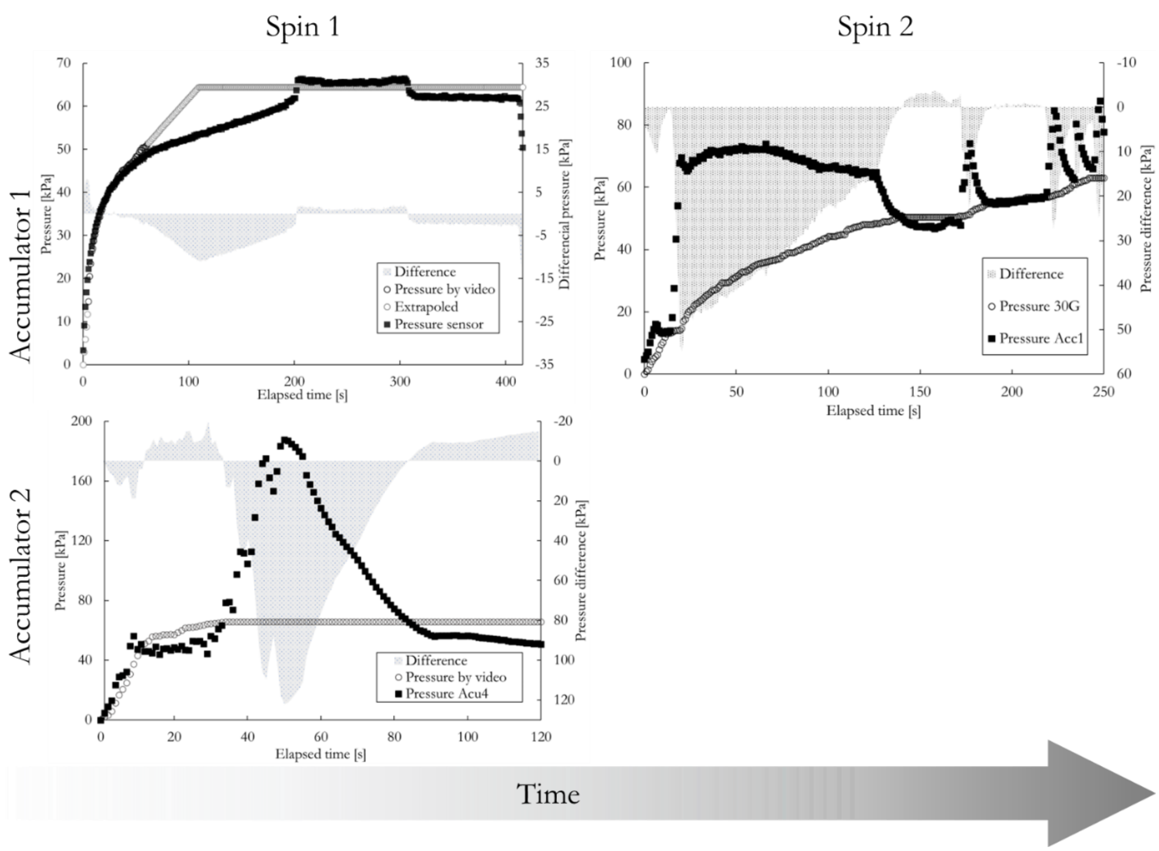

Fig 4-11. Pressure in the accumulators during spinning

Fig 3-12 shows the results of fluid production and the corresponding pressure in the accumulators. Note that the time and production axis are scaled at the 30 Gs acceleration rate, which helps to better see the dynamics of fluid production and changes in pressure within the accumulators. To scale these values into a prototype space some scaling factors reported at the literature are used [14]. For the distance a scale of

1:30 was used, for volume a scale of 1:30², and for time 1:30² were applied to scale from model to prototype space.

Noticeable patterns emerge in both accumulators, with instances where pressure levels rise without a corresponding increase in flow rate. This observation could be attributed to pressure pulses, originating from the post-CHOPS cell and subsequently propagating throughout the external acrylic accumulators.

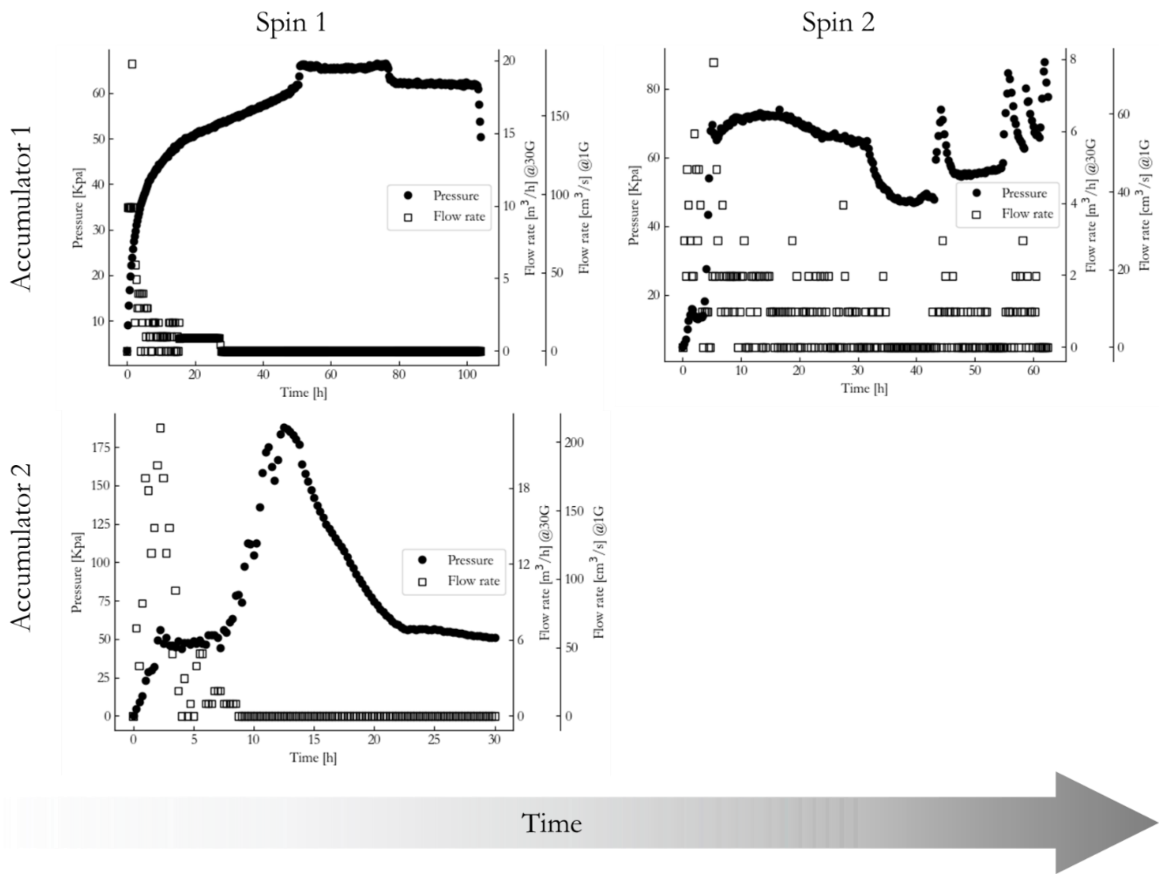

Fig 4-12. Production vs pressure in accumulators 1 and 4

4.4.2. Discussion on the Established Flow Regimes

To get insight on the flow regime inside the CHOPS protorype, we used the pressure data during the geotechnical centrifuge test to peform a transient presure analysis, i.e. a drawdon well test. Drawdown tests involve a sequence of bottomhole pressure measurements taken during a period of flow at a constant production rate. Prior to the flow test, the well is shut in for a sufficient duration to allow the pressure to stabilize throughout the formation and reach static pressure [15].

In a homogenous reservoir, the pressure during a drawdown test is governed by Equation (3-1) [15]:

$$p_{wf} = p_i + 162.6\frac{qB\mu}{kh}\left[log\left(\frac{1688\varphi\mu c_t r_w^2}{kt}\right) - 0.869s\right] \quad (4\text{-}1)$$

where p_{wf} is the bottom hole pressure [psi], p_i is the initial pore pressure of the reservoir [psi], q is the flow rate [bbl/day], B is the volumetric factor [bbl/STB], μ is the viscosity [cP], k is the permeability [mD], h is the reservoir thickness [ft], φ is the porosity, c_t is the total compressibility [psi^{-1}], r_w is the wellbore radious [ft], t is the time [h], and s is the skin. In Eq. (3-1), the independent variable is time, and the remaining variables can be represented as one unknown factor, leading to Eq. (3-2):

$$p_{wf} = p_i + m\log(t) \quad (4\text{-}2)$$

where m represents the slope of a straight line observed during the middle time region (MTR), this provides significant information about the reservoir properties [16]. To analize the drawdown test analysis, we obtained a diagnostic semi-log plot (Fig 3-13-a) which illustrates a typical drawdown behavior agianst the prototype time. The linear trend in the MTR suggests the possibility of radial flow regime around the wellbore.

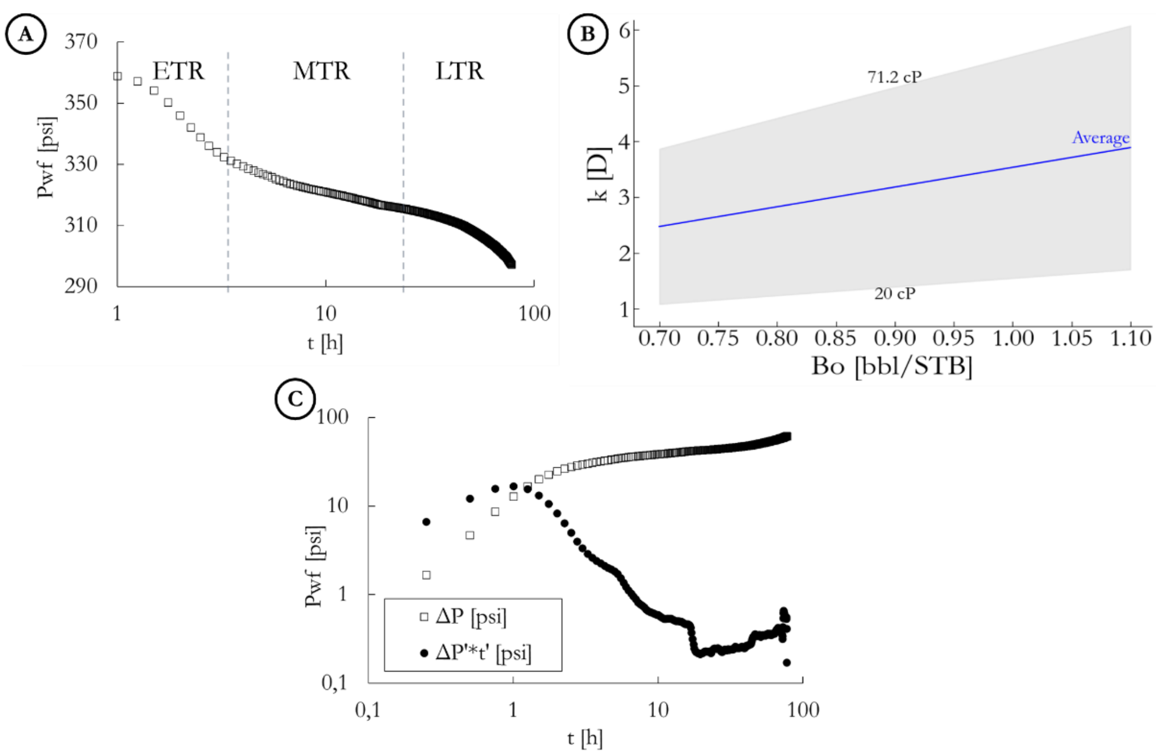

Fig 4-13. a) Pressure vs log t during the test at prototype space. b) Estimated permeability from drawdown test, c) Derivative of pressure at prototype space

The permeability (k) can be determined from the slope of pressure during the MTR straight line using the equation:

$$k = 162.6\frac{qB\mu}{mh} \tag{4-3}$$

We assumed values of B (formation volume factor) and μ (viscosity) of the fluid are subject to change due to the foamy oil behavior. That is why the estimated permeability is presented as a range to account in Fig 3-13-b. The maximum viscosity (71.2 cP) and formation volume factor (B) values were taken for the pure canola oil and heavy oil, respectively. However, the actual viscosity and volumetric factor in the test are expected to be significantly lower due to the presence of dissolved CO_2 in the oil. The permeability of the sample is estimated to fall between 1 and 2 Darcy; this value is consistent with the experimental measurement for similar 3D printed rocks reported by Gomez, Chalaturnyk, & Zambrano-Narvaez [12].

The shape of the pressure derivative plot in Fig 3-13-c is characteristic of a dual porosity system [17]; it is commonly referred to as the dual porosity signature. In such reservoirs, the fluid is stored in the matrix of the porous media, while the flow initially occurs through fractures, i.e. high permeability pathways, that are connected to the wellbore. The pressure derivative plot indicates that during the hyper-gravity process, the flow pattern resembles a dual porosity radial flow; fluid enters the wormholes from non-wormhole (matrix) domain, and then moves towards the wellbore through the present wormholes, very similar to the flow behavior observed in naturally fractured reservoirs.

To complement the pressure analysis, we calculated the beginning and end of the MTR region, corresponding to the radial flow regime. The radius of investigation can be estimated using Equation 3-4 [16]:

$$r = \sqrt{\frac{kt}{948\varphi\mu c_t}} \tag{4-4}$$

We use the permeability derived from Equation (3) and Fig 3-13-b; B_o was 0.8, k is 1200 mD, and μ is 20 cP, φ is 35.7%. The compressibility of 3D printed rocks is reported as high and equal to 3.12E-4 psi^{-1} [12]. A summary of the times at which the radial flow begins and ends, along with their respective radii, is presented in Table 4-1.

Table 4-1. Radius of investigation where the radial flow could happen

Time [h]	Radius [ft](m)
5	5.2 (1.5)
40	15.07 (4.6)

At t = 40 hours, corresponding to a radius of approximately 4.6 m, the distance closely matches the wormhole that was printed inside the sample. This suggests that CHOPS reservoirs could be assumed as double porosity models and it brings our centrifuge model closer to replicating the actual flow regimes in CHOPS reservoirs. The ability to emulate such complex flow behavior in the laboratory is an advancement in understanding the behavior of hydrocarbon reservoirs and provides valuable insights for the oil and gas industry.

Lastly, we analyzed the pressure differentials among the sensors, given their distinct positions within the CHOPS prototype. This analysis helped to capture variations arising from different heterogeneities, such as discontinuities in the sample blocks and wormholes. For reference, the pressure of sensor 1 is depicted in Fig 3-14. The pressure difference between sensor 1 and sensor 3 indicate that the wormholes function as highly permeable channels during production phase. As time progresses, this pressure difference increases, signifying that the fluid encounters less resistance to flow through sensor 3 compared to sensor 1. Notably, even though sensor 1 and sensor 3 are equidistant from the wellbore, sensor 1 is positioned within a continuous reservoir, whereas sensor 3 lies beneath a wormhole.

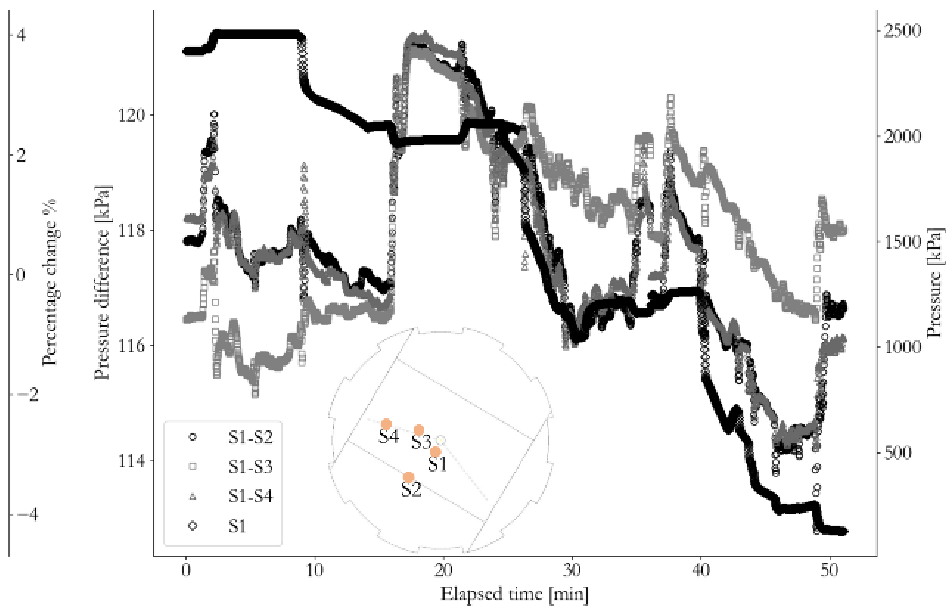

Fig 4-14. Pressure differences between sensors

Furthermore, the disparities between sensor 1 and sensor 2, as well as between sensor 1 and sensor 4, exhibit synchronicity. This alignment suggests that the presence of a discontinuity between blocks, where sensor 2 is situated, and the end of a wormhole, where sensor 4 is placed, both act as continuous porous mediums. Notably, the pressure difference between sensor 1 and sensor 4 exhibits sporadic peaks at various instances, indicating the dynamic flow behavior in these areas and the possible coalescence of gas bubbles in the tip of the wormhole.

4.4.3. Geomechanics Aspects

The rationale behind applying stress anisotropy to the sample during the hyper-gravity test was to understand the influence of stress anisotropy on the behavior of pre-existing wormholes. This approach aimed to compare and contrast the results with findings from previous experiments. A numerical model of the post-CHOPS prototype was built using RS3 software by RocScience to predict the mechanical behavior under the applied stress state and the distribution of stresses around the wellbore. The simulation was conducted replicating the incremental loading and associated changes in vertical and horizontal stresses before the centrifuge hyper-gravity process. Fig 3-15 provides an overview of results, that shows a smooth distribution of stresses around the wellbore, with most of the mechanical impact to occur near the horizontal stress actuators. It is important to note that the numerical simulations only assumed mechanical processes; they did not incorporate the impacts of flow and pore pressure (i.e. hydromechanical behavior).

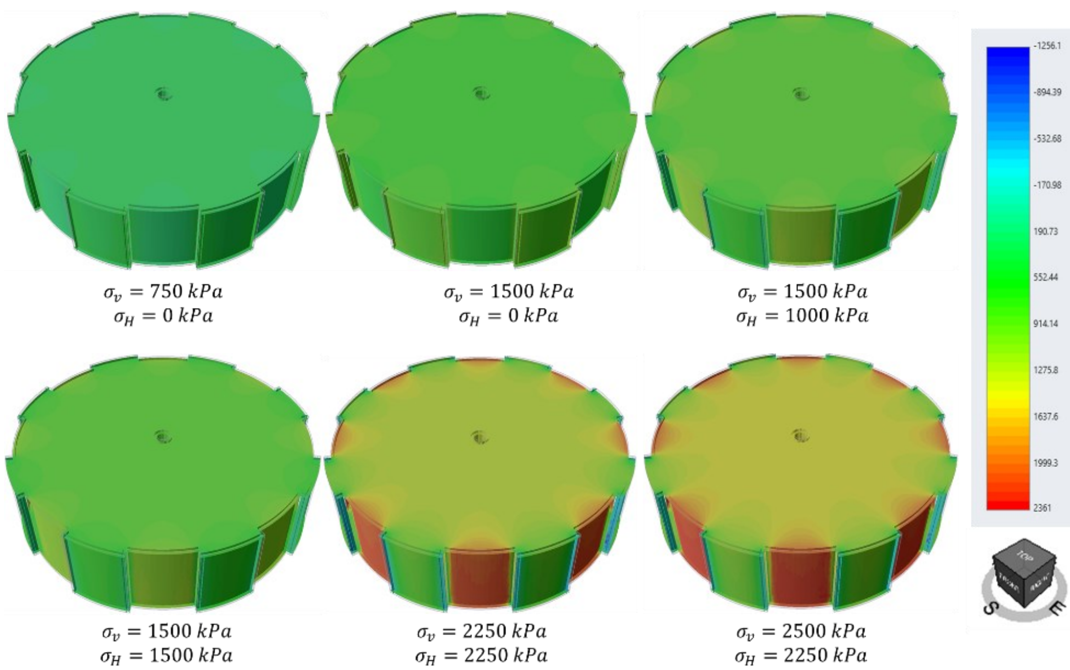

Fig 4-15. Modelling of the loading process by stages before spinning

In the physical prototype, geomechanical considerations come into play when examining the deformations during and after the centrifuge test; we observed two distinct sets of cracks (Fig 3-16) once the post-CHOPS setup was opened.

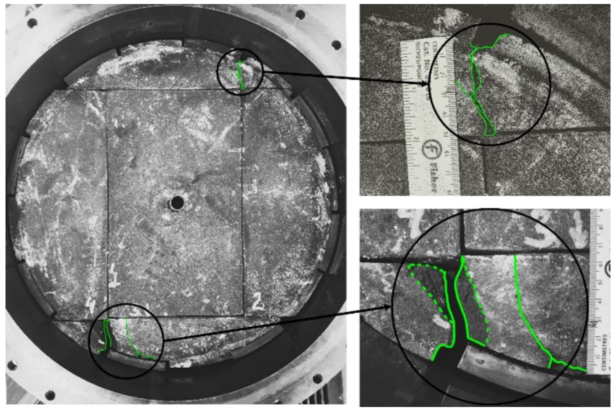

Fig 4-16. Cracks in the sample after the spinning and production

In both scenarios, these fractures exhibit a distinct pattern, originating from the stress actuators and extending towards the juncture where two intact rock blocks meet. It is reasonable to attribute the creation of these cracks to the concentration of shear forces along the edges of the stress actuators, a phenomenon caused by their unique shape and integration within the rock. Notably, the presence of these cracks also serves as an indication of the effectiveness of the stress actuators because fractures would only manifest if the stress actuators functioned as intended.

We noted no substantial sand production, even in the vicinity of the wormholes. This observation underscores the competence of the printed rock sample in maintaining its structural integrity. However, it also implies the necessity of conducting analogous tests on less competent rock samples (e.g. lower binder saturation), particularly if there is a pronounced interest in solid production. Previously, Pereira [18] and Layeghpour [8] explored the geomechanics of CHOPS production in a specimen made from loose sands; they observed an inverse conical cavity around the wellbore after sand production (Fig 3-17).

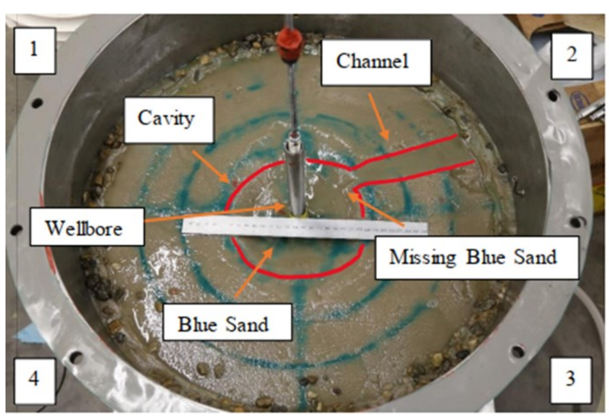

Fig 4-17. Planar view of the cavity after sand production around a wellbore. Taken from [17]

This phenomenon can be attributed to the fact that detaching a sand grain necessitates the predominance of viscous forces over resistance forces related to shearing and tension on a yielding rock [19]. The resistance force can be estimated with the approach of Fjær et al. [19] assuming a material that responds to yielding as forecasted by the Mohr-Coulomb criteria. Basically, the resistance will be performed by four neighboring grains in shearing and one grain in tension, as shown schematically in Fig 3-18. Mathematically, the resistance can be written as:

$$F_r = \left(\frac{d_g}{2}\right)^2 [4S_0 + \mu(2\sigma'_z + \sigma'_\theta) + T_0] \tag{4-5}$$

where, F_r is the resistance force [N], d_g is the diameter of the grain [m], S_0 is the cohesion [Pa], σ'_z and σ'_θ are the effective axial and tangential stresses at the cavity wall, μ is the internal friction angle, and T_0 is the tension strength. Equation (5) was employed to assess an individual grain at the surface of a cavity. When the resistance force from equation (5) was plotted against the drag force generated by the viscous fluid, the points at which the sand grain would undergo yielding were directly correlated with the viscosity and velocity of the fluid (Fig 3-18).

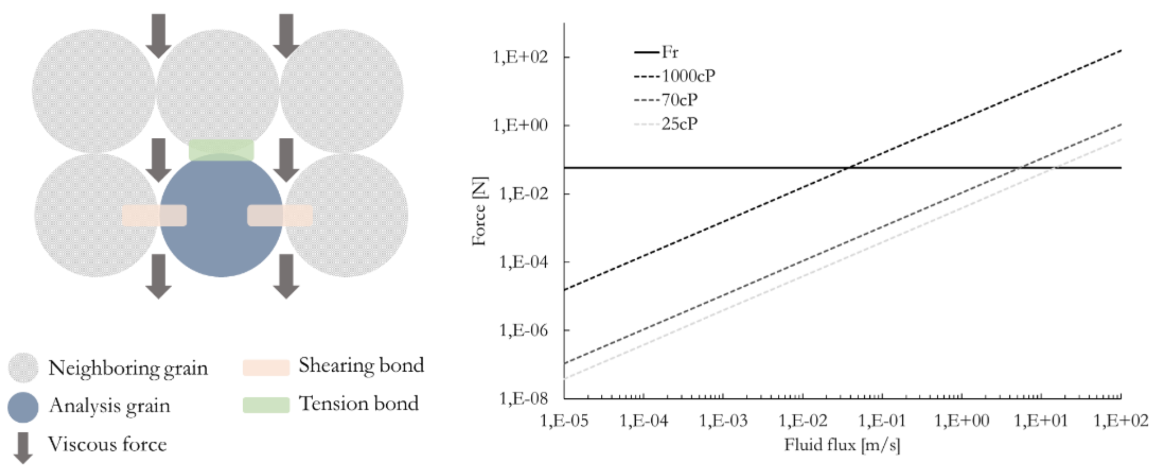

Fig 4-18. Yielding of a single grain at the wall of a cavity. Schematic representation (left) and force resistance against viscous forces at different velocities and viscosities (right)

Based on Fig 18, it can be inferred that the formation of conical cavities was not a consequence of any mechanical impact but rather the outcome of viscous forces dragging sand. This phenomenon is attributed to the low strength of loose sand, making it susceptible to formation under almost any fluid flux. This discussion is important since authors as Tremblay & Oldakowski [20] suggest that the main driving mechanism in the growth of the wormholes is the mechanical failure of the reservoir and the following sand production.

4.5. Conclusions and Remarks

This work presents the design, development and implementation of a novel centrifuge cell to model the cyclic CO_2 injection process into a poorly cemented post-CHOPS reservoir. This centrifuge cell is capable to induce triaxial stress states within a large cylindrical sample while incorporating multi-phase flow processes at high rotational speed, a capability that has not been available before and that allows us to observe phenomena that would be difficult at small samples that are usually available in laboratory testing.

In contrast to previous studies involving geotechnical centrifuges for CHOPS reservoir investigations [18], [21], the current research demonstrates an extended scope. By allowing for the testing of rocks under triaxial stress conditions, the study introduces a crucial geomechanical dimension that bears significance due to its connection with sand production dynamics. Importantly, the research unveils that enhancing the sample's strength effectively suppresses the occurrence of conical cavities, as observed in earlier works. This highlights the relevance of further research in the representation of poorly-cemented sandstones.

The analysis of pressure transients yields insights about the flow regime. Discontinuities between distinct sample blocks appear to exert minimal influence on the flow regime, hinting at their likely impact being confined to the wellbore connection, rather than the reservoir itself. Conversely, the presence of wormholes significantly affects the flow dynamics, underscoring the sample's dual porosity characteristics. Additionally, the estimation of permeability through drawdown test interpretation is demonstrated to align remarkably well with laboratory measurements, attesting to the method's accuracy.

Future test may include the utilization of different fluids, injection/production cycles, multiple wormholes geometries, and the use of optic sensors to measure the bottom hole pressure.

In summary, this study advances the field by introducing a purposed-designed centrifuge cell that not only enhances the understanding of rock behavior under triaxial stress states but also contributes to unraveling the intricate interplay between geomechanics and fluid flow dynamics in complex reservoir systems. The insights gained from this investigation have the potential to influence future research and enhance our comprehension of the subsurface processes governing oil and gas production.

4.6. Statements and Declarations

Conflict of interest: The authors declare no competing interests.

4.7. Acknowledgements

This work was partially supported by Mitacs through the Mitacs Accelerate program. We gratefully acknowledge the Heavy Oil Research Network program, managed by the Petroleum Technology Research Centre, Regina for providing partial funding of this research project. We gratefully acknowledge the NSERC/Energi Simulation Industrial Research Chair in Reservoir Geomechanics in Unconventional Resources for additional funding, and the Rocscience Inc. for providing the geotechnical software package.

4.8. References

[1] M. B. Dusseault, "CHOPS: Cold Heavy Oil Production with Sand in the Canadian heavy oil industry," Waterloo, 2002.

[2] D. F. Cartagena-Pérez, G. A. Alzate-Espinosa, and A. Arbelaez-Londoño, "Conceptual evolution and practice of sand management," *Journal of Petroleum Science and Engineering*, vol. 210, Mar. 2022.

[3] A. Rangriz Shokri and T. Babadagli, "A sensitivity analysis of cyclic solvent stimulation for post-CHOPS EOR: Application on an actual field case," *SPE Economics and Management*, vol. 8, no. 4, pp. 78–89, 2016.

[4] B. Yadali Jamaloei, R. Kharrat, and F. Torabi, "Analysis and correlations of viscous fingering in low-tension polymer flooding in heavy oil reservoirs," *Energy and Fuels*, vol. 24, no. 12, pp. 6384–6392, 2010.

[5] Z. Lin, "Experimental Study About Radial Viscous Fingering in Heavy Oil Reservoir," University of Regina, 2020.

[6] D. W. Zhao, J. Wang, and I. D. Gates, "Thermal recovery strategies for thin heavy oil reservoirs," *Fuel*, vol. 117, pp. 431–441, Jan. 2014.

[7] G. Coskuner and H. Huang, "Enhanced oil recovery in post-CHOPS cold heavy oil production with sand heavy oil reservoirs of Alberta and Saskatchewan part 2: Field piloting of cycling solvent injection," *Society of Petroleum Engineers - SPE Canada Heavy Oil Conference 2020, CHOC 2020*, vol. 3, 2020.

[8] S. Layeghpour, "Geotechnical centrifuge experiments to improve understanding of sand production from heavy oil reservoirs," University of Saskatchewan, 2021.

[9] M. Dusseault and F. J. Santarelli, "A conceptual model for massive solids production in poorly-consolidated sandstones," in *ISRM International Symposium*, 1989, pp. 789–797.

[10] K. Oldakowski and R. P. Sawatzky, "Direction of wormholes growth under anisotropic stress," in *SPE Canada Heavy Oil Technical Conference*, 2018.

[11] G. Zambrano-Narvaez and R. J. Chalaturnyk, "The new GeoREF geotechnical beam centrifuge

at the University of Alberta, Canada," in *Physical Modelling in Geotechnics*, C. Gaudin and D. White, Eds. London: Taylor & Francis Group, 2014, pp. 163–167.

[12] J. S. Gomez, R. J. Chalaturnyk, and G. Zambrano-Narvaez, "Experimental Investigation of the Mechanical Behavior and Permeability of 3D Printed Sandstone Analogues Under Triaxial Conditions," *Transport in Porous Media*, vol. 129, no. 2, pp. 541–557, 2019.

[13] J. S. Gomez, "Mechanical Properties Characterization of Printed Reservoir Sandstone Analogues," 2017.

[14] R. N. Taylor, Geotechnical Centrifuge Technology, 1st ed. London: Taylor & Francis, 1995.

[15] T. Ahmed and P. McKinney, *Advanced Reservoir Engineering*, 1st Ed. Elsevier, 2005.

[16] J. Lee, *Well Testing*. Society of Petroleum Engineers, 1982.

[17] H. Jourde, F. Cornaton, S. Pistre, and P. Bidaux, "Flow behavior in a dual fracture network," *Journal of Hydrology*, vol. 266, no. 1–2, pp. 99–119, Sep. 2002.

[18] M. Pereira, "A Physical Model to Assess Sand Production Processes during Cold Heavy Oil Production with Sand," University of Saskatchewan, 2021.

[19] E. Fjær, R. M. Holt, P. Horsrud, A. M. Raaen, and R. Risnes, *Petroleum Related Rock Mechanics*. Elsevier, 2008.

[20] B. Tremblay and K. Oldakowski, "Modeling of wormhole growth in cold production," *Transport in Porous Media*, vol. 53, no. 2, pp. 197–214, 2003.

[21] H. H. Vaziri and L. Lemoine, "Strong support for significant productivity boost through sand production," in *4th North American Rock Mechanics Symposium, NARMS 2000*, 2000, pp. 295–302.

Chapter 5

Mechanical and Hydraulic Characterization of 3D Printed Rocks at Low Binder Saturation as Analogs to Poorly Cemented Sandstone Rocks

A version of this chapter was accepted for presentation at the 58th US Rock Mechanics / Geomechanics Symposium – ARMA 2024, Golden (CO), 23-26 June 2024.

5.1. **Abstract**

The utilization of 3D printing technology has garnered considerable attention in various fields for its ability to fabricate complex structures with precision and efficiency. Among the diverse range of materials that have been subjected to 3D printing processes, rocks and geologic formations stand out as a unique and intriguing subject of study. This paper explores the challenges of employing binder jetting technology at its current binder saturation limits to manufacture rock analogs to mimic poorly cemented sandstones, and their hydromechanical characterization.

To obtain well-shaped rock samples, two key adjustments are implemented into the printing process: (i) disabling the compaction roller during printing, and (ii) increasing the vertical layer thickness. These adjustments were employed to counteract the sliding effect between printed layers prior to curing and the surface cracks that occur during the normal printing process. By systematically implementing these modifications, we aimed to optimize the 3D printing process and enhance the quality of the printed samples at very low binder saturation. To assure the printed rock samples can represent poorly cemented sandstone, we conducted a comprehensive mechanical characterization program, including uniaxial compressive strength (UCS) tests, triaxial tests, creep behavior, petrophysical properties, and an investigation of the failure mechanisms. These combined methods allowed us to gain a thorough understanding of the characteristics of 3D printed rocks and their potential applications in geotechnical and petrophysical research, specifically in the context of heavy oil reservoirs.

The experimental results show an average UCS of 2,03 MPa and Young's Modulus of 175,18 MPa for rock samples printed at 5% binder saturation, suggesting their reliability to represent heavy oil reservoirs.

Our examinations revealed high porosity values of approximately 46% and absolute permeability values of 1,77 Darcies, making the 3D printed samples comparable to the heavy oil reservoirs. The Skempton's parameter "B" was estimated 0,73, in line with typical values for poorly cemented rocks. Other observations included a distinctive failure mechanism, characterized by the loss of cohesion at triaxial stress conditions, which highlights the role of internal friction on material's strength. Further, assessments of creep behavior indicated minimal creep in the initial 500 minutes, ensuring the stability of the samples during regular-long tests.

This paper offers insights on the current limitations of 3D printing rocks at low binder saturation and ways to improve their quality and reliability for experimental research. The findings not only validate the application of 3D printed technology for hydromechanical study of poorly cemented rocks, but also provide valuable data for further geotechnical and heavy oil engineering applications.

5.2. **Introduction**

The 3D printing of rocks with actual silica grains involves a series of key steps, each contributing to the successful replication of rock properties and shapes. These steps include (i) the mixing of sand powder with an acid catalyst, (ii) the alternating deposition of sand and binding material on the print bed, and (iii) the curing of the resulting parts inside an oven. The binding material can be thought of as the artificial cementation between the sand grains. A critical prerequisite for the effective crystallization of the binding liquid is the pre-mixing of the sand powder with the acid catalyst [1]. In this study, ExOne's FA001 activator, primarily consisting of P-toluenesulfonic acid, was employed as the catalyst. The meticulous blending of 1.4 grams of acid catalyst with every 1000 grams of silica sand ensures the homogeneous dispersion of acid throughout the sand powder [1].

The deposition of sand powder was executed in layers using a vibrating hopper named recoater. each layer was approximately 250 micrometers in height. The particle size distribution of the silica sand indicated D10, D50, and D90 values of 110, 175, and 220 micrometers, respectively [1].

The binder liquid was dispensed onto the powder bed through the print head, equipped with 4x256 piezoelectric nozzles that generated a directed cloud of microdroplets maintained at a constant printing speed of 200 mm/s and a fixed height of 6 mm above the powder bed. These droplets, containing the binding material, were closely spaced in parallel lines, with a spacing of 64 micrometers in the x-direction and 138 micrometers in the y-direction. The properties of the binder, including its surface tension and composition, promoted the formation of connecting bridges at the sand grain contacts, ensuring nearly uniform infiltration of the sand pack. In this study, the binding liquid, ExOne FB001, was primarily composed of furfuryl alcohol with trace amounts of bisphenol A, resorcinol, and 3-aminopropyltriethoxysilane [1]. After each layer has the desired pattern with the shape of the designed sample, a roller compacts the sand to create denser samples [2] and the recoater adds the next layer of clean loose sand. Subsequent to the 3D printing process, the fabricated samples were subjected to curing at 80°C for at least 12 hours to eliminate any moisture. During all this process, variables as the amount of binder and thickness of each clean sand layer can be set up. The main components of the process are shown in Fig 5-1-a. The final material which is a combination of silica grains, pore space and binder is shown in Fig 5-1-b , this image was obtained using an optical microscope Zeizz-Axio Scope A1

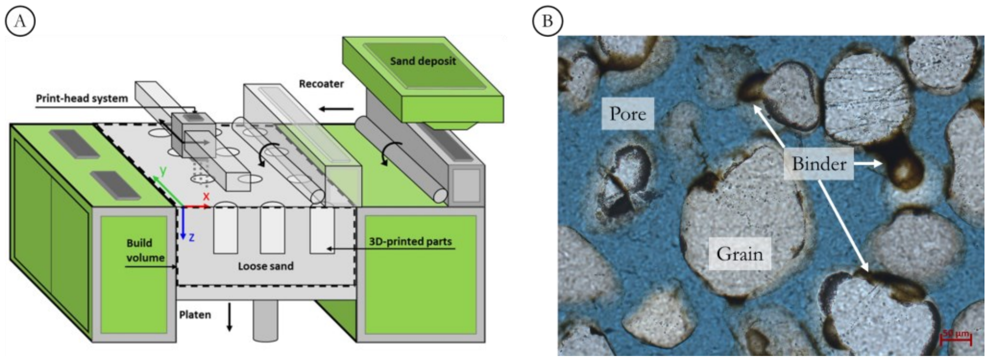

Fig 5-1.(a) Diagram with the main parts of the 3D printer of rocks. Taken from [3], **(b)** Thin-section images of cylindrical samples. Blue epoxy fills in the pore space. Silica grains are gray in color; dark brown binder forms necks between grains

Most of the current 3D printed samples are fabricated at 20% of binder saturation; this means that 20% of the porous volume is occupied by the binder (the artificial cement). This study explores the challenges of printing at low binder saturation (i.e. 5%). The 3D printed samples with such low level of binder saturation are characterized mechanically and hydraulically to establish their potential as rock analogs for poorly cemented reservoirs; e.g. Unconsolidated and semiconsolidated sand and gravel aquifers [4], heavy oil reservoirs [5], among other. .

5.3. **3D Printing Challenges at Low Binder Saturation.**

Typically, 3D printed specimens are fabricated with a binder saturation level of 20% and a layer thickness of 250 µm, which translates to well-consolidated rock formations [3]. In a related study, a comprehensive series of tests to characterize 3D printed rock samples with 20% binder saturation were conducted [6]. Those experiments revealed an unconfined compressive strength of 20,78 MPa, a Young's modulus of 1,79 GPa, and a Poisson ratio of 0.24. Those experiments strictly adhered to a meticulously defined standard operating procedure (SOP) for the printing process to ensure the reproducibility of the 3D printed rock specimens.

Adhering to the same SOP, a set of samples was fabricated with standard dimensions of 1.5 inches by 3 inches (1:2 ratio between diameter and height), but with a reduced binder saturation (from the typical

20% to 5%); this was intended to diminish the rock strength to mimic a poorly cemented heavy oil reservoir. During the printing process, certain cracks on the surface of the sand layers were observed, indicating the occurrence of a sliding effect during printing. For visual reference, Fig 5-2 provides a snapshot captured during the printing procedure.

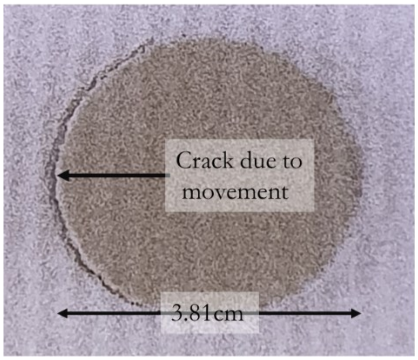

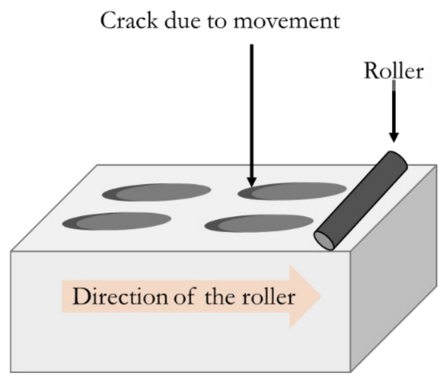

Fig 5-2. Cracks during printing at 5% binder with roller on (Left). Diagram of the issue (Right)

This printing issue arises from the interaction of the roller during the consolidation of the sand layers, primarily since the weight of each wet layer is less than the drag force. This reduced weight is caused by very low binder saturation.

Upon the completion of the printed samples at low binder saturation, a noticeable deviation was observed (Fig 5-3-left). This deviation occurs at the lower section of the sample, and it is larger close to the base of the sample, as shown in Fig 3-left using different angles of inclination versus horizontal direction. The magnitude of these angles signifies that at the initial stages of printing, the first bottom layers were subject to unintended horizontal displacement at the 3D printer bed. In order to rectify this issue, it is imperative to achieve equilibrium in the forces between the weight of the printed layers and the drag force exerted by the roller. Consequently, the primary solution entails the deactivation of the roller during the printing process.

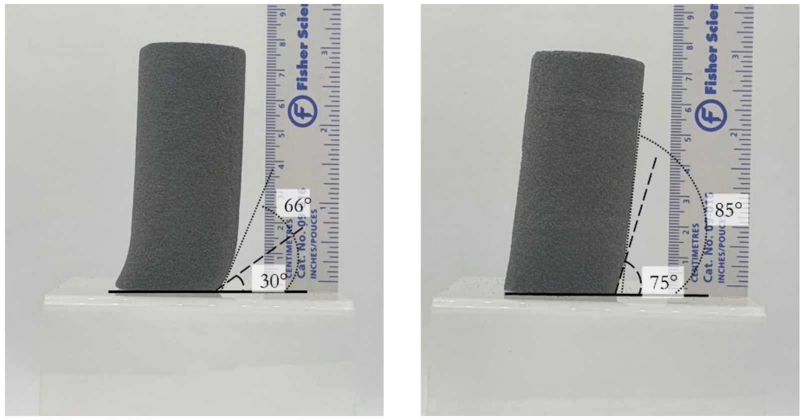

Fig 5-3. Sample printed at 5% binder saturation, 250 µm, and active roller (Left). Sample printed at 5% binder saturation, 250 µm, and no roller (Right)

5.3.1. **Printing with a Disabled Roller**

The deactivation of the roller diminishes the drag force between the roller and each printed layer; this allows the weight of the layers to potentially balance, and results in the fabrication of a straight, uniform sample. It is worth to mention that the roller function is primarily aimed to increase the density of 3D printed sample through compaction, aligning with the principles proposed in [2]. In the case of disabling the roller, other parameters, such as layer thickness and binder saturation, remained unaltered. Fig 5-3-right illustrates the shape of the printed samples with a disabled roller.

Upon disabling the roller, the samples still exhibit a noticeable deviation, but to a lesser degree (Fig 5-3-right), characterized by an initial inclination of 75°, followed by a nearly vertical orientation at 85°. A close inspection of the sample during the printing process indicated that, even when the roller is not in active rotation (indicating no rotation during the operation of the recoater), there is still contact between the sand layer and the roller. This sand layer-roller contact generates a significant level of friction, which becomes sufficiently large to displace the initial bottom layers of the 3D printed sample when the bulk volume of the printed sample is not substantial to overcome the frictional forces.

In order to restore equilibrium between the dragging forces and the weight of the wet layers, the second parameter that can be adjusted in the printing process is the weight of the 3D printed layer itself. This can be achieved by increasing the thickness of each layer.

5.3.2. **Printing with a Disabled Roller and thicker layers**

Increasing the thickness of each layer translates to a heavier and larger printed volume for each layer. For a binder saturation of 5%, the printed volume within each layer becomes more substantial when the layer thickness is set at 400 µm, compared to the standard 250 µm. As shown in Fig 5-4, this adjustment leads to the fabrication of high-quality straight and uniform cylindrical samples with no sign of deviation in the bottom printed layers. The shape of the printed sample clearly illustrates that thicker layers effectively counteract the frictional force exerted by the roller. By implementing the two modification into printing process, a total of 22 samples (Which are statistically identical [1]) were successfully fabricated for subsequent mechanical and petrophysical characterization.

Fig 5-4. Sample printed at 5% binders, 400 μm, and no roller

Additional challenges were found in the printing process due to hardware issues, those are described in the appendix e.

5.4. **Mechanical Behavior**

5.4.1. **Uniaxial Compressive Strength Tests**

The Uniaxial Compressive Strength is defined as the compressive stress at which an unconfined cylindrical soil specimen will fail in a simple compression test. In this method, unconfined compressive strength is determined as the maximum load achieved per unit area, as per ASTM guidelines [7]. To conduct this test, a two column load frame with a maximum capacity of 50 kN of axial load was employed. The sensing experimental setup consists of a loading cell positioned at the top of the sample (max. capacity of 15000 lbs), a Linear Variable Differential Transformer (LVDT) to measure vertical displacement with an independent linearity of $\leq \pm 0.2$ %FS, and a circumferential LVDT (Fig 5-5-a). After calibrating the sensors (i.e. the loading cell, and both LVDT's), the 3D printed rock sample was positioned inside the load frame, subjected to a vertical axial load at a strain rate of 0.12 mm/min.

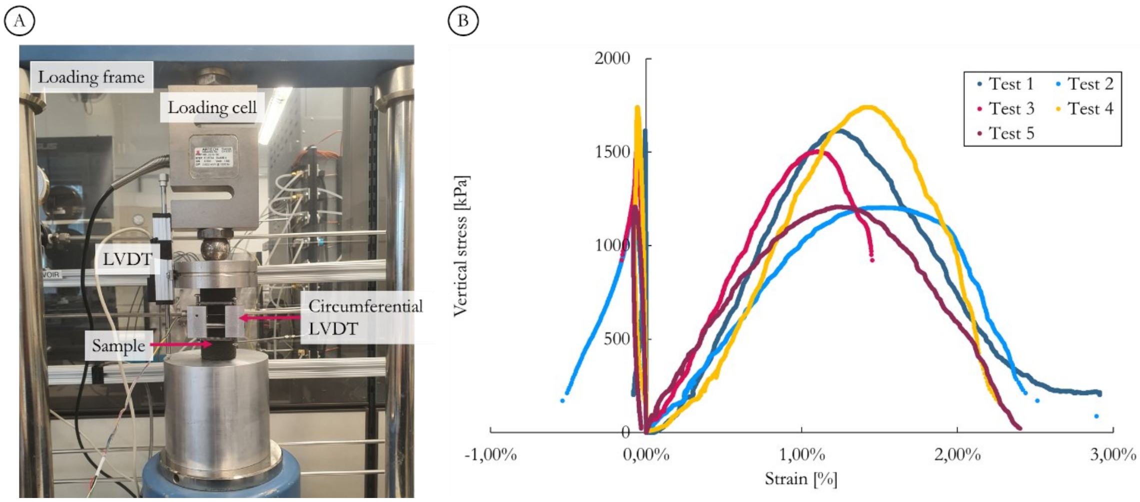

Fig 5-5. a) UCS setup and b) Stress-Strain curve for samples at 5% binder saturation.

The USC tests were conducted using five identical 3D printed rock samples to assure the test repeatability. The results are presented in Fig 5-5-b. In terms of mechanical behavior, the radial strain exhibits a pronounced strain-stress relationship, characterized by a steep response in Fig 5-5-b. This observation could be attributed to various factors, including the pore collapse due to low degree of cementation (i.e. low binder saturation between sand grains) being the most probable cause. It is worth to mention that despite the difference in peak values, all specimens display a consistent behavior, underscoring the test repeatability using 3D printed rocks. Following the initial elastic response, the samples display a strain softening behavior, which is akin to responses observed in certain Canadian heavy oil reservoirs, such as the one described by McMurray [8]. Table 5-1 is a summary of results obtained from the UCS tests, including the Young's modulus that was calculated as the tangential at 50% of peak.

Table 5-1. Summary of UCS tests

	Sample 1	**Sample 2**	**Sample 3**	**Sample 4**	**Sample 5**	**Average**	**St Dev.**
Diameter [mm]	38,18	38,19	38,03	37,87	37,65	37,98	0,20
Length [mm]	75,85	75,62	75,89	75,82	75,69	75,77	0,10
UCS [MPa]	1,65	1,20	1,50	1,74	1,21	1,45	0,21
Young Modulus [MPa]	180,14	110,24	239,07	251,81	94,67	175,18	64,31
Axial strain at peak	1,24%	1,51%	1,10%	1,42%	1,25%	1,30%	0,14%
Poisson Ration	0,0004	0,03	0,04	0,02	0,05	0,03	0,02

Our experimental results indicate that the utilization of 3D printing technology yields rock samples with consistent shapes and uniform structures, characterized by minimal deviations in their diameters and lengths. This not only enhances the quality of the results but also facilitates more reliable comparisons with samples with the presence of heterogeneities. For the low binder saturation of 5% in the printing process, an average UCS of 1,45 MPa with a low standard deviation was obtained. However, the behavior of the Young's Modulus exhibited some variability between 94,67 MPa and 251,81 MPa. The low Poisson ratio is likely caused due to the samples undergoing pore collapse prior to radial expansion. In such circumstances, the initial axial loading of the sample leads to the pore collapse rather than radial strain; this can also explain the potential large standard deviation in the Young's modulus.

In comparison to the UCS values reported for 3D printed rocks of different degrees of binder saturation ([6], [9]), our experimental results shows a consistent trend with prior research (Fig 5-6-a); this improves the confidence of relating UCS to binder saturation. Assuming a linear regression analysis, the minimum binder saturation would be approximately 3% during the 3D printing process. It is important to mention that the work by [6] used a layer thickness of 250 µm.

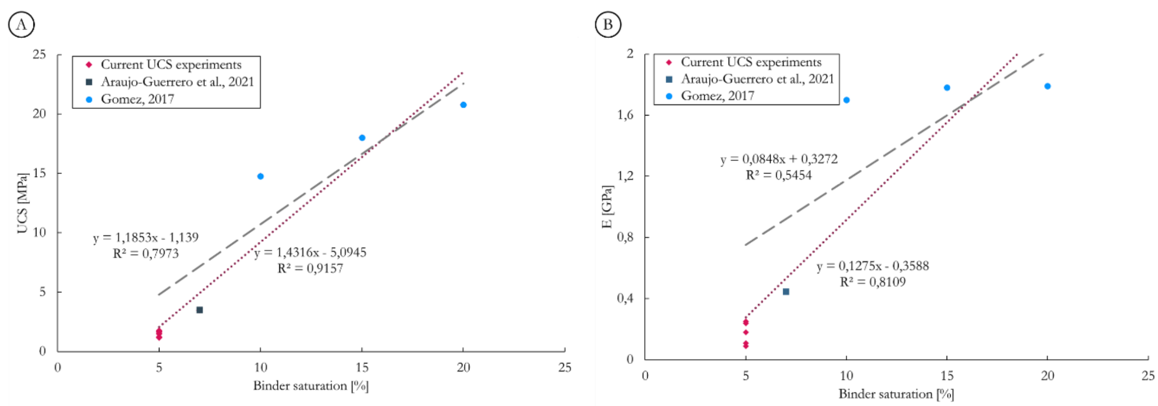

Fig 5-6. a) UCS of multiple samples with different binder saturation degrees. b) Young's modulus of multiple samples with different binder saturation degrees

The 3D printed rocks appear to show similar mechanical behavior to some core samples extracted from actual heavy oil reservoirs (Fig 5-7); especially, the relationship between Young modulus and UCS for 3D printed rocks with 5% binder saturation align well with Canadian heavy oil formations such as McMurray and Cold Lake. This increases our confidence in using the 3D printed samples with 5% binder saturation for mechanical testing when accessing to actual cores from these reservoirs is limited.

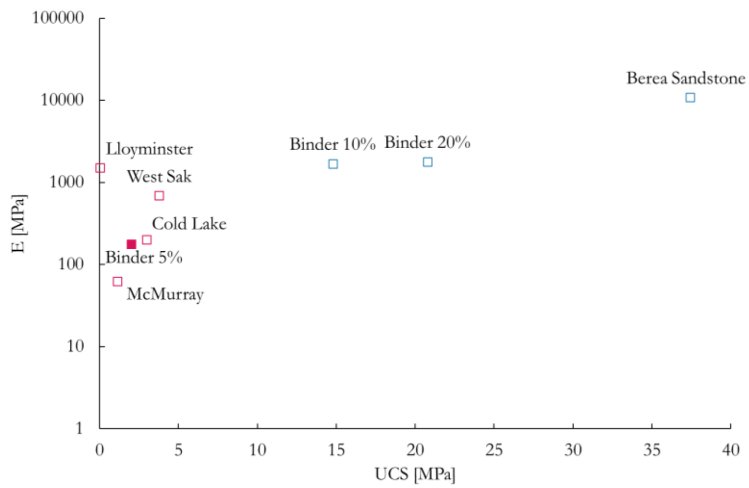

Fig 5-7. Elastic behavior compared with some reservoirs. Pink squares represent heavy oil reservoirs. The filled pink square is the 5% binder saturation sample. Blue squares are other materials for reference.

Regarding the failure mode, all the samples subjected to UCS tests exhibit a consistent failure mechanism, characterized by a persistent diagonal crack (Fig 5-8). This typical failure mode in a 2:1 ratio cylindrical rock sample provides valuable insight into the mechanical behavior of rock under stress. The rock undergoing a UCS test often either shows a diagonal fracture (associated with shearing), or a vertical fracture (resulting from tensile failure) regardless of the orientation of sedimentation or layering in 3D printed samples, as demonstrated by [10].

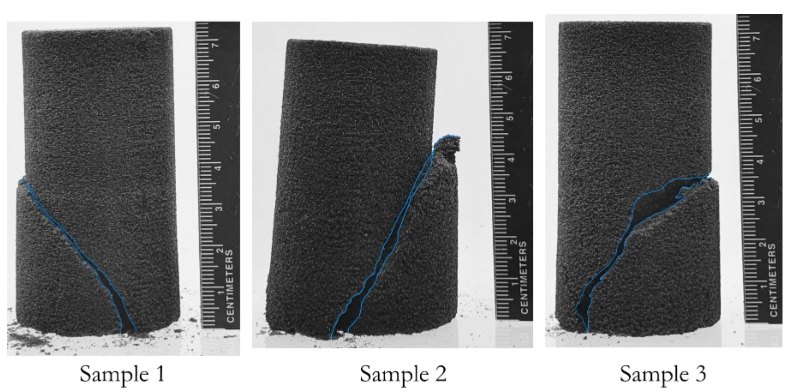

Fig 5-8. Failure mechanics in three different samples under UCS test. Blue lines added to highlight the failure planes edges.

For certain engineering applications (e.g. soil remediation after contamination), the potential change in the UCS, caused by prolonged saturation with a fluid (e.g. oil), is important [11]. To examine this effect, some 3D printed rock samples were saturated with canola oil for a soaking time of 109 and 214 days, respectively. Following the saturation period, the fluid in the 3D printed rocks was allowed to drain by gravity over the course of a week, with absorbent paper changes performed regularly. This process was particularly effective due to the high permeability of the sample. Subsequently, the samples underwent UCS testing, and the results are depicted in Fig 5-9. The indication of the slope corresponds to a Young's modulus of 175 MPa that was found for the intact samples is added to the graph as a reference.

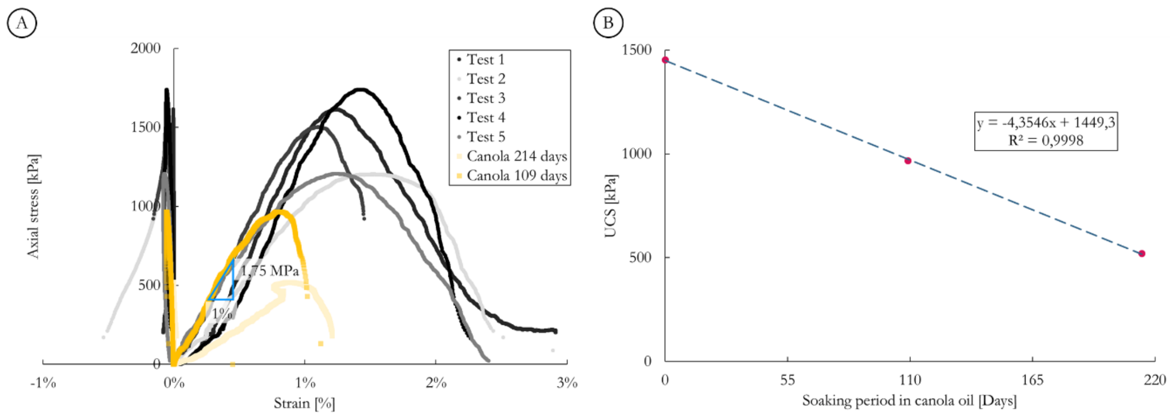

Fig 5-9. a) Stress-strain relationship for samples soaking in canola oil, and b) Change of the UCS with long oil saturation. And

The results indicated a significant 64% decrease in UCS, declining from 1,45 MPa to 0,52 MPa after the soaking using canola oil for 214 days. This reduction to more than a half of the strength value for intact samples suggests a weakening of the binder material as the one described by [12] who measured changes in strength for samples printed at 20% of binder saturation and soaked into water or silicone oil for period between 15 minute to two weeks. Those experiments allowed the author to conclude that for specimens submerged in water, the UCS peak strength decreased by an average of 42% compared to the unsaturated case (base case), while for those submerged in silicone oil, the decrease was only around 5% [12].

If the calculation for the reduction of strength due to canola oil is done for 2 weeks (14 days) using the linear regression shown in Figure 10-b, a decrease of 4.2% is found. This decrease closely aligns with the 5% found by Ardila Angulo for silicone oil. It indicates that saturation with oils does not significantly impact the strength of the samples in the short term. However, prolonged soaking periods, such as 214 days, do result in noticeable effects on strength. The UCS weakening of 3D printed rocks subject to different fluids and saturation time periods needs further investigation.

5.4.2. **Triaxial Tests**

In order to gain a comprehensive understanding of the yielding and failure mechanisms of the material, a series of triaxial consolidated-drained tests were conducted under isothermal conditions. The triaxial test setup, as depicted in Fig 5-10, included axial and radial LVDTs to measure the displacement of the sample when it is within the cell during the experiment. Additionally, external linear displacement sensors are employed to track the displacement of the loading ram throughout the test. It is essential to highlight that all the instrumentations employed in the triaxial tests were calibrated prior to their use.

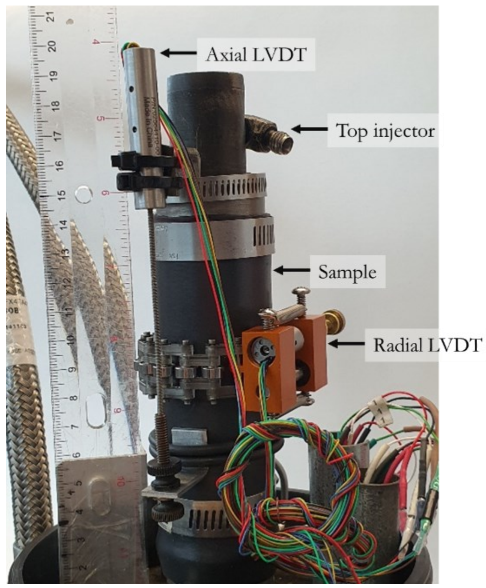

Fig 5-10. General setup for triaxial tests.

Throughout the test, canola oil serves as both the pore and confining pressure fluid, with the pore pressure being meticulously regulated using a high-precision Quizix pump model QX-500 with a resolution in the flow rate of 0,1 mL/min. An initial consolidation phase was conducted at 2000 kPa, maintaining an effective stress of 500 kPa, until the shearing phase was initiated. The resultant failure envelope is illustrated in Fig 5-11. By assuming the Mohr-Coulomb theory of failure, the analysis reveals a cohesion value of 350 kPa and an internal friction angle of 56°, providing key insights into the material's behavior under the selected test conditions. In comparison to other triaxial tests conducted on 3D printed samples (e.g. [9], [13]) it is evident that the samples with a 5% binder saturation exhibit a lower cohesion, which is expected due to the lower binder content. However, what stands out is that these samples show a higher internal friction angle, a characteristic compatible with the results typically found in very dense sands [14].

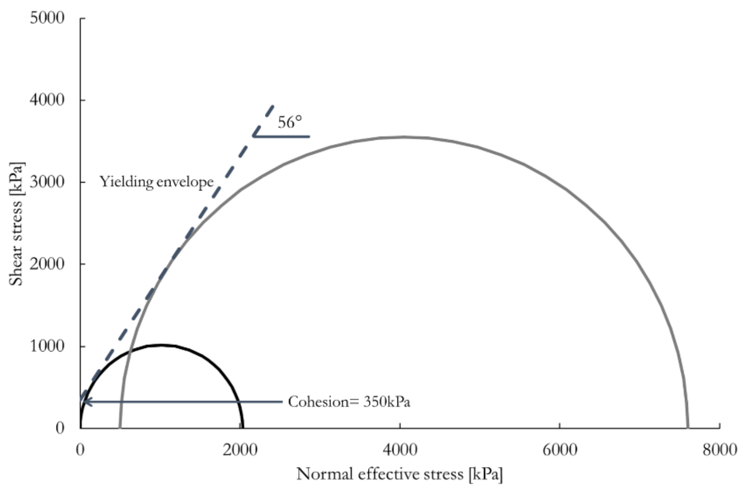

Fig 5-11. Yielding envelope

This observation is important as it indicates that a substantial portion of the material's strength is derived from the frictional interaction between the grains, rather than the cementation (binder) between the grains; this aligns with the nature of the 3D printed rock samples.

5.4.3. **Creep Tests**

The study of creep behavior provides valuable insights into how rocks respond to long-term loading conditions [15]. In this context, a series of isotropic creep tests were conducted at an effective hydrostatic stress of 90 kPa using the same setup that was employed for the triaxial tests. Fig 5-12 illustrates the axial strain (blue circles), rate of strain (red squares), and moving average values of the strain rate (red triangles) for Test A, encompassing primary creep and part of the secondary creep phase. In Test B, due to technical challenges, the primary creep phase was not recorded; however, the secondary creep phase was observed for a duration of over 500 minutes. Test B illustrates how the secondary creep phase aligns with the expected theoretical behavior, as discussed by [15], which forecasts a constant deformation and zero deformation rate. During this phase, the strain rates are in the order of 1×10^{-6} strain/min, indicating the stability of the 3D printed rock response.

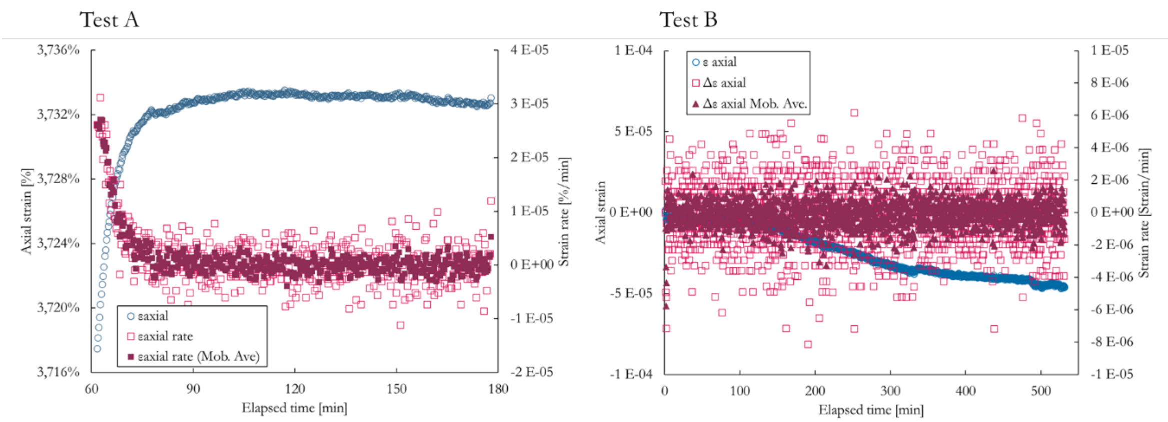

Fig 5-12. Creep response of the samples in the test A and B

The observed creep behavior for 3D printed rock samples with low binder saturation is interesting from an experimental perspective, as it suggests that the results from tests that require long periods of effective stress stabilization (e.g. the consolidation phase of triaxial tests), remain almost unaffected by creep behavior, particularly within the initial 500 minutes (Test B).

5.4.4. **Failure Mode**

A comparison of the failure mechanism of the 3D printed rocks at 5% binder saturation was conducted given the final state under various conditions, namely confining stress, and binder saturation. The results are depicted in Fig 5-13, which illustrates the failure behavior across different confining stresses and binder saturations. The comparative assessment explains how the 3D printed rock responds to varying stress conditions, shedding light on its mechanical behavior.

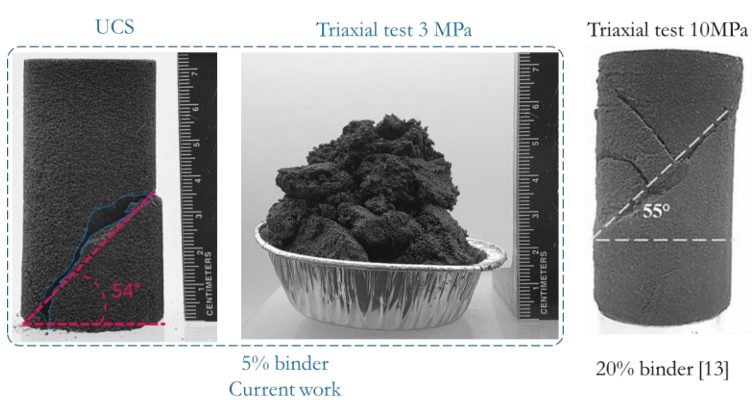

Fig 5-13. Failure mode for unconfined conditions at 5% binder saturation (Left), triaxial test at 5% binder saturation (center), and triaxial test at 20% binder saturation (Right)

Following the triaxial tests, it becomes evident that large deformations and dilation result in a loss of the sample structural integrity, causing it to transition from a cylindrical shape to a state resembling loose sand with minimal cohesion. This behavior diverges from the observations described by [13] in the case of triaxial tests conducted on 3D printed samples with higher binder saturation. In those samples, a distinct shearing diagonal failure plane was identified and characterized as having an inclination of 55° relative to the horizontal. In contrast, for the material with 5% binder saturation, a similar failure mechanism is observed, particularly under unconfined conditions, where sample 3 exhibits a failure plane inclined at 54°.

This variance in behavior raises questions about the distribution of the binder within the layers, especially considering the use of thicker layers (400 μm) for printing at 5% binder saturation. To investigate this matter, a computed tomography (CT) scan is conducted with a voxel size of 1,5 μm x 1,5 μm x 1,5 μm on an intact sample to assess the distribution of the binder within the layers. Fig 5-14 is a snapshot of the results in different directions that shows the distribution of the binder material within the printed layers. The top images show the result of two vertical slices (532 and 1494 out of 1914) of the scanned sample. Meanwhile, the bottom ones correspond to horizontal slices.

In Fig 5-14, the blue regions represent the silica grains, while the yellow areas correspond to the binders. In the case of the horizontal slices, there is a circular hole in the middle that was caused after placing a piece of wood to improve the density contrast and obtain a better scan. It is apparent that there are regions where the binder effectively attaches the grains together. However, the overall observation is that the binder is reasonably well-distributed within the 3D printed rock. Consequently, it can be inferred that the behavior of the analogue rock is not primarily attributed to the lack of binder within the layers, but it rather stems from its inherent response to shearing stress, it is the relationship between the grains and the binder attaching them together in a given structure.

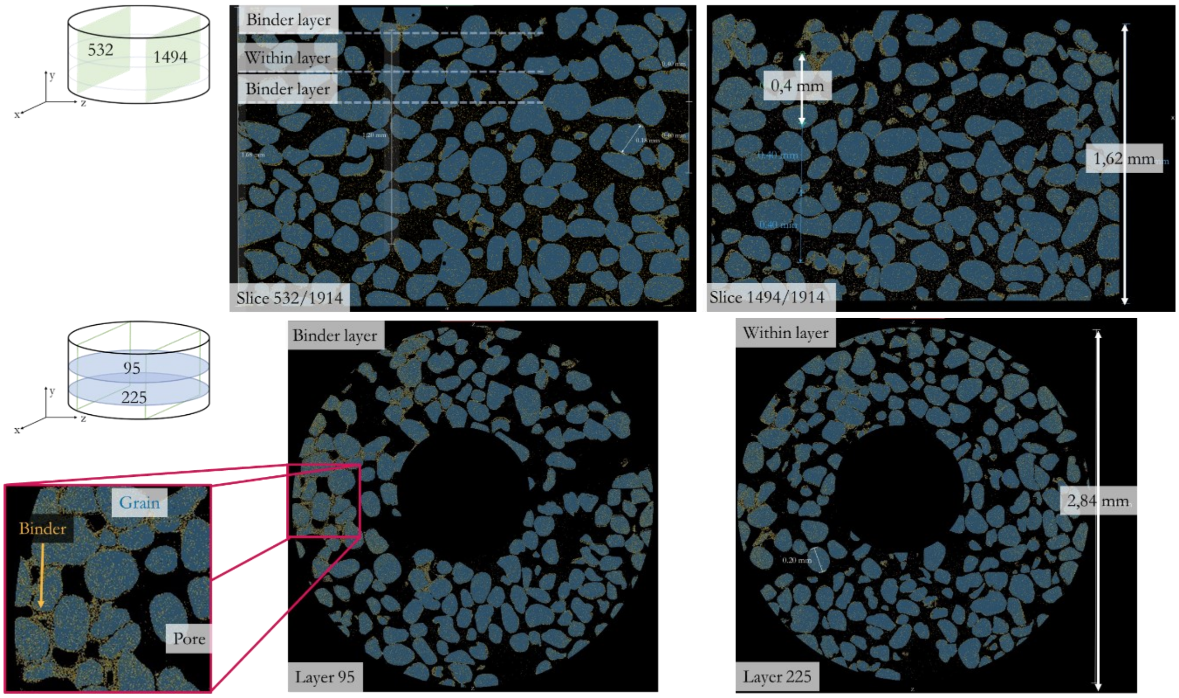

Fig 5-14. CT scan of analogous at 5% binder saturation planar and axial views. Top views are axial views at different slices. Bottom views are planar views at different slices. Binder material illustrated with the yellow voxels

The thin-section technique allowed for the observation of binder distribution, as depicted in the results shown in Fig 5-15-a. An optic microscope Zeizz Axio Scope A1 was used to capture the snapshots of the thin section. A comparative analysis reveals that samples printed with 5% binder saturation exhibit significantly fewer binder necks between grains compared to those printed at 20% and 10% (Fig 5-15-b), as reported in [16].

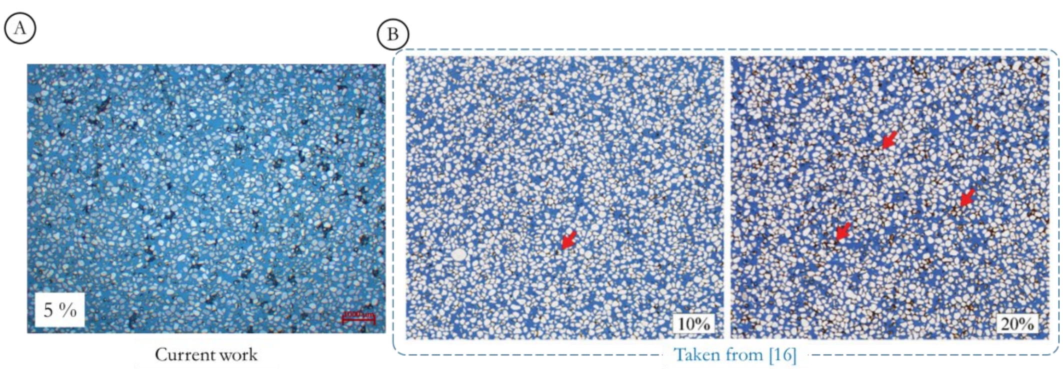

Fig 5-15. Thin-section images of cylindrical samples. Binder saturation is indicated on each photograph. Blue epoxy fills in the pore space. Silica grains are gray in color; dark brown binder forms necks between grains (red arrows in B). The black dots in (A) are bubbles of air that got trapped in the epoxy

5.4.5. **Skempton Parameter "B"**

The changes in porewater pressure within soils are influenced by fluctuations in both the mean total and deviatoric stresses. In axisymmetric conditions, Skempton introduced the following equation for the calculation of pore water pressure [17]:

$$\Delta u = B[\Delta\sigma_3 + A(\Delta\sigma_1 - \Delta\sigma_3)] \tag{5-1}$$

Where u is pore pressure, $\Delta\sigma_i$ is the stress change in i direction, A and B are known as Skempton pore pressure coefficients. During consolidation, there is no deviatoric stress ($\Delta\sigma_1 - \Delta\sigma_3 = 0$), thus Eq. (5-1) can be written as follows:

$$\Delta u = B\Delta\sigma_3 \tag{5-2}$$

$$\therefore B = \frac{\Delta u}{\Delta\sigma_3}$$

Therefore, during the consolidation phase, the parameter B offers insights into how pore pressure increases in response to a change in confining stress. Fig 5-16 based on triaxial testing of 3D printed samples illustrates the variations in pore pressure as the confining stress increases.

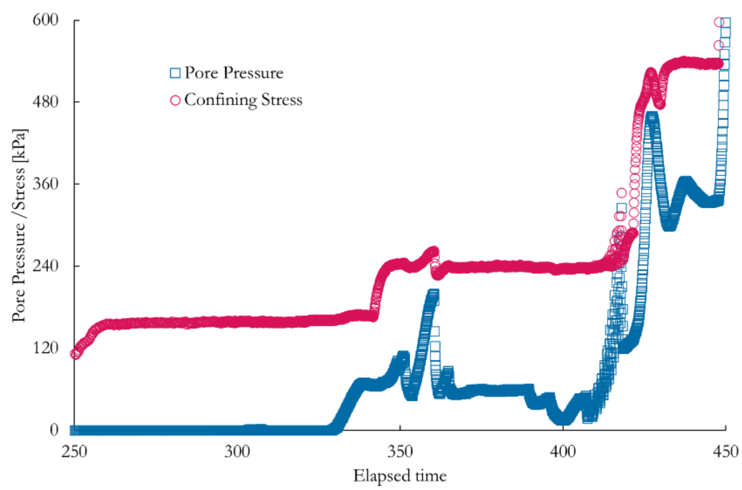

Fig 5-16. Response of pore pressure with changes in confining stress.

By utilizing the data collected during the period when the confining and pore pressure remain stable, the calculation of Skempton's parameter B yields a value of 0,73. This value aligns with the expected result for a fully saturated 3D printed rock with poor cementation. It is worth noting that the use of canola oil for this measurement may introduce some compressibility effects that could influence the result.

5.5. **Hydraulic Description**

5.5.1. **Porosity**

The determination of porosity involved saturating the sample with both water or canola oil. The saturated sample was then placed in a vacuum chamber, where daily measurements of its weight were recorded until a stable value was achieved. Each porosity measurement was conducted over three consecutive days; the results are summarized in Table 5-2.

Table 5-2. Summary of the porosity measurements

Sample	Density [g/cc]	Porosity [%]	Saturation
Sample1	1,41	44,4%	Water
Sample 2	1,43	44,9%	Water
Sample 3	1,42	47,1%	Oil
Sample 4	1,42	47,5%	Oil
Average	1,42	46%	N/A
St. Dev.	0,01	1,3%	N/A

The results from porosity measurements indicate that the 3D printed rock at 5% binder saturation is characterized by a high degree of porosity. Additionally, the samples exhibit a high degree of statistical homogeneity, with minimal variation in their porosities. This conclusion aligns with similar findings reported by [1], further supporting the consistency and uniformity of the 3D printed samples.

5.5.2. **Permeability**

The permeability measurement was carried out using the steady-state technique [18] where a drawdown pressure is applied to the sample, and the flowrate is observed until it stabilizes over a certain period as shown in Fig 5-17. This test was carried out in a sample placed vertically, due to the short size of the sample (7,62 cm), the gravitation effect may be disregarded.

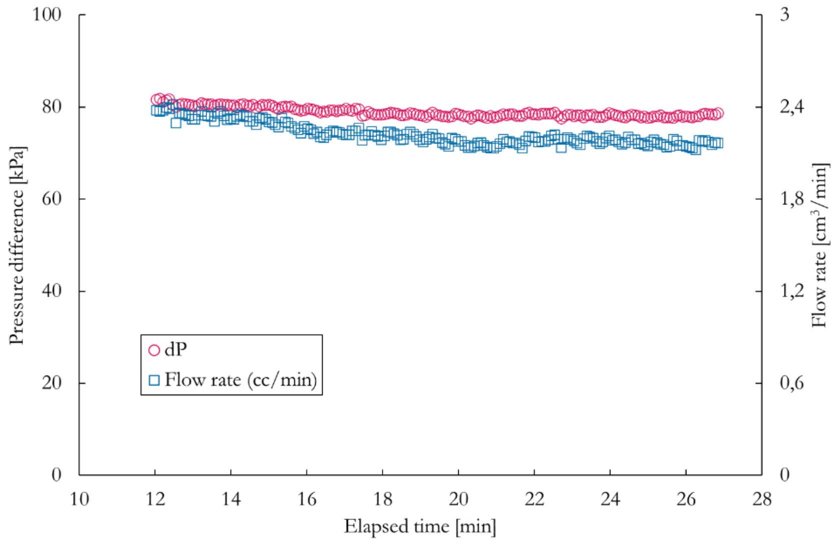

Fig 5-17. Pressure difference between top and bottom, and flow rate.

The pressure difference between the bottom and top of the sample recorded with two pressure transduces exhibited a deviation of 1,32%, while the flow rate showed a deviation of 3,16%. These observations indicate that the flow was predominantly laminar and very close to steady-state conditions, validating the applicability of Darcy's equation. In this context, the effects of gravity can be considered negligible, given the small size of the sample (76,2 mm).

By employing a viscosity value of 93,99 cP for canola oil [19], an absolute permeability value of 1,77 Darcies was determined. Fig 5-18 shows the permeability and porosity of the 3D printed rock samples in comparison with actual cores from some heavy oil reservoirs; the measured permeabilities of 3D printed rocks fall within the permeability range for the heavy oil reservoirs.

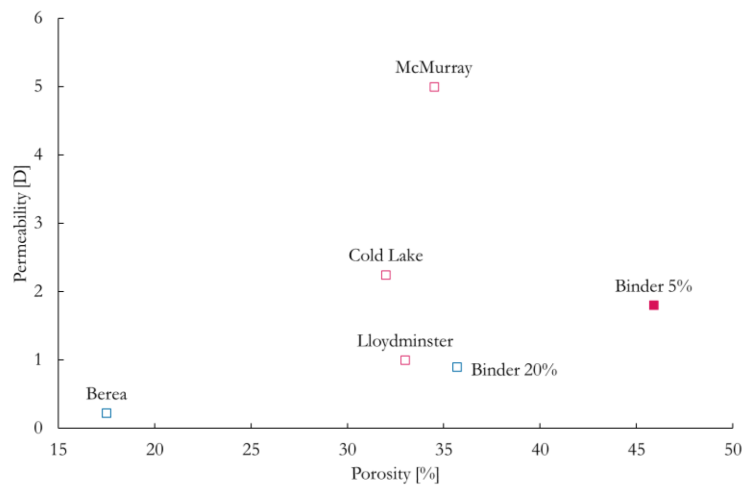

Fig 5-18. Petrophysical characteristics of 5% binder saturation samples (Pink filled square) compared with some heavy oil reservoirs (pink squares) and reference rocks (blue squares). Some of the reservoir values are the mean from the observe range in the reservoir.

5.6. **Conclusions**

The conclusions drawn from the current study are as follows:

1. Printing samples at low binder saturation with thicker layers of 400 µm effectively resolved issues related to dragging forces and led to well-shaped samples.

2. Samples printed at 5% binder saturation exhibit behavior similar to certain heavy oil reservoirs within the elastic domain. This suggests that the material described in this study can be used as analogs for core samples from heavy oil reservoirs for further experimental study.

3. The measured petrophysical properties of the 3D printed rock samples, including average porosity of 46% and permeability of 1,77 Darcies, align well with those of typical heavy oil reservoirs. The Young's modulus and UCS were determined to be 175,2 MPa and 1,45 MPa, respectively.

4. The primary failure mechanism observed under triaxial conditions for 3D printed rock samples with 5% binder saturation appears to be pore collapse, leading to the loss of rock integrity. This failure mode differs from what was observed in the UCS and triaxial tests conducted on 3D printed rocks with higher binder saturation of 20%.

5. CT scans revealed that the binder was evenly distributed within the layers which represents a homogeneous medium.

6. The results of the triaxial test yielded a cohesion of 350 kPa and an internal friction angle of 56°. The isotropic creep test demonstrated a typical creep response to consolidation stresses.

7. These experimental findings provide valuable insights into the behavior of the 3D printed rocks at low binder saturation and their potential applications for further experimental studies as analogs to heavy oil reservoir rocks or poorly cemented water reservoirs.

8. The experimental results indicated the weakening of the binder material (47% decrease in UCS) with long-term soaking using canola oil. The UCS weakening of 3D printed rocks subject to different fluids and soaking periods needs further investigation.

5.7. **Acknowledgements**

This work was partially supported by Mitacs through the Mitacs Accelerate program. We gratefully acknowledge the Heavy Oil Research Network program, managed by the Petroleum Technology Research Centre, Regina for providing partial funding of this research project. We gratefully acknowledge the NSERC/Energi Simulation Industrial Research Chair in Reservoir Geomechanics in Unconventional Resources for additional funding.

We also would like to acknowledge the scanning work carried out at the nanoFAB facility of the University of Alberta. And Dr. Noga Vaisblat for her help with the acquisition of the thin section images.

5.8. **References**

[1] B. Primkulov, J. Chalaturnyk, R. Chalaturnyk, and G. Zambrano Narvaez, "3D printed sandstone strength: Curing of furfuryl alcohol resin-based sandstones," *3D Printing and Additive Manufacturing*, vol. 4, no. 3, pp. 149–155, 2017.

[2] K. J. Hodder, A. J. Sanchez-Barra, S. Ishutov, G. Zambrano-Narvaez, and R. J. Chalaturnyk, "Increasing Density of 3D-Printed Sandstone through Compaction," *Energies*, vol. 15, no. 5, 2022.

[3] A. Sanchez-Barra, G. Zambrano-Narvaez, and R. Chalaturnyk, "An In-Depth Analysis of Strength and Stiffness Variability in 3D-Printed Sandstones: Implications for Geomechanics," *Energies*, vol. 16, no. 14, p. 5406, Jul. 2023.

[4] Water Resources Mission Area, "Unconsolidated and semiconsolidated sand and gravel aquifers," 2021. [Online]. Available: https://www.usgs.gov/mission-areas/water-resources/science/unconsolidated-and-semiconsolidated-sand-and-gravel-aquifers. [Accessed: 17-Feb-2024].

[5] D. Cartagena Perez *et al.*, "Scaled Physical Modeling of Cyclic CO2 Injection in Unconsolidated

Heavy Oil Reservoirs Using Geotechnical Centrifuge and Additive Manufacturing Technologies," in *SPE Canadian Energy Technology Conference and Exhibition*, 2024.

[6] J. S. Gomez, "Mechanical Properties Characterization of Printed Reservoir Sandstone Analogues," 2017.

[7] ASTM, "Standard Test Method for Unconfined Compressive Strength of Cohesive Soil 1," *ASTM International*, no. January. 2013.

[8] P. Li and R. J. Chalaturnyk, "Geomechanical Model of Oil Sands," in *SPE International Thermal Operations and Heavy Oil Symposium*, 2005.

[9] E. F. Araujo-Guerrero, G. A. Alzate-Espinosa, J. G. Osorio, R. Chalaturnyk, and G. Zambrano, "Advanced geomechanically laboratory testing for sand production with aids of 3D printing technology," *55th U.S. Rock Mechanics / Geomechanics Symposium 2021*, vol. 4, 2021.

[10] J. Chang, J. Ivory, and G. Beaulieu, "Pressure maintenance at post-CHOPS cyclic solvent injection (CSI) well using gas injection at offset well," in *SPE Heavy Oil Conference*, 2014, vol. 2, pp. 1387–1409.

[11] A. Salimnezhad, H. Soltani-Jigheh, and A. A. Soorki, "Effects of oil contamination and bioremediation on geotechnical properties of highly plastic clayey soil," *Journal of Rock Mechanics and Geotechnical Engineering*, vol. 13, no. 3, pp. 653–670, Jun. 2021.

[12] N. A. Ardila Angulo, "Hydraulic properties characterization of 3D printed sandstone analogues," University of Alberta, 2018.

[13] J. S. Gomez, R. J. Chalaturnyk, and G. Zambrano-Narvaez, "Experimental Investigation of the Mechanical Behavior and Permeability of 3D Printed Sandstone Analogues Under Triaxial Conditions," *Transport in Porous Media*, vol. 129, no. 2, pp. 541–557, 2019.

[14] B. Das and N. Sivakugan, *Fundamentals of geotechnical engineering*. Boston: Cengage Learning, 2017.

[15] W. Frenelus, H. Peng, and J. Zhang, "Creep Behavior of Rocks and Its Application to the Long-Term Stability of Deep Rock Tunnels," *Applied Sciences*, vol. 12, no. 17, p. 8451, Aug. 2022.

[16] K. J. Hodder, K. Craplewe, S. Ishutov, and R. Chalaturnyk, "Binder Saturation as a Controlling Factor for Porosity Variation in 3D-Printed Sandstone," *Petrophysics*, vol. 62, no. 5, pp. 450–462, 2021.

[17] M. Budhu, *Soil mechanics and foundations*, 3rd ed. John Wiley & Sons, 2010.

[18] ASTM, "Standard Test Method for Permeability of Granular Soils (Constant Head)." 2000.

[19] E. E. G. Rojas, J. S. R. Coimbra, and J. Telis-Romero, "Thermophysical Properties of Cotton, Canola, Sunflower and Soybean Oils as a Function of Temperature," *International Journal of Food Properties*, vol. 16, no. 7, pp. 1620–1629, Oct. 2013.

Chapter 6

Conclusions and Recommendations

In this section, an overall view of the study is presented, with key conclusions and insights highlighted:

1. The implementation of CO_2-CSI in fields of Western Canada has been relative successful and even adopted after cycles done with other solvents in post-CHOPS reservoirs. This shows the potential in real life of the technique.
2. A brand-new cell with triaxial capabilities and able to manage multiphase flow was designed, constructed, commissioned, and tested in this thesis. This cell, one of its kind in the world, may help engineers to model complex phenomena regarding flow in porous media.
3. The radial flow during the test was confirmed using well testing technique analysis. This means that the test was carried out in a more realistic flow regime that is barely available in physical modelling at a laboratory scale.
4. The physical modelling including wormholes as an initial condition revealed the influence of strength in the final production of sand. During our test, the production of sand was not significant even with the presence of wormholes that leads to higher drawdown pressure inside them.
5. It was possible to 3D print rocks at 5% binder saturation to emulate the behavior of poorly cemented reservoir. After mechanical tests, it is possible to conclude that the new material behaves as some main Albertan reservoirs in the elastic domain. The hydraulic characterization shows that the samples printed at 5% binder saturation have a permeability in the range of those CHOPS reservoirs but higher porosity.
6. The failure mechanism of the samples at 5% binder saturation is according with what expected for poorly cemented rock. It is marked by strong dilation and loose in the integrity of the rock.

References

To provide the reader with a comprehensive compilation of references in one place, while also facilitating comfortable reading of the papers and chapters that comprise this thesis, a list of references is presented here, organized by chapter.

Recent Developments of Cyclic Solvent Injection Process to Improve Oil Recovery From Unconsolidated Heavy Oil Reservoirs

[1] BP, “Statistical Review of World Energy,” 2020.

[2] Canada Energy Regulator, “Crude Oil Annual Export Summary – 2020,” 2021. [Online]. Available: https://www.cer-rec.gc.ca/en/data-analysis/energy-commodities/crude-oil-petroleum-products/statistics/crude-oil-summary/crude-oil-annual-export-summary.html. [Accessed: 26-Jul-2021].

[3] G. Coskuner, K. Naderi, and T. Babadagli, “An enhanced oil recovery technology as a follow up to cold heavy oil production with sand,” Journal of Petroleum Science and Engineering, vol. 133, pp. 475–482, 2015.

[4] D. W. Zhao, J. Wang, and I. D. Gates, “Thermal recovery strategies for thin heavy oil reservoirs,” Fuel, vol. 117, pp. 431–441, Jan. 2014.

[5] G. Coskuner and H. Huang, “Enhanced oil recovery in post-CHOPS cold heavy oil production with sand heavy oil reservoirs of Alberta and Saskatchewan part 2: Field piloting of cycling solvent injection,” Society of Petroleum Engineers - SPE Canada Heavy Oil Conference 2020, CHOC 2020, vol. 3, 2020.

[6] M. B. Dusseault, “CHOPS: Cold Heavy Oil Production with Sand in the Canadian heavy oil industry,” Waterloo, 2002.

[7] C. M. Istchenko and I. D. Gates, “Well/wormhole model of cold heavy-oil production with sand,” SPE Journal, vol. 19, no. 2, pp. 260–269, 2014.

[8] E. Fjær, R. M. Holt, P. Horsrud, A. M. Raaen, and R. Risnes, Petroleum Related Rock Mechanics. Elsevier, 2008.

[9] V. Fattahpour, M. Roostaei, M. Mahmoudi, M. Soroush, S. A. Hosseini, and M. Anderson, "Standalone sand control evaluation: Developing a large-scale high temperature sand retention test apparatus," in SPE Canada Heavy Oil Conference 2020, 2020.

[10] K. Naderi, N. Romaniuk, and B. Ozum, "Improvement of the CHOPS process efficiency," in SPE Kuwait Oil and Gas Show and Conference, 2015.

[11] M. Plata, J. Bryan, and A. Kantzas, "Experimental study of heavy oil recovery mechanisms during cyclic solvent injection processes," in Proceedings - SPE Annual Technical Conference and Exhibition, 2018, no. June, pp. 24–26.

[12] X. Li, X. Sun, Z. Yang, H. Gong, T. Li, and X. Shi, "Experimental study on chemical-assisted methane flooding for foamy oil reservoirs after primary production," Journal of Petroleum Science and Engineering, vol. 216, p. 110803, Sep. 2022.

[13] P. Luo, S. Li, K. D. Knorr, and P. Nakutnyy, "A New PVT Apparatus for Automatic Measurement of Foamy Oil Generation and Stability," in PE Canada Heavy Oil Technical Conference, CHOC 2018, 2018, vol. 2018-Janua.

[14] B. Maini, "Foamy Oil Flow in Primary Production of Heavy Oil under Solution Gas Drive," in Annual Technical Conference and Exhibition, 1999.

[15] C. Shen, M. L. Hamm, and M. Bdair, "Improving cold heavy oil development at peace river with the understanding of foamy-oil dynamics," in SPE Kuwait Oil and Gas Show and Conference, 2015.

[16] M. Wu, X. Lu, J. Yang, Z. Lin, and F. Zeng, "Experimental analysis of optimal viscosity for optimizing foamy oil behavior in the porous media," Fuel, vol. 262, p. 116602, Feb. 2020.

[17] H. Wang, F. Torabi, F. Zeng, and H. Xiao, "A novel visualization approach for foamy oil non-equilibrium phase behavior study of solvent / live heavy oil systems," vol. 272, no. March, 2020.

[18] Z. Du, F. Zeng, and C. Chan, "Effects of pressure decline rate on the post-CHOPS cyclic solvent injection process," in Society of Petroleum Engineers - SPE Heavy Oil Conference Canada 2014, 2014, vol. 3, pp. 1979–1996.

[19] T. Lu, Z. Li, W. Fan, and S. Li, "CO2 huff and puff for heavy oil recovery after primary production," Greenhouse gases science and tecnology, vol. 6, pp. 288–301, 2016.

[20] S. Yang and D. Yang, "Integrated characterization of wormhole network by use of a modified pressure-gradient-based (PGB) sand failure criterion and ensemble-based history matching during CHOPS processes," Journal of Petroleum Science and Engineering, no. October 2021, p. 109777, Nov. 2021.

[21] L. Jiang, J. Liu, T. Liu, and D. Yang, "Characterization of Dynamic Wormhole Growth and Propagation During CHOPS Processes by Integrating Rate Transient Analysis and Pressure-Gradient-Based Sand Failure Criterion," in SPE Canadian Energy Technology Conference, 2022.

[22] X. Lei and Z. Gang, "A novel approach for determining wormhole coverage in CHOPS wells," in PE Heavy Oil Conference Canada 2012, 2012, vol. 2, pp. 1531–1549.

[23] L. Xiao and G. Zhao, "Integrated study of foamy oil flow and wormhole structure in CHOPS through transient pressure analysis," in SPE Heavy Oil Conference Canada, 2013, vol. 3, pp. 1946–1960.

[24] H. Yu and J. Y. Leung, "A Sand-Arch Stability Constrained Dynamic Fractal Wormhole Growth Model for Simulating Cold Heavy-Oil Production with Sand," SPE Journal, vol. 25, no. 06, pp. 3440–3456, Dec. 2020.

[25] K. Oldakowski and R. P. Sawatzky, "Direction of wormholes growth under anisotropic stress," in SPE Canada Heavy Oil Technical Conference, 2018.

[26] M. Pereira, "A Physical Model to Assess Sand Production Processes during Cold Heavy Oil Production with Sand," University of Saskatchewan, 2021.

[27] B. Meza-Díaz, R. Sawatzky, and E. Kuru, "Sand on Demand: A Laboratory Investigation on Improving Productivity in Horizontal Wells Under Heavy-Oil Primary Production—Part II," SPE Journal, vol. 17, no. 04, pp. 1012–1028, Dec. 2012.

[28] B. Mathur, A. Y. Dandekar, S. Khataniar, and S. L. Patil, "Life after CHOPS: Alaskan heavy oil perspective," in SPE Western Regional Meeting Proceedings, 2017, vol. 2017-April, pp. 914–927.

[29] J. Chang, J. Ivory, and M. London, "History matches and interpretation of CHOPS performance for CSI field pilot," in Society of Petroleum Engineers - SPE Canada Heavy Oil Technical Conference 2015, CHOC 2015, 2015, pp. 526–544.

[30] K. Oldakowski and R. P. Sawatzky, "Wormhole stability under post chops conditions," Society of Petroleum Engineers - SPE Canada Heavy Oil Technical Conference, CHOC 2018, vol. 2018-Janua, 2018.

[31] A. Mohamad-Hussein et al., "Geomechanical modelling of cold heavy oil production with sand," Petroleum, Mar. 2021.

[32] A. Rangriz Shokri and T. Babadagli, "A sensitivity analysis of cyclic solvent stimulation for post-CHOPS EOR: Application on an actual field case," SPE Economics and Management, vol. 8, no. 4, pp. 78–89, 2016.

[33] B. Yadali Jamaloei, R. Kharrat, and F. Torabi, "Analysis and correlations of viscous fingering in low-tension polymer flooding in heavy oil reservoirs," Energy and Fuels, vol. 24, no. 12, pp. 6384–6392, 2010.

[34] Z. Lin, "Experimental Study About Radial Viscous Fingering in Heavy Oil Reservoir," University of Regina, 2020.

[35] J. G. Maas, N. Springer, A. Hebing, J. Snippe, and S. Berg, "Viscous fingering in CCS - A general criterion for viscous fingering in porous media," International Journal of Greenhouse Gas Control, vol. 132, p. 104074, Feb. 2024.

[36] Y. Soh, A. Rangriz-Shokri, and T. Babadagli, "Optimization of methane use in cyclic solvent injection for heavy-oil recovery after primary production through experimental and numerical studies," Fuel, vol. 214, no. November 2017, pp. 457–470, 2018.

[37] Y. Li et al., "A review of in situ upgrading technology for heavy crude oil," Petroleum, vol. 7, no. 2, pp. 117–122, 2021.

[38] P. H. Krumrine, M. Lefenfeld, and G. A. Romney, "Investigation of post CHOPS enhanced oil recovery of alkali metal silicide technology," in SPE Heavy Oil Conference Canada 2014, 2014, vol. 3, pp. 1634–1650.

[39] Z. Du, F. Zeng, and C. Chan, "An experimental study of the post-CHOPS cyclic solvent injection process," Journal of Energy Resources Technology, Transactions of the ASME, vol. 137, no. 4, pp. 1–15, 2015.

[40] M. Huerta, J. M. Alvarez, E. Jossy, and K. Forshner, "Use of acid gas ($CO2/H2S$) for the Cyclic Solvent Injection (CSI) process for heavy oil reservoirs," Society of Petroleum Engineers - SPE Heavy Oil Conference Canada 2012, vol. 2, pp. 912–921, 2012.

[41] D. F. Cartagena-Pérez et al., "Scaled Physical Modeling of Cyclic CO 2 Injection in Unconsolidated Heavy Oil Reservoirs Using Geotechnical Centrifuge and Additive Manufacturing Technologies," in 2024 SPE Canadian Energy Technology Conference and Exhibition, 2024.

[42] J. Chang and J. Ivory, "Field-scale simulation of cyclic solvent injection (CSI)," Journal of Canadian Petroleum Technology, vol. 52, no. 4, pp. 251–265, 2013.

[43] J. A. Rivero et al., "Modeling CHOPS Using a Coupled Flow-Geomechanics Simulator With Nonequilibrium Foamy-Oil Reactions: A Multiwell History Matching Study," in SPE Annual Technical Conference and Exhibition, 2010.

[44] A. Rangriz Shokri and T. Babadagli, "An approach to model CHOPS (cold heavy oil production with sand) and post-CHOPS applications," in Proceedings - SPE Annual Technical Conference and Exhibition, 2012, vol. 3, no. 1, pp. 2305–2316.

[45] A. S. Haddad and I. Gates, "Modelling of Cold Heavy Oil Production with Sand (CHOPS) using a fluidized sand algorithm," Fuel, vol. 158, pp. 937–947, Oct. 2015.

[46] B. Vanderheyden, B. Jayaraman, X. Ma, and D. Zhang, "Multiscale Simulation of CHOPS Wormhole Networks," in SPE Reservoir Simulation Symposium, 2013.

[47] H. Ma, G. Yu, Y. She, and Y. Gu, "A new hybrid production optimization algorithm for the combined CO2-cyclic solvent injection (CO2-CSI) and water/gas flooding in the post-CHOPS reservoirs," Journal of Petroleum Science and Engineering, vol. 170, no. January, pp. 267–279, 2018.

[48] M. Zhang, Z. Du, F. Zeng, and S. Xu, "Upscaling study of cyclic solvent injection process for post-chops reservoirs through numerical simulation," in Society of Petroleum Engineers - SPE Heavy Oil Conference Canada 2014, 2014, vol. 3, pp. 1651–1669.

[49] J. J. Martinez Gamboa and J. Y. Leung, "Design of field-scale cyclic solvent injection processes for post-CHOPS applications," Canadian Journal of Chemical Engineering, vol. 97, no. 1, pp. 123–132, 2019.

[50] J. Chang, J. Ivory, and G. Beaulieu, "Pressure maintenance at post-CHOPS cyclic solvent injection (CSI) well using gas injection at offset well," in SPE Heavy Oil Conference, 2014, vol. 2, pp. 1387–1409.

[51] X. Tang, C. Yu, Y. Bai, H. Lu, and M. S. Mohamed, "Field Trial of Nitrogen-Assisted Cyclic Steam Stimulation in Post-CHOPS Wells, Case Study in Sudan," in SPE Thermal Well Integrity and Production Symposium, 2022.

A Summary of Geotechnical Centrifuge Applications in Petroleum Engineering

G. Madabhushi, Centrifuge modelling for civil engineers. 2017.

[2] R. Phillips, “Computes Reudus de l’Academie des Sciences.” Paris, p. 68, 1869.

[3] P. H. Joseph, H. H. Einstein, and R. V. Whitman, “A literature review of geotechnical centrifuge modeling with particular emphasis on rock mechanics,” 1988.

[4] M. Budhu, Soil mechanics and foundations, 3rd ed. John Wiley & Sons, 2010.

[5] J. M. Duncan, S. G. Wright, and T. L. Brandon, Soil strength and slope stability, 2nd ed. New Jersey: Wiley, 2014.

[6] B. Das and N. Sivakugan, Fundamentals of geotechnical engineering. Boston: Cengage Learning, 2017.

[7] C. W. W. Ng, “The state-of-the-art centrifuge modelling of geotechnical problems at HKUST,” Journal of Zhejiang University SCIENCE A, vol. 15, no. 1, pp. 1–21, Jan. 2014.

[8] R. N. Taylor, Geotechnical Centrifuge Technology, 1st ed. London: Taylor & Francis, 1995.

[9] E. M. J. S. Lemoine, “Modelling Sand Production in a Geotechnical Centrifuge,” Dalhousie

University, 1999.

[10] R. Butterfield, “Scale-modelling of fluid flow in geotechnical centrifuges,” Soils and Foundations, vol. 40, no. 6, pp. 39–45, 2000.

[11] H. H. Vaziri and L. Lemoine, “Strong support for significant productivity boost through sand production,” in 4th North American Rock Mechanics Symposium, NARMS 2000, 2000, pp. 295–302.

[12] H. H. Vaziri, S. Thallak, and R. Phillips, “Centrifuge tests to identify mode of sand production and its effect on production,” International Journal of Rock Mechanics and Mining Sciences, vol. 35, no. 4–5, p. 75, 1998.

[13] M. Pereira, “A Physical Model to Assess Sand Production Processes during Cold Heavy Oil Production with Sand,” University of Saskatchewan, 2021.

[14] M. B. Dusseault, “CHOPS: Cold Heavy Oil Production with Sand in the Canadian heavy oil industry,” Waterloo, 2002.

[15] C. M. Istchenko and I. D. Gates, “Well/wormhole model of cold heavy-oil production with sand,” SPE Journal, vol. 19, no. 2, pp. 260–269, 2014.

[16] S. Layeghpour, “Geotechnical centrifuge experiments to improve understanding of sand

production from heavy oil reservoirs," University of Saskatchewan, 2021.

[17] P. Ian, V. Hans, W. Stephen, M. Zissis, C. John, and I. Ion, "Predicting and Managing Sand Production: A New Strategy," in Proceedings of SPE Annual Technical Conference and Exhibition, 2003, pp. 3949–3961.

[18] B. G. do. S. Costa, M. A. Jaculli, J. R. P. Mendes, and D. Colombo, "Evaluation of rock integrity during well drilling activities using reliability analysis," Journal of Petroleum Science and Engineering, vol. 200, p. 108405, May 2021.

[19] I. Okamoto, X. Li, and T. Ohsumi, "Effects of Supercritical CO2 on the Integrity of Cap Rock," in Greenhouse Gas Control Technologies - 6th International Conference, Elsevier, 2003, pp. 483–488.

[20] S. Jia, "Bean Centrifuge Modelling of Caprock Integrity," University of Alberta, 2021.

[21] J. D. Murff, "The geotechnical centrifuge in offshore engineering," Proceedings of the Annual Offshore Technology Conference, vol. 1, pp. 675–689, 1996.

[22] A. B. Cooke and R. J. Mitchell, "Soil column drainage modelling using a geotechnical centrifuge," Geotechnical Testing Journal, vol. 14, no. 3, pp. 323–327, 1991.

[23] D. N. Singh, S. J. Kuriyan, and V. Madhuri, "Application of a Geotechnical Centrifuge for Estimation of Unsaturated Soil Hydraulic Conductivity," Journal of Testing and Evaluation, vol. 29, no. 6, pp. 556–562, 2001.

[24] D. N. Singh and A. K. Gupta, "Falling Head Hydraulic Conductivity Tests in a Geotechnical Centrifuge," Journal of Testing and Evaluation, vol. 29, no. 3, pp. 258–263, 2001.

[25] O. Oung et al., "Investigation of a european network of geotechnical centrifuge on multiphase flow," International Journal of Physical Modellin in Geotechnics, vol. 1, pp. 01–14, 2005.

[26] J. Nayser, E. Pooley, and S. Springman, "Modelling of double porosity clays in a mini-centrifuge," International Journal of Physical Modellin in Geotechnics, vol. 1, pp. 15–22, 2009.

[27] T. E. Noble and J. M. Dixon, "Structural evolution of fold-thrust structures in analog models deformed in a large geotechnical centrifuge," Journal of Structural Geology, vol. 33, no. 2, pp. 62–77, 2011.

[28] M. Rojhani, M. Moradi, M. H. Ebrahimi, A. Galandarzadeh, and S. Takada, "Recent developments in faulting simulators for geotechnical centrifuges," Geotechnical Testing Journal, vol. 35, no. 6, pp. 924–934, 2012.

[29] M. B. Dusseault, “Stress Changes in Thermal Operations,” in SPE International Thermal Operations Symposium, 1993.

[30] S. Krishnaiah and D. N. Singh, “Centrifuge Modelling of Heat Migration in Soils,” International Journal of Physical Modellin in Geotechnics, vol. 3, pp. 39–47, 2004.

[31] M. D. Zoback, Resevoir Geomechanics, 1st ed. New York: Cambridge University Press, 2007.

[32] E. Fjær, R. M. Holt, P. Horsrud, A. M. Raaen, and R. Risnes, Petroleum Related Rock Mechanics. Elsevier, 2008.

[33] G. E. King and R. L. Valencia, “Well Integrity for Fracturing and Re-Fracturing: What Is Needed and Why?,” in SPE Hydraulic Fracturing Technology Conference, 2016.

[34] B. Carey, “Wellbore integrity and CO2 sequestration.” .

[35] W. Ovalle-Villamil and I. Sasanakul, “Assessment of centrifuge modelling of internal erosion induced by upward flow conditions,” International Journal of Physical Modelling in Geotechnics, vol. 21, no. 5, pp. 251–267, 2021.

An Approach to Model Cyclic CO2 Injection Process in Poorly Cemented Heavy Oil Reservoirs Using a Novel Geotechnical Centrifuge Cell and 3D Printed Rocks

M. B. Dusseault, “CHOPS: Cold Heavy Oil Production with Sand in the Canadian heavy oil industry,” Waterloo, 2002.

[2] D. F. Cartagena-Pérez, G. A. Alzate-Espinosa, and A. Arbelaez-Londoño, “Conceptual evolution and practice of sand management,” *Journal of Petroleum Science and Engineering*, vol. 210, Mar. 2022.

[3] A. Rangriz Shokri and T. Babadagli, “A sensitivity analysis of cyclic solvent stimulation for post-CHOPS EOR: Application on an actual field case,” *SPE Economics and Management*, vol. 8, no. 4, pp. 78–89, 2016.

[4] B. Yadali Jamaloei, R. Kharrat, and F. Torabi, “Analysis and correlations of viscous fingering in low-tension polymer flooding in heavy oil reservoirs,” *Energy and Fuels*, vol. 24, no. 12, pp. 6384–6392, 2010.

[5] Z. Lin, “Experimental Study About Radial Viscous Fingering in Heavy Oil Reservoir,” University of Regina, 2020.

[6] D. W. Zhao, J. Wang, and I. D. Gates, “Thermal recovery strategies for thin heavy oil

reservoirs," *Fuel*, vol. 117, pp. 431–441, Jan. 2014.

[7] G. Coskuner and H. Huang, "Enhanced oil recovery in post-CHOPS cold heavy oil production with sand heavy oil reservoirs of Alberta and Saskatchewan part 2: Field piloting of cycling solvent injection," *Society of Petroleum Engineers - SPE Canada Heavy Oil Conference 2020, CHOC 2020*, vol. 3, 2020.

[8] S. Layeghpour, "Geotechnical centrifuge experiments to improve understanding of sand production from heavy oil reservoirs," University of Saskatchewan, 2021.

[9] M. Dusseault and F. J. Santarelli, "A conceptual model for massive solids production in poorly-consolidated sandstones," in *ISRM International Symposium*, 1989, pp. 789–797.

[10] K. Oldakowski and R. P. Sawatzky, "Direction of wormholes growth under anisotropic stress," in *SPE Canada Heavy Oil Technical Conference*, 2018.

[11] G. Zambrano-Narvaez and R. J. Chalaturnyk, "The new GeoREF geotechnical beam centrifuge at the University of Alberta, Canada," in *Physical Modelling in Geotechnics*, C. Gaudin and D. White, Eds. London: Taylor & Francis Group, 2014, pp. 163–167.

[12] J. S. Gomez, R. J. Chalaturnyk, and G. Zambrano-Narvaez, "Experimental Investigation of the Mechanical Behavior and Permeability of 3D Printed Sandstone Analogues Under Triaxial Conditions," *Transport in Porous Media*, vol. 129, no. 2, pp. 541–557, 2019.

[13] J. S. Gomez, "Mechanical Properties Characterization of Printed Reservoir Sandstone Analogues," 2017.

[14] R. N. Taylor, Geotechnical Centrifuge Technology, 1st ed. London: Taylor & Francis, 1995.

[15] T. Ahmed and P. McKinney, *Advanced Reservoir Engineering*, 1st Ed. Elsevier, 2005.

[16] J. Lee, *Well Testing*. Society of Petroleum Engineers, 1982.

[17] H. Jourde, F. Cornaton, S. Pistre, and P. Bidaux, "Flow behavior in a dual fracture network," *Journal of Hydrology*, vol. 266, no. 1–2, pp. 99–119, Sep. 2002.

[18] M. Pereira, "A Physical Model to Assess Sand Production Processes during Cold Heavy Oil Production with Sand," University of Saskatchewan, 2021.

[19] E. Fjær, R. M. Holt, P. Horsrud, A. M. Raaen, and R. Risnes, *Petroleum Related Rock Mechanics*. Elsevier, 2008.

[20] B. Tremblay and K. Oldakowski, "Modeling of wormhole growth in cold production," *Transport*

in Porous Media, vol. 53, no. 2, pp. 197–214, 2003.

[21] H. H. Vaziri and L. Lemoine, “Strong support for significant productivity boost through sand production,” in *4th North American Rock Mechanics Symposium, NARMS 2000*, 2000, pp. 295–302.

Mechanical and Hydraulic Characterization of 3D Printed Rocks at Low Binder Saturation as Analogs to Poorly Cemented Sandstone Rocks

[1] B. Primkulov, J. Chalaturnyk, R. Chalaturnyk, and G. Zambrano Narvaez, “3D printed sandstone strength: Curing of furfuryl alcohol resin-based sandstones,” *3D Printing and Additive Manufacturing*, vol. 4, no. 3, pp. 149–155, 2017.

[2] K. J. Hodder, A. J. Sanchez-Barra, S. Ishutov, G. Zambrano-Narvaez, and R. J. Chalaturnyk, “Increasing Density of 3D-Printed Sandstone through Compaction,” *Energies*, vol. 15, no. 5, 2022.

[3] A. Sanchez-Barra, G. Zambrano-Narvaez, and R. Chalaturnyk, “An In-Depth Analysis of Strength and Stiffness Variability in 3D-Printed Sandstones: Implications for Geomechanics,” *Energies*, vol. 16, no. 14, p. 5406, Jul. 2023.

[4] Water Resources Mission Area, “Unconsolidated and semiconsolidated sand and gravel aquifers,” 2021. [Online]. Available: https://www.usgs.gov/mission-areas/water-resources/science/unconsolidated-and-semiconsolidated-sand-and-gravel-aquifers. [Accessed: 17-Feb-2024].

[5] D. Cartagena Perez *et al.*, “Scaled Physical Modeling of Cyclic CO2 Injection in Unconsolidated Heavy Oil Reservoirs Using Geotechnical Centrifuge and Additive Manufacturing Technologies,” in *SPE Canadian Energy Technology Conference and Exhibition*, 2024.

[6] J. S. Gomez, “Mechanical Properties Characterization of Printed Reservoir Sandstone Analogues,” 2017.

[7] ASTM, “Standard Test Method for Unconfined Compressive Strength of Cohesive Soil 1,” *ASTM International*, no. January. 2013.

[8] P. Li and R. J. Chalaturnyk, “Geomechanical Model of Oil Sands,” in *SPE International Thermal Operations and Heavy Oil Symposium*, 2005.

[9] E. F. Araujo-Guerrero, G. A. Alzate-Espinosa, J. G. Osorio, R. Chalaturnyk, and G. Zambrano, “Advanced geomechanically laboratory testing for sand production with aids of 3D printing technology,” *55th U.S. Rock Mechanics / Geomechanics Symposium 2021*, vol. 4, 2021.

[10] J. Chang, J. Ivory, and G. Beaulieu, "Pressure maintenance at post-CHOPS cyclic solvent injection (CSI) well using gas injection at offset well," in *SPE Heavy Oil Conference*, 2014, vol. 2, pp. 1387–1409.

[11] A. Salimnezhad, H. Soltani-Jigheh, and A. A. Soorki, "Effects of oil contamination and bioremediation on geotechnical properties of highly plastic clayey soil," *Journal of Rock Mechanics and Geotechnical Engineering*, vol. 13, no. 3, pp. 653–670, Jun. 2021.

[12] N. A. Ardila Angulo, "Hydraulic properties characterization of 3D printed sandstone analogues," University of Alberta, 2018.

[13] J. S. Gomez, R. J. Chalaturnyk, and G. Zambrano-Narvaez, "Experimental Investigation of the Mechanical Behavior and Permeability of 3D Printed Sandstone Analogues Under Triaxial Conditions," *Transport in Porous Media*, vol. 129, no. 2, pp. 541–557, 2019.

[14] B. Das and N. Sivakugan, *Fundamentals of geotechnical engineering*. Boston: Cengage Learning, 2017.

[15] W. Frenelus, H. Peng, and J. Zhang, "Creep Behavior of Rocks and Its Application to the Long-Term Stability of Deep Rock Tunnels," *Applied Sciences*, vol. 12, no. 17, p. 8451, Aug. 2022.

[16] K. J. Hodder, K. Craplewe, S. Ishutov, and R. Chalaturnyk, "Binder Saturation as a Controlling Factor for Porosity Variation in 3D-Printed Sandstone," *Petrophysics*, vol. 62, no. 5, pp. 450–462, 2021.

[17] M. Budhu, *Soil mechanics and foundations*, 3rd ed. John Wiley & Sons, 2010.

[18] ASTM, "Standard Test Method for Permeability of Granular Soils (Constant Head)." 2000.

[19] E. E. G. Rojas, J. S. R. Coimbra, and J. Telis-Romero, "Thermophysical Properties of Cotton, Canola, Sunflower and Soybean Oils as a Function of Temperature," *International Journal of Food Properties*, vol. 16, no. 7, pp. 1620–1629, Oct. 2013.

Appendix A:

Callibrations and Checking of Sensors and Devices

To ensure the accuracy and reliability of our experimental procedure, a comprehensive series of calibration and performance tests were conducted on various components of the centrifuge cell and setup. Given the unique requirements of certain components, particularly those reliant on specific mechanisms, such as enhanced gravity, calibration tests were performed under these conditions.

Horizontal stress actuators calibration

Prior to calibrating the pistons of the horizontal confining system, attention was directed towards the calibration of the sensors integral to the setup, namely the pressure transducers and load cell. These sensors play a critical role in accurately measuring the stress applied to the sample during testing. Additionally, the horizontal confining system, comprising eight pistons driven by hydraulic motion facilitated by two step motors, required calibration to establish the relationship between the number of motor steps and the resulting stress exerted on the sample. This calibration process is essential to ensure the precision and reliability of the tests conducted in our research.

Pressure transducer calibration

To ensure the correct record of the pressure/stress during the main test as well as during commissioning and supplemental ones, it is necessary to calibrate the pressure transducers. To accomplish this task, a GE Druck DPI 603 - Portable Pressure Calibrator (Fig 8-1) with a maximum operation pressure of 2067 kPa (300 psi) was employed. This tool allows us to get the relationship between the applied pressure and the electrical response from the sensor in terms of voltages.

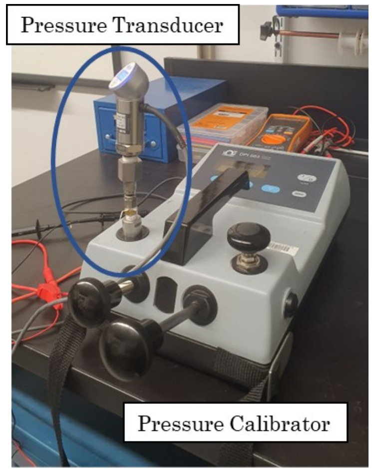

Fig 8-1. GE Druck DPI 603 - Portable Pressure Calibrator used during calibration.

In general, the procedure consists in increasing the pressure manually while recording the outcome voltage. Once the data is obtained, it is plotted, and the coefficient of determination (R^2) is calculated to ensure the linearity of the relationship between pressure and voltage. The results for three of the pressure transducers are shown below in the Fig 8-2, Fig 8-3, and Fig 8-4: For all the pressure transducers the coefficient of determination was higher than 99.6% which means that the reliability of the sensor is proved for experimental purposes.

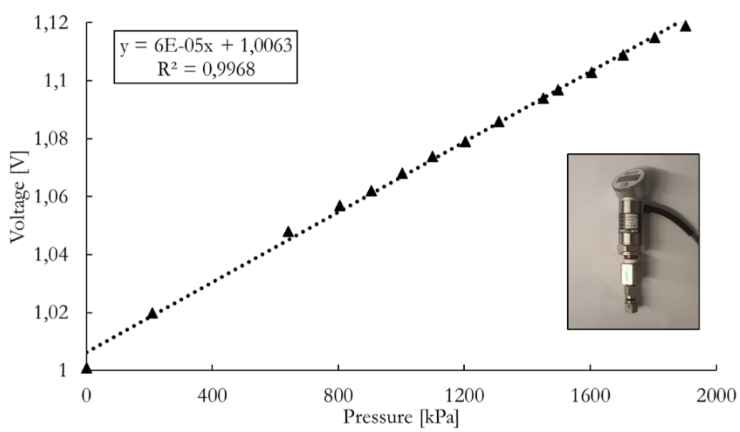

Fig 8-2. Calibration of pressure transducer 1

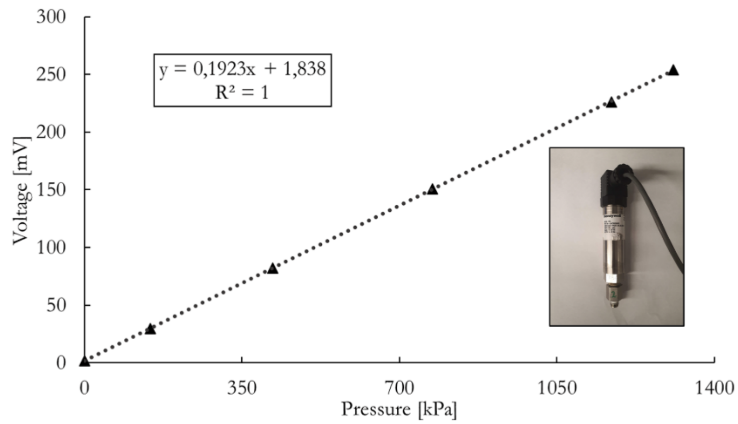

Fig 8-3. Calibration of Pressure Transducer 2

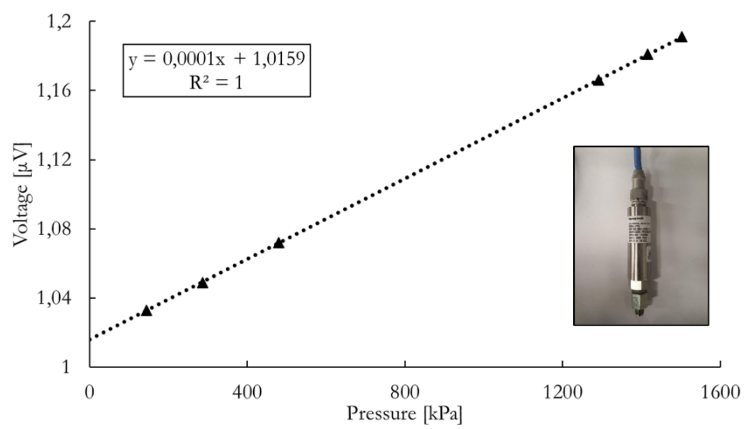

Fig 8-4. Calibration of Pressure Transducer 3

Load Cell Calibration

Similarly to the process used to calibrate the pressure transducers, the load cell (Omega-LCMHD-10K) underwent calibration using weights instead of pressure. The general setup for the calibration process is illustrated in Fig 8-5. This calibration procedure ensures accurate measurements of the applied loads during the experiments.

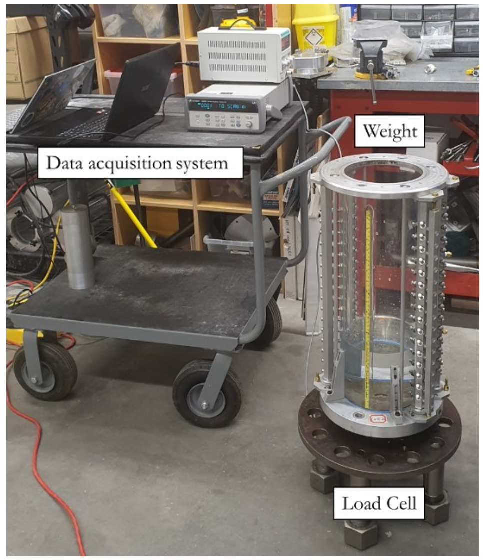

Fig 8-5. Load cell Omega-LCMHD-10K used during calibration and loading system.

The results from this calibration are shown in Fig 8-6. With a determination coefficient of 99,9%, the resolution and response of the sensor are accurate for the test.

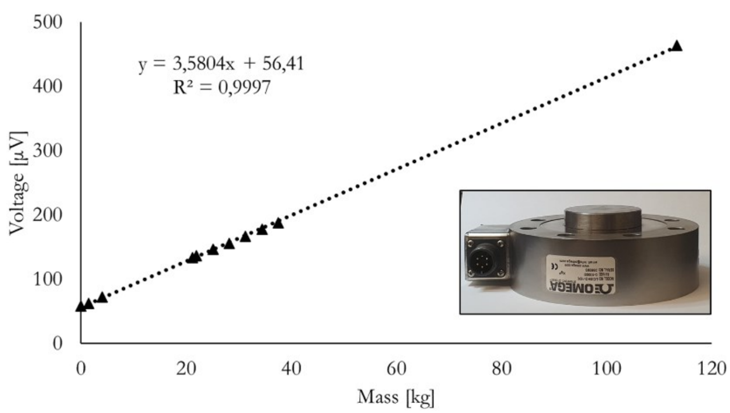

Fig 8-6. Calibration of load cell.

Calibration of the actuator

The calibration of the pistons aims to give an idea of how many steps of the motor are required to achieve a given confining stress. Since the centrifuge cell applies the confining stress through actuators (pistons), the calibration gives the relationship between the motor and the actual stress "felt" by the sample. In general, the setup (Fig 8-7) uses a motor connected to a hydraulic oil reservoir that pressurizes the piston. Once the pressure inside the piston excesses the frictional resistance, it begins to move against the load cell. Each movement of the piston represents a higher stress over the load cell (Similarly to the way the sample is comprised).

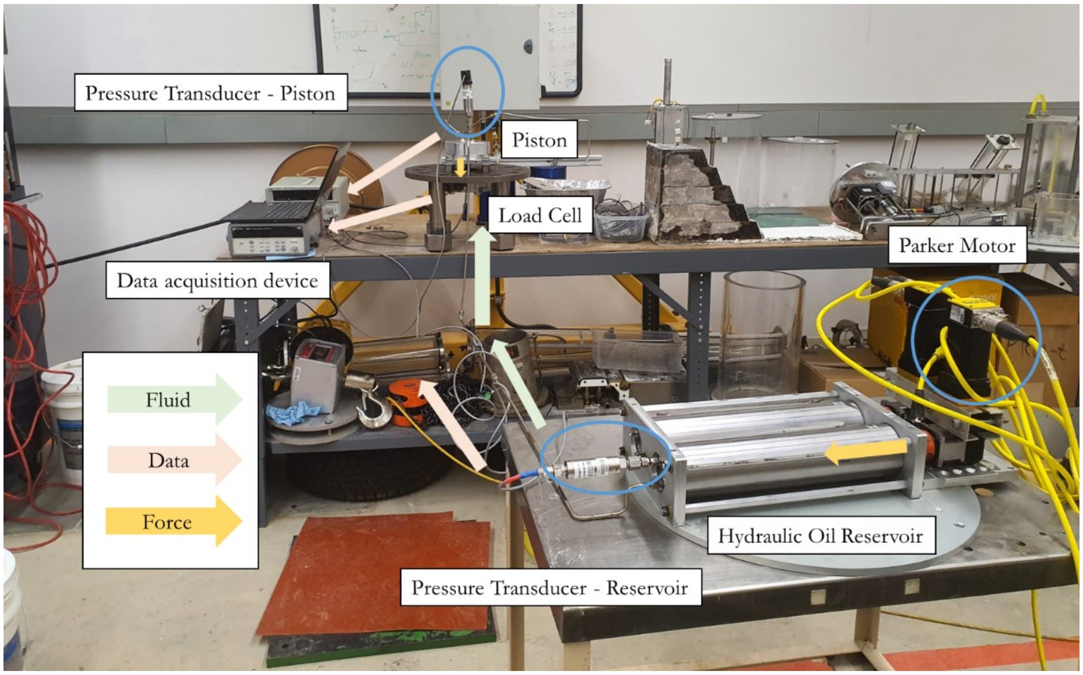

Fig 8-7. General calibration setup. Color arrows show the direction of fluid flow, data, and forces.

With this process, it is possible to represent the pressure in the hydraulic oil reservoir, at the entrance of the piston, and the load cell against the number of steps of the motor. This is recorded and shown in Fig 8-8:

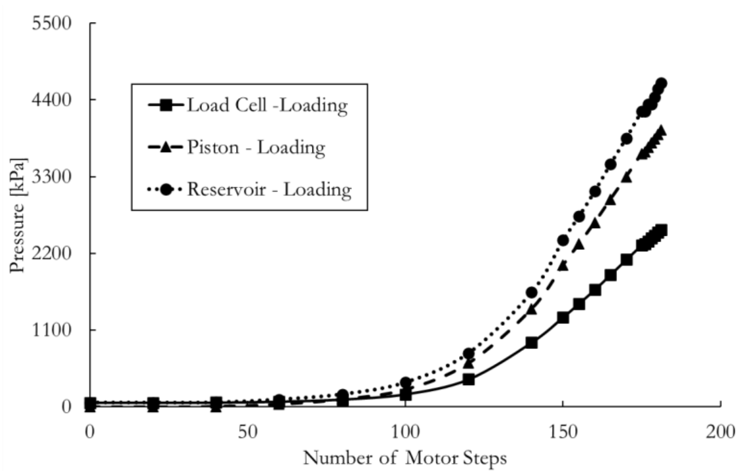

Fig 8-8. *Relationship between pressures and number of motor's steps*

Once the pressure over the load cell is equal to 2.5 MPa (The maximum operation stress for the cell), the direction of the motor is inverted to retract the displacement within the hydraulic oil reservoir and doing so, remove the pressure inside the piston. The readings of the pressure during the unloading are shown in Fig 8-9. In general, the unloading path is statistically the same as the one in loading. To confirm those results, a second test was executed.

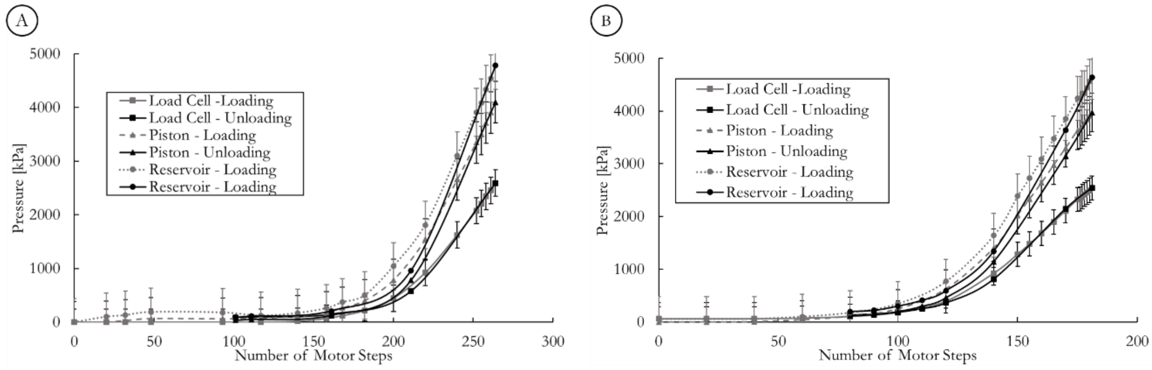

Fig 8-9. *a) First test of the relationship between motor steps and pressures in different parts of the system. b) Second test of relationship between motor steps and pressures in different parts of the system.*

Despite both Figures confirm the trending of the pressure, a best fitting is obtained when the relationship is done with the piston pressure and the load cell (Fig 8-10). It means, that from an engineering point of view, a better way to monitor the confining horizontal stresses applied to the sample is through a pressure transducer outside the piston device.

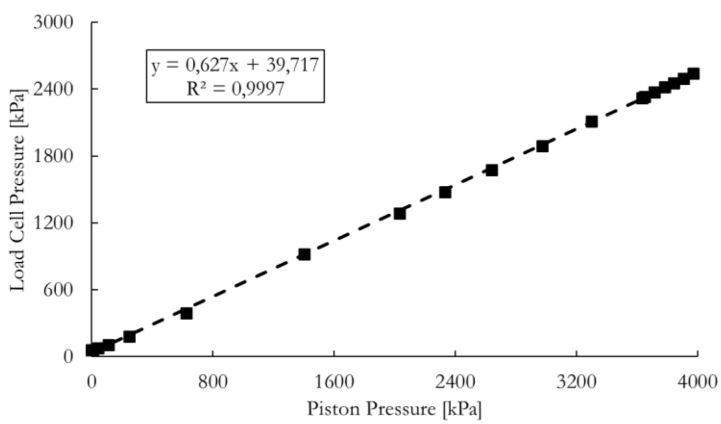

Fig 8-10. Relationship between pressures in the piston and load cell.

The suggested question to calculate the stress is:

$$\sigma_h\ [kPa] = 0{,}627 * (Piston\ Pressure\ [kPa]) + 39{,}717$$

Pressure transducer calibration.

In a similar way to the calibration done to the auxiliary pressure transducer used during the stress actuators adjustment, the pressure transducer that are placed inside the cell during the tests were subjected to a calibration. These sensors are responsible for measuring the changes in the pore pressure during the test.

To guarantee the nearest conditions to test, these calibrations are done in the centrifuge pit providing power through the rotary union. The general setup is shown below in Fig 8-11:

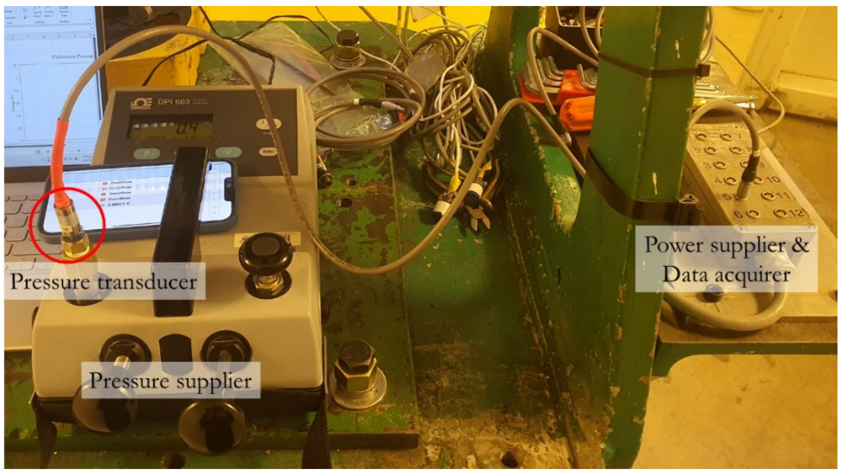

Fig 8-11. Setup for the pressure transducer calibration in the centrifuge pit.

The procedure is identical to the one used to calibrate the pressure transducers for the stress actuators adjustments. The results are shown in the following figures.

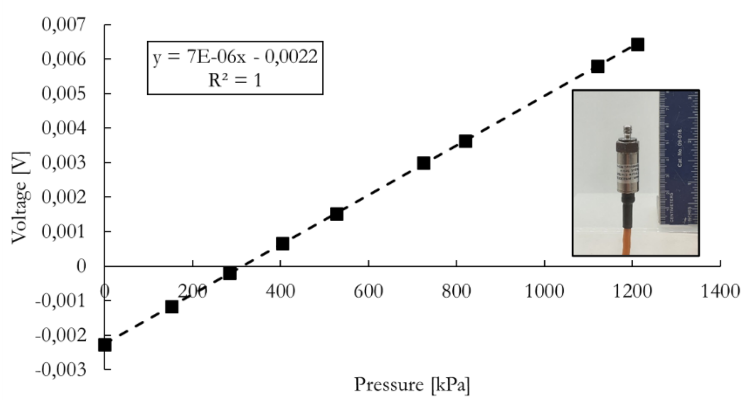

Fig 8-12. Calibration of pressure transducer 1, pressure vs voltages.

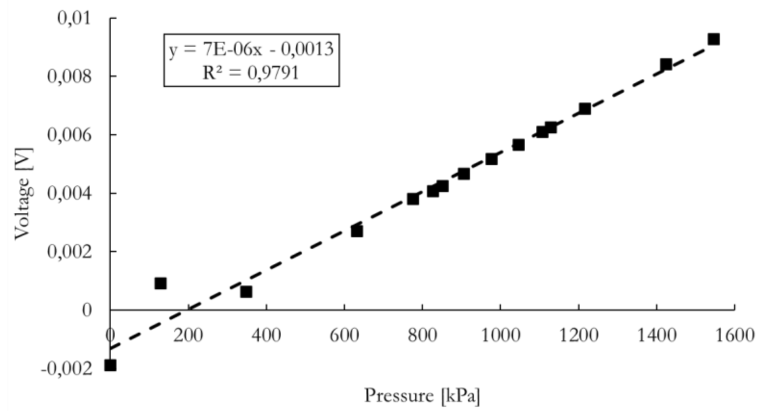

Fig 8-13. Calibration of pressure transducer 2, pressure vs voltages.

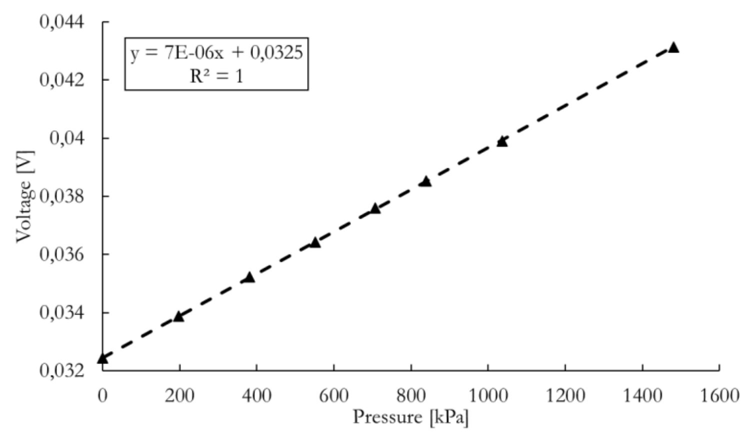

Fig 8-14. Calibration of pressure transducer 3, pressure vs voltages.

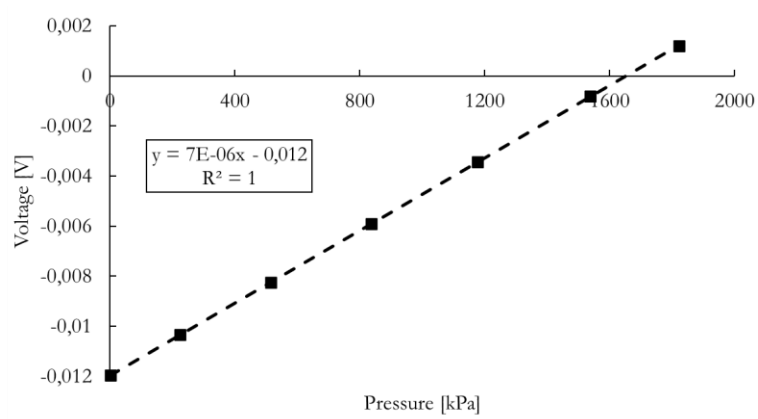

Fig 8-15. Calibration of pressure transducer 4, pressure vs voltages.

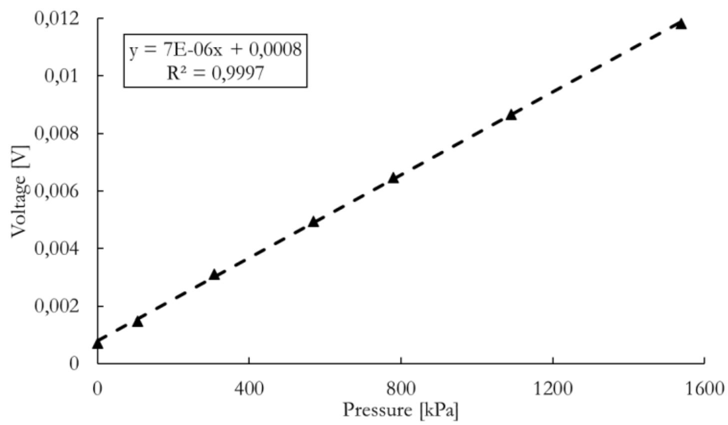

Fig 8-16. Calibration of pressure transducer 5, pressure vs voltages

The results of the multiple calibration point out a good performance of the devices with coefficients of determination near to 1.

Solenoid valve

A solenoid valve is an electromechanical device designed to control the flow and remotely activated thanks to their solenoid coil. Fig 8-17 illustrates the main elements of a solenoid valve. The mechanism behind this kind of valve is the electro magnetic field that is created in the solenoid coil when an electrical current goes through moving up the plunger. Therefore, the correct performance of this kind of valve relies on the balance of forces between the magnetic field and the weight of the plunger.

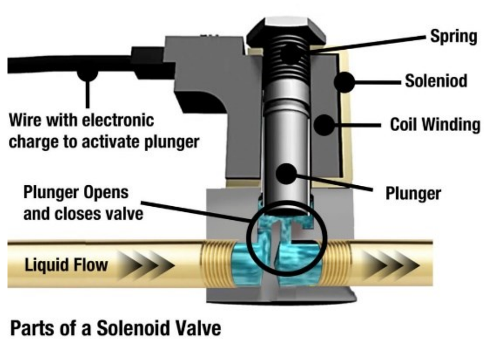

Fig 8-17. Solenoid valve diagram. Taken from [1]

Since the functional mechanism of the solenoid valve depends on the plunger weight, a commissioning test is run at enhanced gravity field to ensure that the plunger can be released. Fig 8-18 shows the basic setup prepared for this test, it consists in two reservoirs connected by the solenoid valve. If the valve works properly, a transit of fluid is allowed at enhanced gravity, leading to equalizing the fluid levels on both reservoirs.

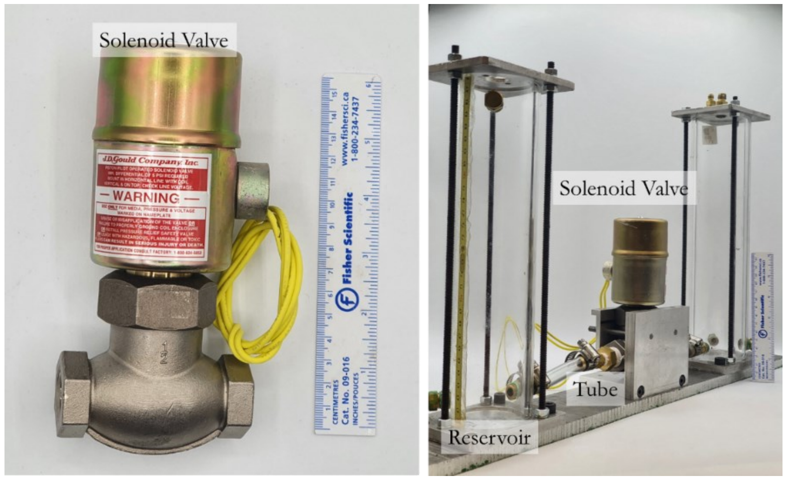

Fig 8-18. Solenoid Valve (left) and Setup to commission the solenoid valve

The following pictures shows the result of this experiment when the solenoid valve is place horizontal and vertically:

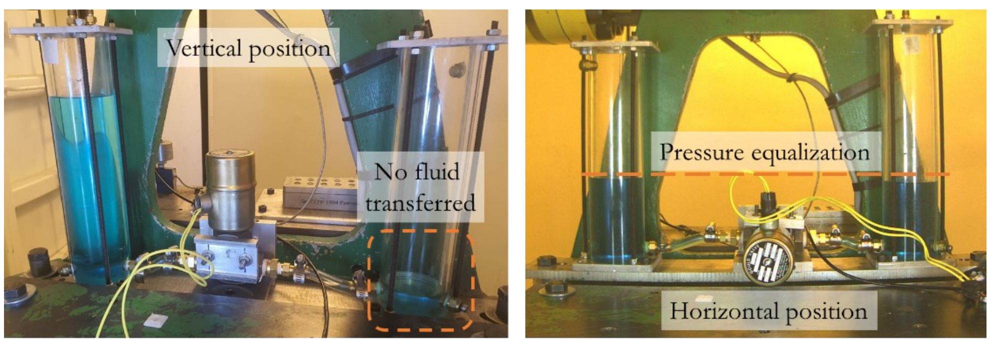

Fig 8-19. Commissioning of solenoid valve at enhanced gravity. Solenoid valve at vertical position (left) and horizontal position (right)

Since the horizontal position cannot be used during the spin of the centrifuge, a decision was made to replace the solenoid valve for a manual one.

Pressure transducers and parker motor interference.

Additional to the pressure transducers (PT) that are attached to the sample's base to follow the pore pressure during the tests, some sensors are required to know the pressure in the confining stress system and the supplied pressure to the membrane (i.e. Testing pressure transduces). To complete this task, calibrated and reliable sensors are used as a reference and connected to the parker motor that induces the pressure. A scheme of the setup is shown in Fig 8-20. In general, parker motor pressurizes the fluid inside the accumulators and the pressure transducers read the signal.

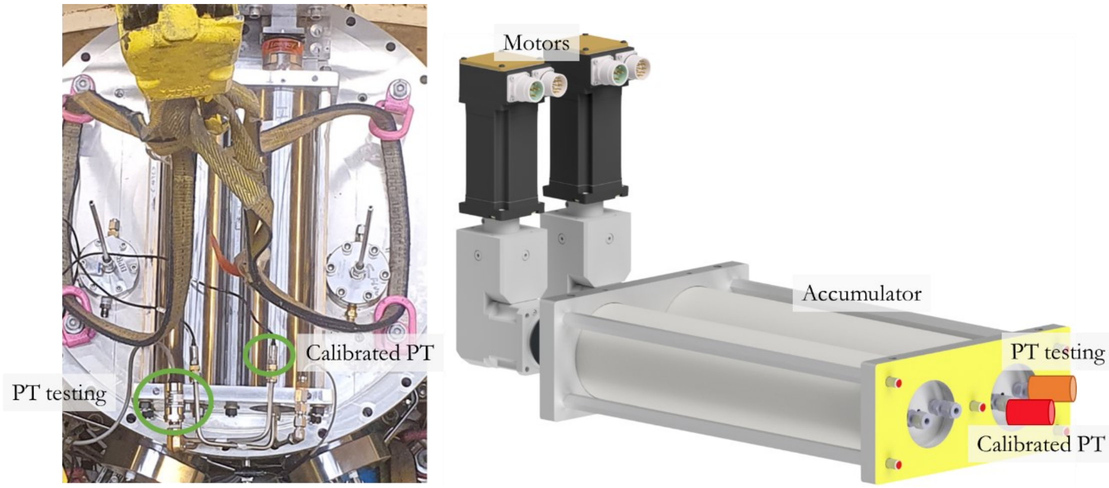

Fig 8-20. Setup for the pressure transducer calibration with parker motors

The signal of the calibrated and testing pressure transducer is shown in the following figure.

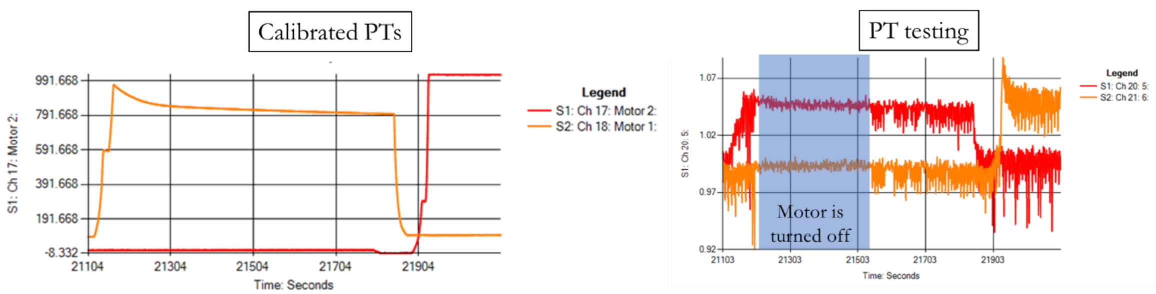

Fig 8-21. Signal of the pressure transducer (calibrated and testing) in both motors.

From Fig 8-21, it is evident that there is so much noise in the signal of the testing pressure transducers. It is important to note that the signal in the Y-axis of the chart at the right is in volts, it means that no transformation is applied to the output. A second important aspect is that the impact of the noise seems to be due to the parker motor in a way that the signal is smoother when the motor is turned off and noisy when the motor is turned on. This behavior is explained as the interference of an electromagnetic field created by the motor that perturbates the outcome signal of the pressure transduces, that usually is in mV, it means that the outcome signal is small enough to be altered by the electromagnetic field.

To solve this problem, a ground mechanism is used, the chosen pressure transducers have outcome in order of V instead of mV, and they are placed far from the parker motor. A new test is run, and the results are shown in Fig 8-22. It is found that this technique helps reduce the noise in the outcome signal. Despite some interfere is still present, it can be corrected easily with the calibration equation to convert from voltage to pressure.

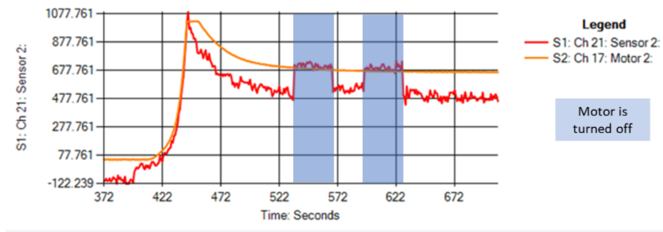

Fig 8-22. Signal of the pressure transducer after handle the electromagnetic field.

Back Pressure Regulators

A back-pressure regulator (BPR) is defined as "a device that maintains a defined pressure upstream of its own inlet. When fluid pressure in the process at the inlet of the BPR exceeds the setpoint, the regulator opens to relieve the excess pressure."[2]. A general diagram of a BPR is shown in Fig 8-23 next to a picture of one of the BPR used for the setup. These devices help to control and moderate the flow from inside the cell to the acrylic accumulators. To commission them, one test at 1G is performed and a second at 30 Gs as well to warranty the proper work for the BPR.

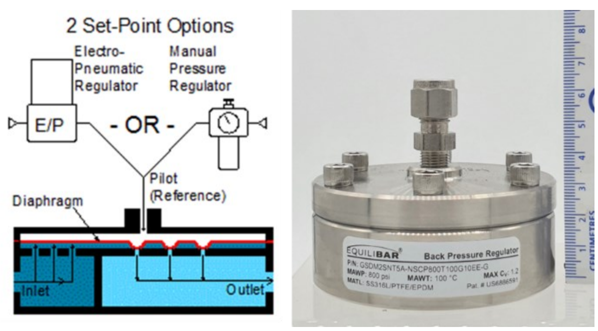

Fig 8-23. BPT diagram (left) and BPR used during the tests (right).

The general setup for the tests at 1G and 30G is shown in Fig 8-24. It is useful to note that the outlet of the BPR is closed to a pressure transducer. Also, the operational procedure takes compressed nitrogen from the bottles at surface and transports it through the rotary union.

This procedure is conducted for both BPR's that will be used during the test.

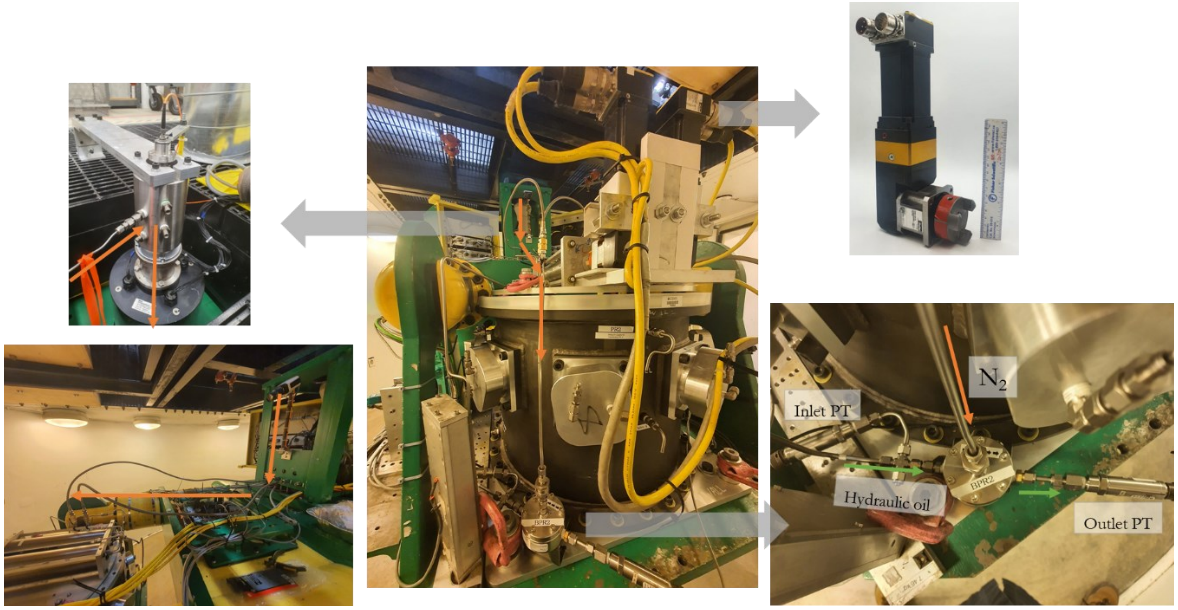

Fig 8-24. BPR setup testing.

BPR 1

The BPR 1 is an Equilibar GSDM2SNT5A (Fig 8-25) with a maximum operational pressure of 800 psi [5515,81 kPa].

Fig 8-25. Back pressure regulator.

The inlet and outlet ports in this BPR are horizontal while the reference pressure point is vertical. The testing results for this BPR are described below.

Tests of the BPR-1 at 1 G

In this test, a reference pressure of 3 MPa is applied, and a pressurized fluid is injected to the BPR while record of the outlet's pressure is recorded. Fig 8-26 shows how the pressure behaves during the test at both endings of the BPR.

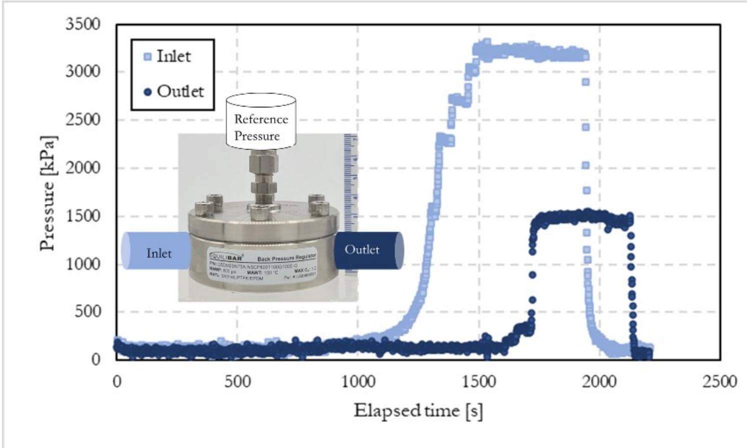

Fig 8-26. Test of BPR-1 at 1G

From the Figure, it is evident that the BPR is working properly since the outlet's pressure does not increase until the inlet excesses 3 MPa which happens approximately at the second 1500.

BPR1 tests at 30Gs

Using the setup described at Fig 8-24, the BPR is tested at 30Gs. The results are presented at Fig 8-27 and show how at enhanced gravity, the BPR1 works. The results also highlight the effect of the gravity during the flow. In this test, once the inlet pressure reaches the 3 MPa of the reference pressure, the flow is fast, and that is symptomatic of the high slope in the curve that describes the outlet pressure. Wich quickly reaches the same 3MPa.

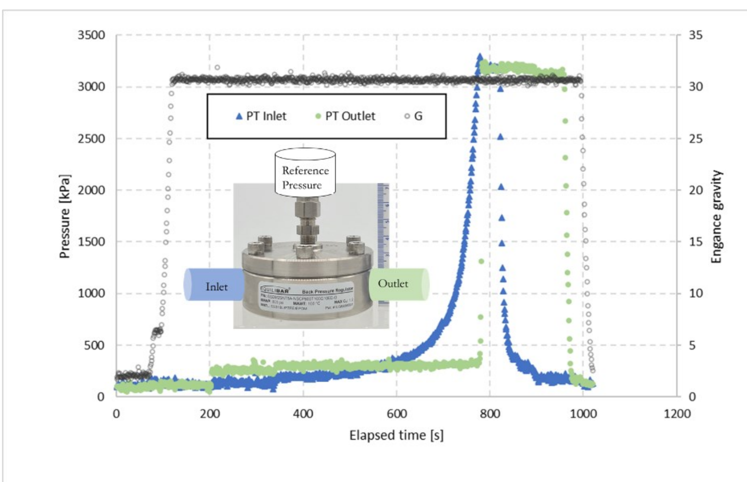

Fig 8-27. BPR 1 test at 30 Gs

BPR2

The BPR2 is an Equilibar GSDH2SNT5A (**Fig *8-28***) with a maximum operational pressure of 800 psi [5515,81 kPa].

Fig 8-28. Back Pressure Regulator (BPR) 2

Like the procedure that is conducted for the BPR1, a set of tests at 1 and 30G's are carried out to determine the capability of the device.

Tests of the BPR2 at 1G

In this test, a reference pressure of approximately 3000 kPa is applied to the BPR, then an inlet pressure is built up with the aim of the Parker motors, when this pressure reaches the reference one, fluid is allowed through the BPR. The Fig 8-29 shows the behavior of the pressure at both endings of the BPR 2 during the test. Near to the second 1000, the inlet pressure increases by steps because of the step system of the Parker motors. At second 1600 (approx.) the flow begins causing that the pressure in the inlets to stand stable and the outlet pressure increases. This test confirms that the BPR2 works at 1 G.

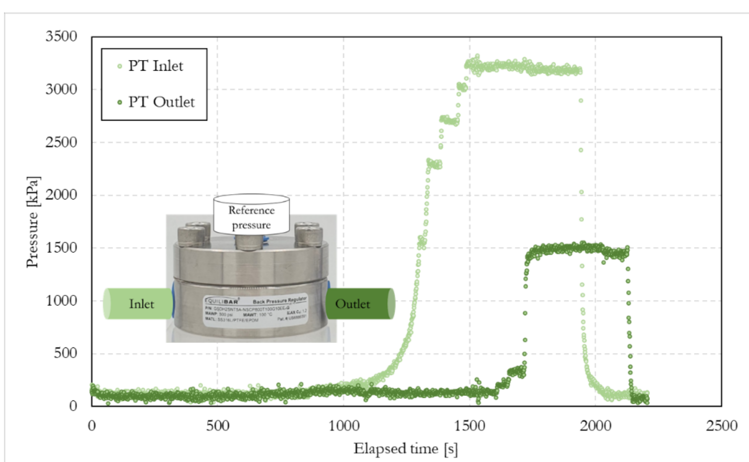

Fig 8-29. BPR2 at 1G

BPR2 tests at 30Gs

Using the setup that is described in Fig 8-24, the BPR2 is subjected to an enhanced gravity of 30 G's and tested. The results of multiple cycles of tests are shown in the Fig 8-30.

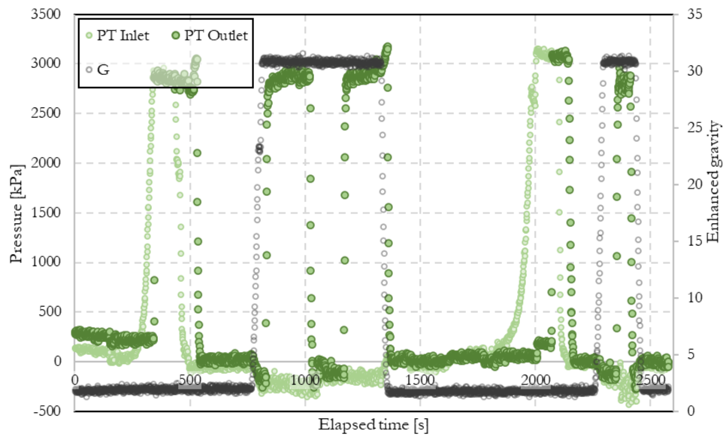

Fig 8-30. Test 1 at 30G's of the BPR2

Fig 8-30 shows multiple tries to make the BPR2 works under enhanced gravity. The first peaks of pressure are related with a test at 1 G which is successful and similar to the one shown in Fig 8-29. When the whole system is accelerated until 30G's, the BPR2 is not reliable exhibiting a behavior in which the outlet pressure increases even when the inlet pressure is constant. To ensure the conclusion, a second test was conducted, this time adding more room for possible fluid production. This leads to the conclusion that the BPR2 cannot be employed for the tests.

References

[1] "The Role of Solenoid Valves in Pneumatic and Hydraulic Power Systems." [Online]. Available: https://www.saferack.com/glossary/solenoid-valves/.

[2] Equilibar, "Definition of Back Pressure Regulator." [Online]. Available: https://www.equilibar.com/back-pressure-regulators/how-it-works/bpr-definition/.

Appendix B

Appendix B:

Commissioning tests

This appendix presents the procedure, results, and main conclusions obtained from the commissioning tests. The purpose of these tests is to verify the functionality of the cell as a complete system, rather than focusing on individual components, which are typically addressed during callibration. The tests are designed to be relatively straightforward but involve the simultaneous operation of multiple devices and sensors under enhanced gravity conditions.

First Precommissioning Test

In this commissioning test, the focus is on ensuring the proper functionality of the cell as a whole system rather than testing individual components. The objective is to evaluate the performance of multiple devices and sensors operating under enhanced gravity conditions. The test procedure is designed to be straightforward, yet it involves the coordination of various components.

One crucial aspect is the installation of five pressure transducers within the cell, with four positioned underneath the sample chamber and one located in the sandtrap. These transducers provide important measurements of pressure during the test. Additionally, external pressure transducers are strategically placed to monitor the pressure in the lines connecting the Parker motor with the stress actuators.

The first step involves assembling the sandtrap and sample plate, ensuring the proper sealing of the o-rings to maintain the integrity of the system. Subsequently, the GeoTriax, a containment vessel, is filled with water, approximately 50 kg in quantity. The purpose of using water in this test is twofold: it reduces the amount of gas required for pressurization, making the process more cost-effective, and water provides better traceability compared to gas. Fig 9-1 illustrates the GeoTriax filled with water, representing the completion of this step. The accompanying Fig 9-1 serves as a visual reference, depicting the Geotriax filled with water as a crucial part of the commissioning test.

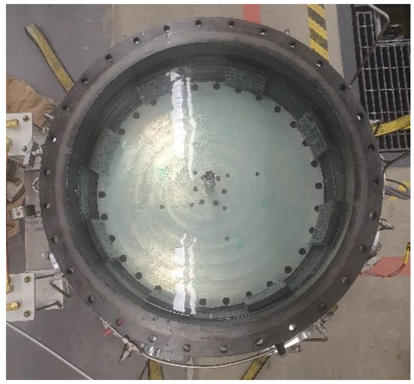

Fig 9-1. GeoTriax full of water.

Then the GeoTriax is closed and pressurized at about 2 MPa through injection of nitrogen to the main chamber. A picture of the process is shown in Fig 9-2.

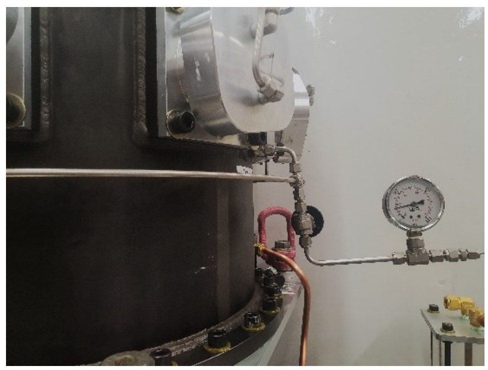

Fig 9-2. Pressurization of Geotriax with nitrogen.

Once the fluid inside is pressurized, the Geotriax is placed into the pit, and all the sensors and devices are connected and ready to spin as can be observed in Fig 9-3.

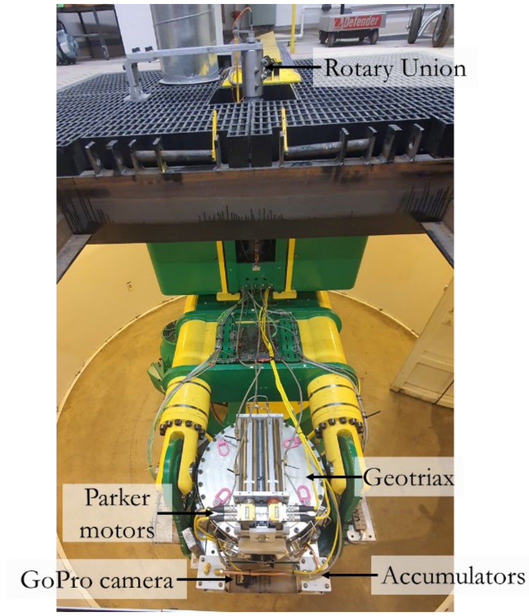

Fig 9-3. General setup after placing the GeoTriax at the pit.

After filling the GeoTriax with water, it is left undisturbed for one hour while closely monitoring the pressure inside the sample chamber. This step aims to ensure that no leakage occurs, and that the system maintains its integrity. The pressure monitoring is conducted under 1G conditions.

Once the one-hour period elapses, the spinning process begins, gradually accelerating the GeoTriax from 1G to 30G. During this phase, the stress actuators exert pressure against the water, simulating the conditions experienced during the test. Additionally, the wellbore sand filter is remotely adjusted as necessary. To control the flow of water, a slight release of the reference pressure is applied to the back pressure regulator. This enables a controlled flow of water into the external accumulators, contributing to the overall functionality of the system.

The results of these tests are summarized in Fig 9-4, which illustrates the evolution of the pressure inside the GeoTriax throughout the entire process. The graph provides valuable insights into the behavior and performance of the system under the varying gravitational forces experienced during the test. In Fig 9-4 different stages of the tests are numbered as follow:

1. Pressure build-up with nitrogen.
2. Test of seal.
3. Aceleration from 1 to 30G.
4. Spin at 30G without production.
5. Production trhough the back pressure regulator.
6. Slow down from 30G to 1G.

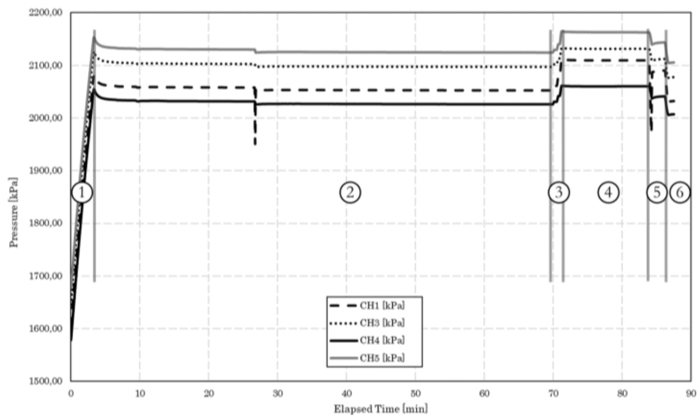

Fig 9-4. Pressure within Geotriax during the cell. Numbers refer to different stages of the test. CH5 is located in the sandtrap while CH1, CH3, CH4 are in the sample plate.

The pressure behavior observed during stage 2 provides compelling evidence of a robust seal, as no pressure leakage is detected from the sample chamber to the sandtrap. To highlight the impact of enhanced gravity, a closer analysis is conducted from stage 3 onwards until the conclusion of the experiment, as depicted in Fig 9-5. This detailed examination allows for a more nuanced understanding of the pressure dynamics within the system.

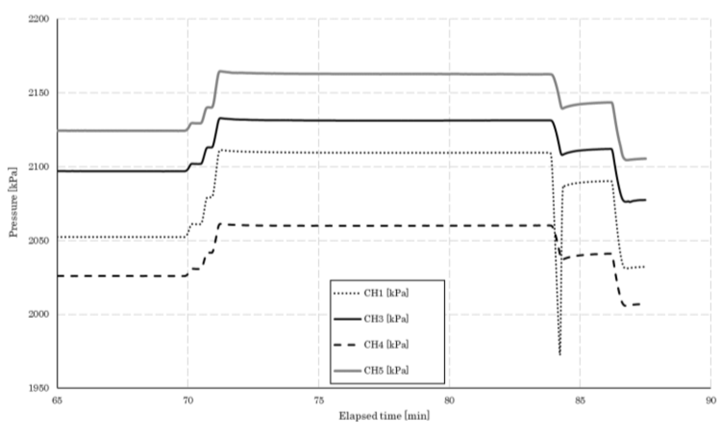

Fig 9-5. Zoom up to the pressure behavior during the spinning.

Until minute 70, the pressure readings from sensors CH1, CH3, and CH4 remain remarkably constant and nearly identical, with only a 3.5% difference observed between CH3 and CH4. It is worth noting that CH5, positioned below the other channels, exhibits a slightly different pressure profile. However, overall, the pressure remains stable during this period.

At minute 70, the spinning commences with staggered acceleration levels of 9G, 20G, and 30G. As the acceleration increases, the contribution of the water's weight to the overall pressure becomes more pronounced. Assuming a water density of 1kg/m³ (albeit a rough estimation considering the dissolved nitrogen and small bubbles present in the water), the expected pressure increase due to acceleration is approximately 54kPa. Remarkably, the observed pressure difference after acceleration is 38,478 kPa, which closely aligns with the anticipated value.

Around minute 84, the back pressure regulator is adjusted to initiate a water production interval lasting approximately 30 seconds. Following the production phase, water flow ceases, and the GeoTriax continues spinning. Finally, at minute 86, the centrifuge comes to a stop. **Fig *9-6*** provides a visual representation of the water produced during this interval, amounting to approximately 245 cm³.

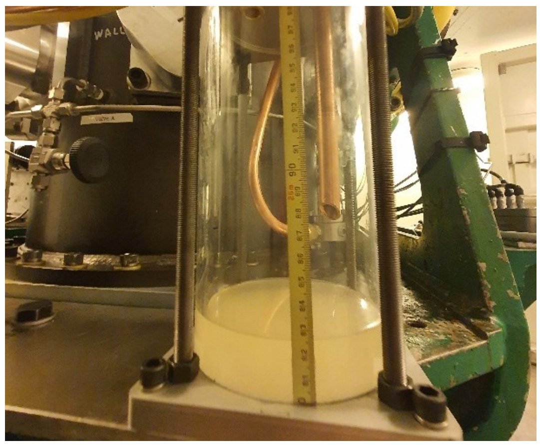

Fig 9-6. Produced water. Its color is due to the presence of little bubbles of nitrogen.

Following the completion of the test, a thorough inspection of all components is conducted, including the GeoTriax. Upon examination, it is discovered that during the initial test, the wellbore was not properly opened due to insufficient pressure applied from the surface. As a result, it is determined that a second commissioning test is necessary to rectify this issue and ensure the proper functioning of the system.

Second Precommissioning Test

This test is specifically designed to validate the functionality of the wellbore while the system is in a spinning state. The GeoTriax within the cell is filled with water and pressurized to the same level as in the previous pre-commissioning test. Once pressurized, the GeoTriax is carefully placed within the centrifuge mesh and the spinning process is initiated. During the spinning phase, the wellbore is activated by introducing pressurized nitrogen at a consistent pressure of 3.5 MPa. The pressure following of this test is depicted in Fig 9-7, providing representation of the entire process. Fig 9-7 provides a clear illustration of the wellbore's functionality during the test. At approximately minute 35, there is a noticeable increase in hydrostatic pressure, as indicated by the sensor located in the sandtrap. This increase signifies the successful opening of the wellbore. Furthermore, after the test is completed, a thorough visual inspection is conducted. The inspection confirms that the wellbore is indeed open, visually validating the proper functioning of the aperture mechanism.

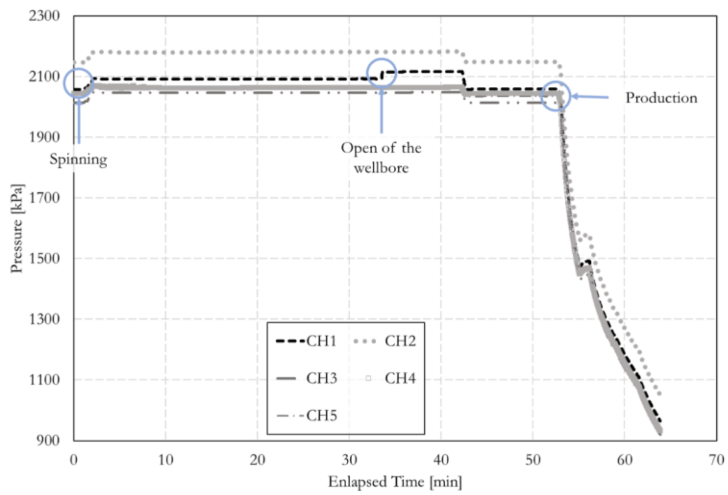

Fig 9-7. Pressure during the spinning

Fig 9-8 visually represents this inspection process, providing additional evidence of the wellbore's successful operation.

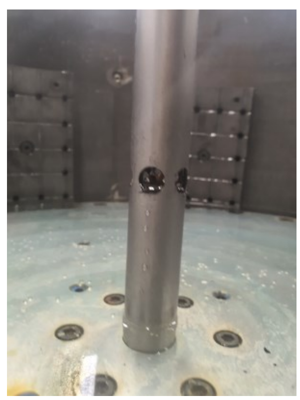

Fig 9-8. Opened wellbore after spinning.

Commissioning of the membrane

The final element to be commissioned, considering its importance, is the membrane. To carry out this test the cell is filled with water, and a metal lid is placed over it to allow a solid and even contact with the membrane (Fig 9-9). Over the lid, the membrane is assembled, and the upper chamber is pressurized with nitrogen while the pressure is followed by pressure transduces that are sensing the main and upper chambers.

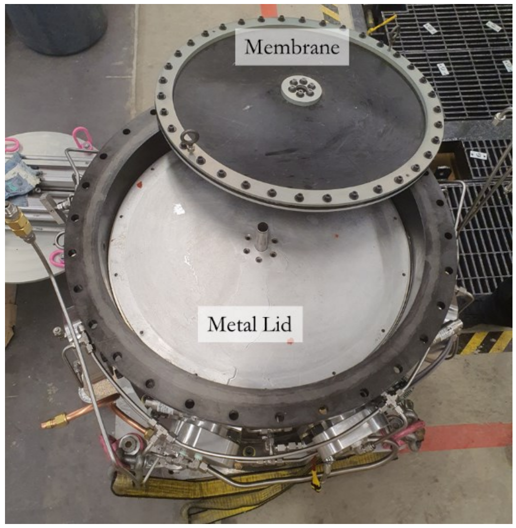

Fig 9-9. General setup to commission the membrane.

As a result, it was possible to confirm that the membrane kept the seal and pressure difference between the upper and main chamber. However, due to an overpressure in the upper chamber, the membrane was able to displace water and the metal lid sheared the screws attached to the stress actuators (Fig 9-10).

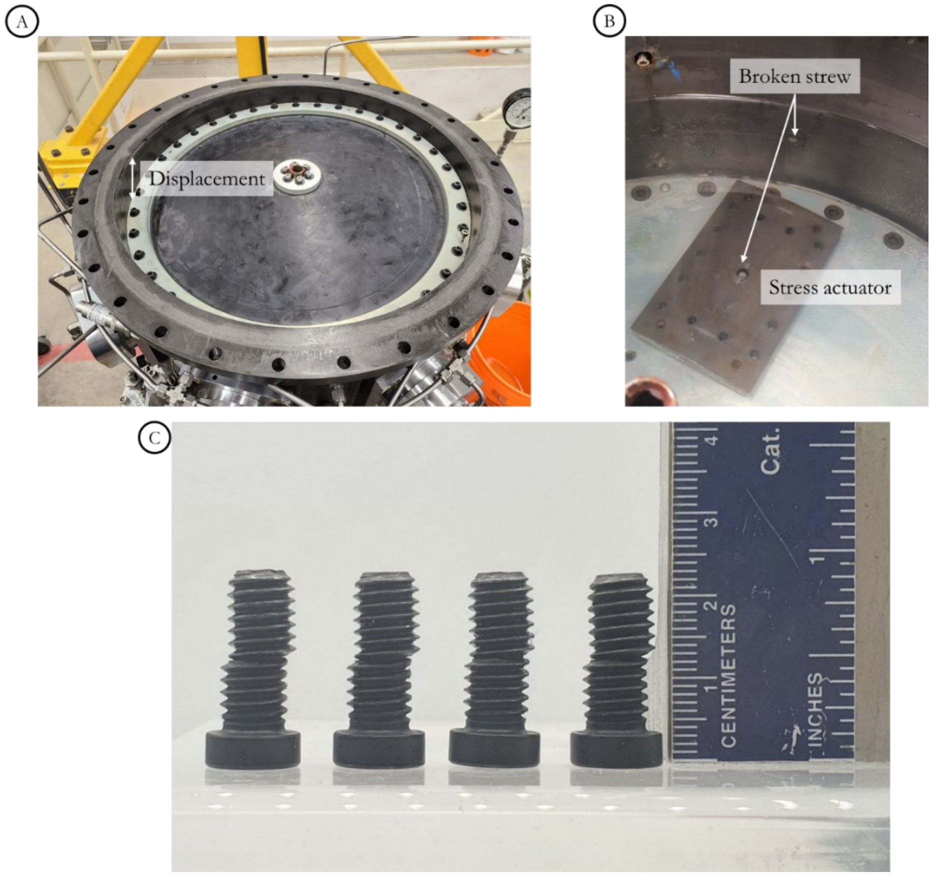

Fig 9-10. a) Membrane after the commissioning test, b) detached stress actuator due to a broken screw, and c) screws with a shear plane (approx. at 1,2 cm)

After the test, those elements were replaced and a bigger control in the possible displacement of the membrane was strongly suggested.

Appendix C:

Standard Operation Procedures

This appendix presents the procedures that were followed during the saturation at 1G and depetion at 30G using the GeoTriax cell. It is important to mention that these procedures were used as a guide and slight changes during the actual test coulb be implemented. It is important to note that this documents are a step-by-step guide and their structure is adaptated for a simple consultation during the experimental labor.

Saturation

General

This SOP details the procedure to saturate a 3D printed sample that represents the post-CHOPS reservoir with CO2-CSI recovery into the centrifuge facility. A post saturation procedure is presented in another SOP.

General Safety Precautions

High levels of CO2 are dangerous for human health.

Calcium Hydroxide is classified as hazardous under the Hazardous Product Regulation. It may cause severe skin burn, respiratory irritation, and eye damage.

There are four main routes by which a chemical can enter the body: oral, skin, ingestion, and inhalation. If an individual is exposed to an excessive concentration of any chemical, undesirable health effects can result.

Summary of sample preparation and saturation at 1G:

The test cell is assembled, and the 3D printed rock is placed inside.

Saturating sample with CO_2

Saturating sample with water

Induction of stress anisotropy

Saturating sample with dead oil

Saturating sample with live oil

Apparatus

Centrifuge cell

Pore pressure transducers

Pump type: Quizix pump 600

Fluid Accumulators

Valves

Back pressure regulator

Carboy

Miscellaneous tools, markers, tapes, etc.

Test Specimens

Test specimen will be 3D printed in GeoPRINT to contain the discontinuities of post-CHOPS reservoirs (e.g., wormholes). Because of size limitation of 3D printer, the specimen (CHOPS physical model) will be a modular sample 3D printed in multiple parts; it's not an individual piece of rock. Then it will be assembled in the lab prior to centrifuge test. A picture of the sample can be seen below:

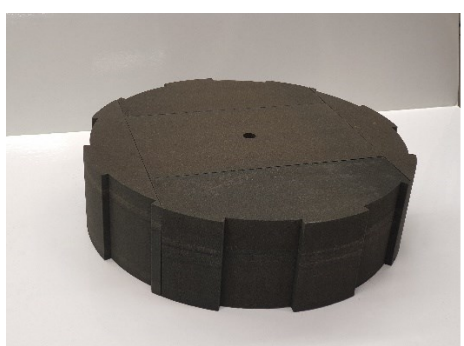

Pre-Preparation Calculations

To calculate the volume of the sample and approximate pore volume a spare sample will be used. The volume of the sample is calculated with the software Inventor for a total of 0.03262m^3 (32 L) with a relative error of 0.000212% and a porosity of 35,7% (For samples at 10% binder).

The porous volume (PV) is calculated bellow:

$$V_p = V * \varphi = 32L * (35{,}7\%) = 11{,}4\ L\ or\ 0{,}0114\ m^3$$

It's important to consider that the sand trap has a volume of approx. 5L that should be count for displacement calculations.

Procedure

Sample placed within the centrifuge cell.

Verify that all the stress actuators of the cell are not extended. Use a rubber mallet to push stress pistons back to their initial place.

Place the central part of the specimen (3D printed sample).

Indicate with a permanent marker over the walls of the tub the direction of the wormholes.

Place the other modules of the specimen (3D printed pieces) from central modules to external one.

Place the membrane on top part of the tub

Fix the top part of the tub.

Saturation with CO_2 at 1G.

Confirm that all the valves shown in Figure *1* (A, B, C, D, and F) are closed

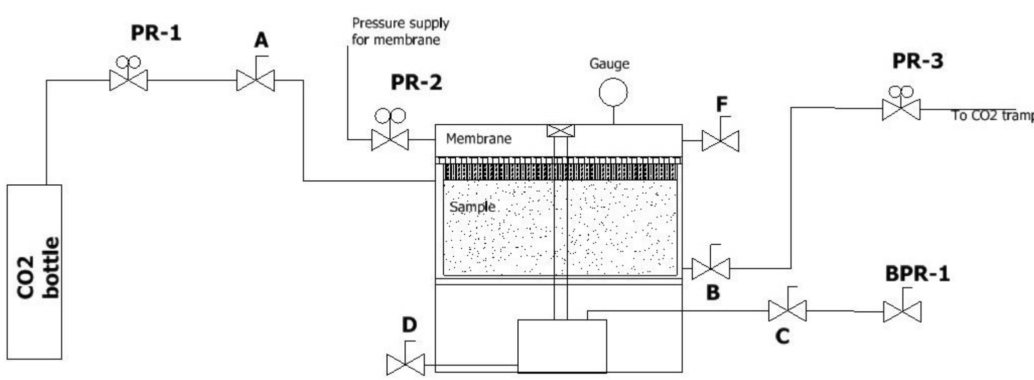

Figure 1. Diagram of CO_2 saturation

Open the valve A for CO_2 to flush the sample. Use PR-1 to slowly increase the pressure to 400 kPa. The injection is suggested to occur through multiple points at the top of the sample. Inject 1,2 PV approx. (13,68 L).

Close the valve A and check for any leaks. Detect leaks by analysis the pore pressure within the cell. No substantial decreases should happen. Neither any kind of increase of the pressure should happens in the membrane chamber.

If no leaks are detected, set PR-3 valve reference pressure to 500 kPa

Open the valve B.

Set PR-3 slowly at 300 kPa to allow the flow. Let the CO_2 and air/N2 to bubble into the solution of water with $Ca(OH)_2$ to absorb until the system pressure reaches 300 kPa. Some change in the color of the solution to white may occur.

To prepare the solution of $Ca(OH)_2$ keep in mind that $Ca(OH)_2 + CO_2 \text{->} CaCO_3 + H_2O$.

We can use the ideal gas law to calculate the number of moles of CO2:

$$n = PV/RT$$

n = PV/RT

where P = 3.947 atm, V = 13.68 L, R = 0.08206 L·atm/mol·K (gas constant), and T = 294.15 K.

$$n = 0,6592\ mol$$

To calculate the mass of CO2, we can use the molar mass of CO2, which is approximately 44.01 g/mol:

$$mass = 0,6592\ mol * 44.01\ \ g/mol = 28,99\ g$$

Since 1 mole of Ca(OH)2 reacts with 1 mole of CO2, we need 0.6587 moles of Ca(OH)2 to react with 0.6587 moles of CO2. The molar mass of Ca(OH)2 is approximately 74.09 g/mol, so the mass of Ca(OH)2 we need is:

mass(Ca(OH)2) = n(Ca(OH)2) x molar mass(Ca(OH)2)

mass(Ca(OH)2) = 0.6587 mol x 74.09 g/mol

mass(Ca(OH)2) = 48.86 g

Close the valve B

Adjust PR-3 valve at 1500 kPa and PR-2 valve at 750kPa.

Supply pressure through PR-2 valve into the membrane region to create the confining stress.

Open the valve A

Increase the pressure of the PR-1 slightly until the cell pressure reaches 500 kPa.

Close the valve A.

Open the valve B and decrease slowly the valve PR-3 to 400kPa. Let the CO_2 and air to bubble into the solution of water and $Ca(OH)_2$ until the pore pressure reaches 400kPa.

Close valve B

Adjust PR-3 valve at 600 kPa

Set PR-2 valve at 1500 kPa.

Supply pressure into the membrane region through PR-2 valve.

Open the valve A, and slowly increase PR-1 until the cell pressure reaches 600 kPa. In this stage, the pore pressure of the specimen is 600 kPa.

Close the valve A

Open the valve B and adjust slowly the valve PR-3 to 500kPa. Let the CO_2 and air/N2 to vent to the CO_2 tramp until the system pressure reaches 500kPa. Thus, the pore pressure changes from 600 kPa to 500 kPa.

Close valve B

Check and make sure that there are no leakages of CO_2 through the valves and connections.

Saturation with water at 1G.

The following steps start with the system (Sample and sand trap) containing CO_2 at 500 kPa. Figure 2 shows the required setup.

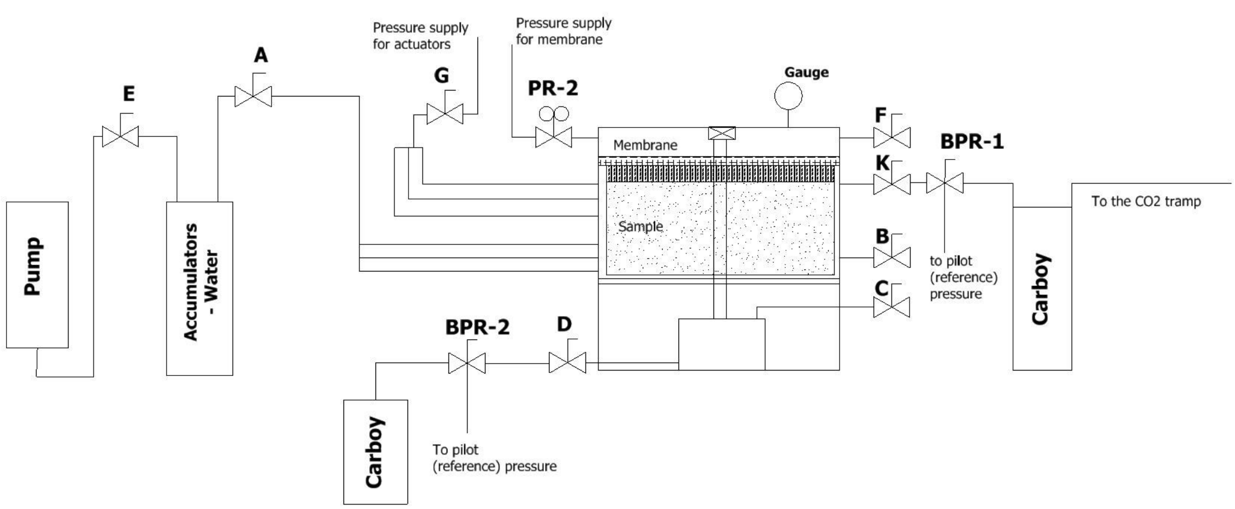

Figure 2. Diagram of the water saturation

Open valve E to connect the water accumulator with the Pump

Set the pump pressure at 1200kPa. The pump pushes the water into the system at low rate. The lowest rate possible is suggested at the very beginning of the saturation to avoid a fingering effect or erosion. To calculate this rate, the high of the injection port is taken as reference, it is at 1.524 cm from the sample's base which means a volume of 1140 cc that will be saturated in 1 hour which gives an flow rate of 19cc/min. The following table shows some rates and the time it would take to saturate the rest of the sample:

Table 10-1. Elapsed time at different rates.

Time elapsed [h]	**Rate [cc/min]**
2	110
3	73
4	55

Keep in mind that the maximum flow rate for the pump is 200 ml/min.

Adjust BPR-1 to 500 kPa (Same pressure that the one inside the sample).

Open valve K. Valve K should connect just one jet/port at the top of the sample to improve the sweeping efficiency

Open Valve A. Multiple jets or point of injection are strongly suggested to do a simultaneous saturation from different points at the bottom of the sample. Thus, valve A means the inlet for multiple jet points.

Vent the CO_2 into the CO_2 tramp while the water comes from valve A is injected at very low rate (See **Table *10-1.*** Elapsed time at different rates.). The maximum rate should not excess 200 cc/min.

Inject 1.2 Pore Volumes (Approx. 13.68 L) and monitor injected/produced water volumes. Additional water may be required to fill the sand tramp (Approx. 5.27L). To monitor the produced water, the use of a carboy is strongly suggested. Check that no sand must be produced into the carboy.

Increase BPR-1 to 900 kPa to stop the flow. And close valve K.

Increase confining stress to 1000 kPa with the valve G and PR-2 (membrane and lateral actuators)

To know the pressure, the pressure in the line can be used as is demonstrated by the relationship between the piston and the load cell

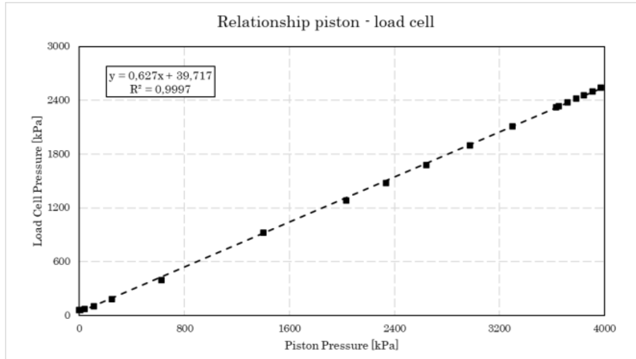

Increase pump pressure to 1000 kPa to change the pore pressure

Increase confining stress to 1500 kPa with the valve G and PR-2 (membrane and lateral actuators)

Increase BPR-1 to 1400 kPa.

Increase pump pressure to 1500 kPa to change the pore pressure

Increase the confining stress to 2250 kPa with the valve G and PR-2 (membrane and lateral jacks)

Increase BPR-1 to 1900 kPa

Increase pump pressure to 2000 kPa to increase the pore pressure

Make sure the cell pressure is stable in 1900 kPa.

Increase BPR-1 to 2000 kPa.

Increase pump injection pressure to 2100 kPa and produced 1.2 PV of water to do so, keep the record in the carboy. During this process, it is important to monitor and record the injected/produced water all the time.

Close Valve K and wait until pressure is stable at 2000kPa. Stop the pump during the stabilization.

Set BPR-2 at 2000kPa

Next steps until 8.59 are required if the PT inside of the cell are connected.

Open Valve D

Slowly reduce the back pressure with the BPR-2 to 1950kPa and take careful record of the produced amount of water for a limited short period of time (Time to no create a significant drawdown or higher that 100kPa). The first produced water is the one trapped into the sand trap (5.27L). After that volume, it is important to record the time and outcoming volume.

Estimate the permeability based on steady-state injection/production rates and inlet-outlet pressure records using the following equation:

$$k = \frac{q\mu \ln{(r_e/r_w)}}{2\pi h(P_e - P_w)}$$

Close Valve D

Inject water at 2100 at low rate to increase the pore pressure again to 2000kPa

Open the valve D.

Estimate the permeability based on steady-state injection/production rates and inlet-outlet pressure records using the following equation:

$$k = \frac{q\mu \ln{(r_e/r_w)}}{2\pi h(P_e - P_w)}$$

Close Valve D

Inject water at 2100 at low rate to increase the pore pressure again to 2000kPa

Estimate the porosity using the expression:

$$\varphi = \frac{V_{w,injected} - V_{w,produced}}{V_{sample}}$$

Close valves E, A, and K. The pore pressure within the sample is 2000 kPa at this point.

To Prevent sand influx into BPR-1 and BPR-2, slow rates are highly recommended.

Stress anisotropy if needed

Stress state is isotropic until this part and is 2250 kPa at membrane and stress actuators.

Increase the stress in the membrane (PR-2) at 2500 kPa

Open valve K and allow the drain of the excesses water pressure until pore pressure stabilizes again in 2000 kPa (with the back pressure regulator set at 2000 kPa).

Close the valve k

Saturation with dead oil at 1G.

In the Figure *3*, the sample is fully saturated with water, the pore pressure within the sample is 2000kPa, confining pressure by actuators is 2250kPa and vertical stress (membrane) is 2500kPa. All valves are closed. The sand trap is full of pressurized water.

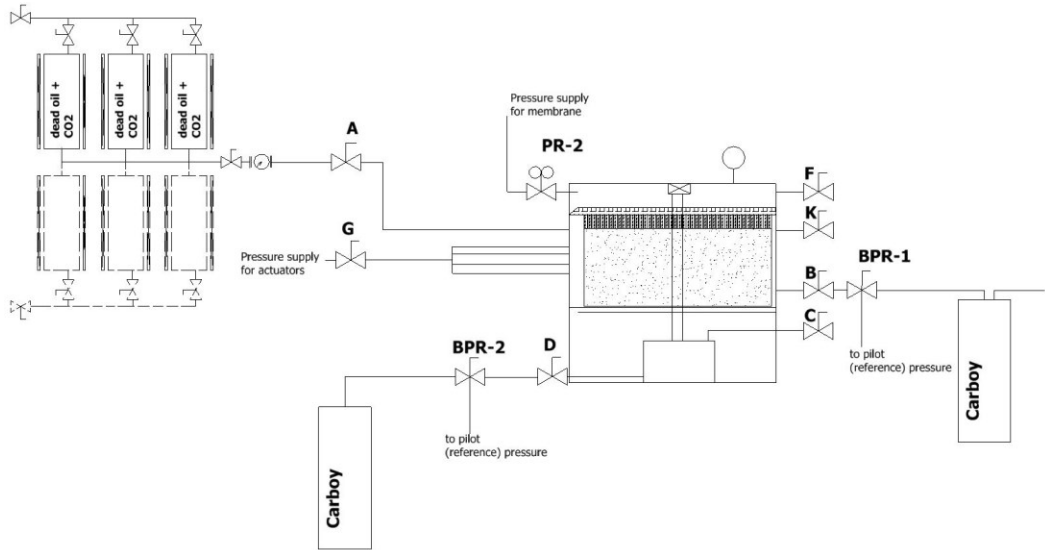

Figure 3. Diagram of Dead Oil Saturation

Fill the accumulators with approximately 32 L of oil. Warm the oil up until 40-45°C (Thermal coil) to allow a better displacement.

Set BPR-1 to 1900kPa. This line should be connected to just one port/jet at the bottom of the sample.

Set the pump A to maintain 2050kPa. A higher value could be required due to viscosity and length of the lines.

Open valve A

Open valve B

Open valve of the first dead oil accumulator

Start the injection of oil

Monitor and measure volume of produced fluids (oil and water) in the carboy after BPR-1.

Inject 1.2 PV (Approx. 11 L) of dead oil and estimate oil and water saturation. A 10% of water saturation is the target. DO NOT DISPOSE THE OIL; COLLECT OIL FOR OTHER MEASUREMENTS/REUSE IN EXPERIMENTS. The produced water should be 11,4L*0,9= 10,26L

Close valves of the accumulators A.

Adjust BPR-1 to 2400kPa to stop the flow. Close valve B

Since the sand trap is a place where some water may be tramped A second and short displacement is done through the BPR-2 and valve D

Adjust BPR-2 to 1900kPa

Set the pump A to maintain 2050kPa. A higher value could be required due to viscosity and length of the lines.

Open valve A

Open valve D

Inject slowly dead oil while carefully watching the Carboy after the BPR-2. The first fluid coming out should be water (Due to its higher density). Once a continuous flow of oil is obtained, the assumption of a fully oil- saturated sand trap is done, and the injection can stop.

Set BPR-2 at 2400 to prevent further flow. Allow the recovery of the pore pressure to 2000 kPa throughout the sample.

Stop the pump

Close valves of the accumulators A, and the sand trap (Valve D)

Saturation with live oil at 1G.

For this stage, all valves are closed, the confining stress is 2500 kPa in the vertical stress, 2250 in the horizontal stresses, and the pore pressure is 2000 kPa (Figure *4*). The sand trap is pressured and full of dead oil.

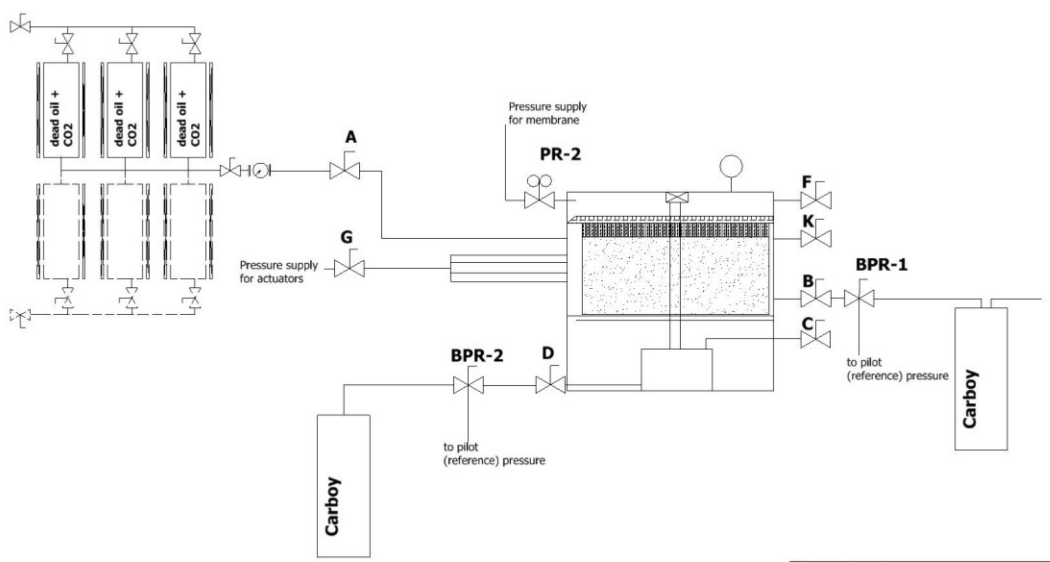

Figure 4. Diagram of Live Oil Saturation

Fill the accumulators with dead oil.

Add CO_2 to the accumulator under 4000 kPa based on PVT properties/mixing instructions of oil/CO_2 from supplier (e.g. CNRL). Wait for 1-2 hours until the pressure inside the accumulators decreases due to dissolution and increase again the pressure. To promote the mixing, spin the accumulator. If possible, take record of the time and decrease of pressure inside the accumulators.

Let the oil with CO_2 stay overnight to allow a fully CO_2 dissolution.

Set BPR-1 at 1900 kPa

Set the pump at 2000 kPa

Open valve B

Open valve A to allow the flow

Inject 1.2 PV (Approx. 13 L) of live oil. When live oil is coming out to the carboy, the separation of the CO_2 should be observable. It should look like little bubbles coming out of the oil.

Close valve A, B

Set BPR-2 at 1900 kPa

Set the pump at 2000 kPa

Open valve D

Open valve A to allow the flow

Inject live oil at slow rate to displace the dead oil that is in the sand trap. When live oil is coming out to the carboy, the separation of the CO_2 should be observable. It should look like little bubbles coming out of the oil.

Close valve A and D

Wait until the pore pressure is stable at 2000kPa.

Depletion

General

This SOP details the procedure to deplete the sample representing a post-CHOPS reservoir with CO_2-CSI recovery in the centrifuge facility.

General Safety Precautions

High levels of CO_2 are dangerous for human health.

There are four main routes by which a chemical can enter the body: oral, skin, ingestion, and inhalation. If an individual is exposed to an excessive concentration of any chemical, undesirable health effects can result.

Summary of sample preparation and testing methods

The sample is placed and saturated.

Check of the pore pressure

Primary depletion at 30G

Cycle 1 of CO_2 at 30G

Cycle 2 of CO_2 at 30G

Apparatus

Centrifuge

Sample cell

Pump

Valves

Test Specimens

Test specimens will be printed to contain the discontinuities of post-CHOPS reservoirs (Wormholes). The recommended saturation of binder is 5%

Pre-Preparation Calculations

From the saturation procedure, it is possible to know the interconnected pore volume as described in the SOP of saturation.

1. **Procedure**

Check of the pore pressure and anisotropy of stresses at 1G

Confirm that all the valves shown in Figure 5 (G, F, K, B, C, and D) are closed.

To check if there is any leak, confirm that all the pressures (Back pressure, horizontal stress, and vertical stress, membrane, and sandtrap) are constant

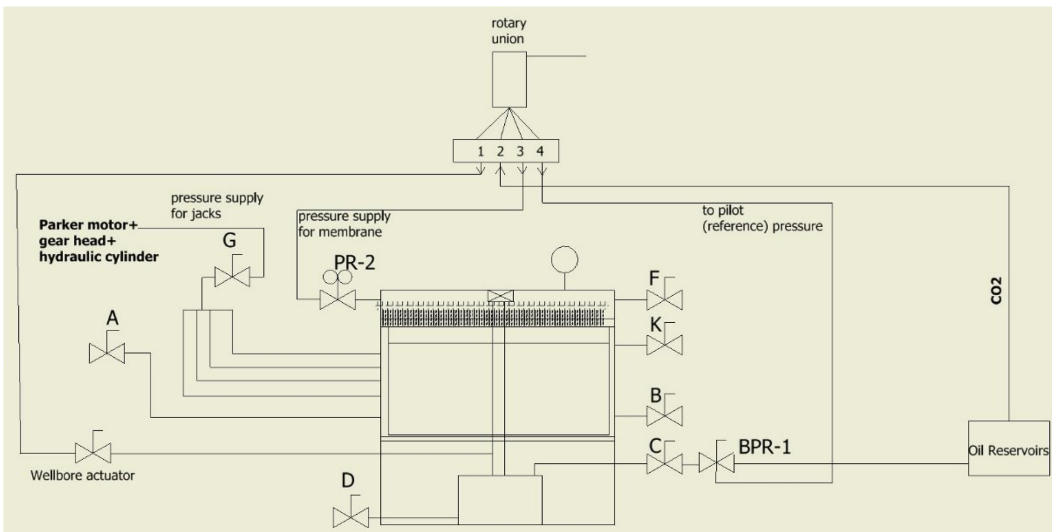

Figure 5. Diagram of centrifuge test

At this moment, the pore pressure should be 2000 KPa, the horizontal stresses at 2250 kPa, and the vertical stress is 2500kPa.

Primary depletion at 30G

Begin the flight of the centrifuge at 120 rpm to obtain 30G

Set BPR-1 at 200 kPa

Activate the actuator to retrieve the wellbore plug

Open valve C to allow the flow

Close valve B when the pressure in the sandtrap when the pressure inside is equal to 250 kPa or lower for a period longer than 15 min.

Cycle 1 of CO2 at 30G

Confirm that all the valves shown in Figure *1* (A, B, C, D, and F) are closed

Open the valve A increasing slowly the pore pressure of the cell to 2000 kPa (PR-1) with CO_2. This is the CO_2-reservoir pressurization

Close the valve A

Keep the cell in soaking during the whole night

Set BPR-1 at 200 kPa

Open valve C to flow

Measure the amount of oil, water, CO2, and sand during the whole process (If possible

Close valve B when the pressure in the sand trap when the pressure inside is equal to 250 kPa or lower for a period longer than 15 min

Cycle 2

TBD

Depressurization of the cell

Stop the centrifuge

At the end of the final cycle, the centrifuge is stopped, the Pore Pressure is 200kPa, and the confining stresses are 2500 kPa and 2250 kPa values

Open the valve F and allow the whole pressure of the membrane to be dissipated. This would let the vertical stress to zero.

Let valve F open

Open the valve G and allow the whole pressure of the pistons to be dissipated. This would let the horizontal stresses to zero.

Let valve G open.

To depressurize the sample, open the valve K. The pressure is 200kPa (twice the atmosphere) so no hazard is produced. If multiple production cycles are done, let the last one to drawdown until 120kPa

Disassembly the cell. Opening the main chamber where the sample is placed.

Analysis of the sample

For each test, the analysis can vary*. The following instructions are general

Place the centrifuge cell over a stable surface and white background.

Place the camara perpendicular to the sample surface. The use of a tripod is strongly suggested

Take a picture of the initial or top surface.

Begin with horizontal or vertical cuts depending on the analysis to examinate the distribution of saturation. The cuts should be at 1 cm each other

Take pictures at each cut. Try to keep the perpendicularity of the camera

Separation of oil in the external containers

This separation will be based on the density difference between oil and water.

Drain the contented fluids into a graduated beaker previously weighted.

Wait 1-2 hours until the phases dissociate by gravity.

Separate the phases with the help of a syringe.

Weight both fluids

Separation of sand from the sand-trap

Open the sand-trap.

Take the produced sand with fluids into a graduated beaker

Weight the produced sand and fluid that were into the sand trap. This weight is Wt

Let the mixture of sand and fluids dissociate by gravity.

With the use of a syringe, separate the excessive oil that is over the sand and measure it. This is Wo

Apply 500 mL of hot water to the "Dirty" sand. In this step, dirty sand means the sand that is mixed with oil.

Let the mixture of sand and fluids dissociate by gravity.

With the use of a syringe, separate the excessive oil that is over the sand and measure it.

Check if the sand is clean. If not, repeat the previous three steps.

Once the sand is clean, separate the sand and the water.

Weight the sand. This is Ws

To calculate the amount of original water, the following subtraction is done:

$$W_w = W_t - W_s - W_o$$

Appendix D:

Tests that went wrong

In this appendix, some of the tests that went wrong are shown. The main purpose of this appendix is to report some learning that helped to improve the final desig of the GeoTriax.

Try 1 – Unstable membrane

During this try, the SOP for saturation was followed until the test failed. Following the SOP, the sample was flushed with CO_2 to remove the air in the sample, after which the saturation with water happened.

The saturation with water is basically a miscible displacement in which the water displaces the CO2 from jet ports that are at the base of the main chamber to outlet ports at the top. This displacement pattern looks for avoiding any gravitational segregation. To have a tracing mechanism, a CO2 trap is integrated at the outlet (Fig 11-1).

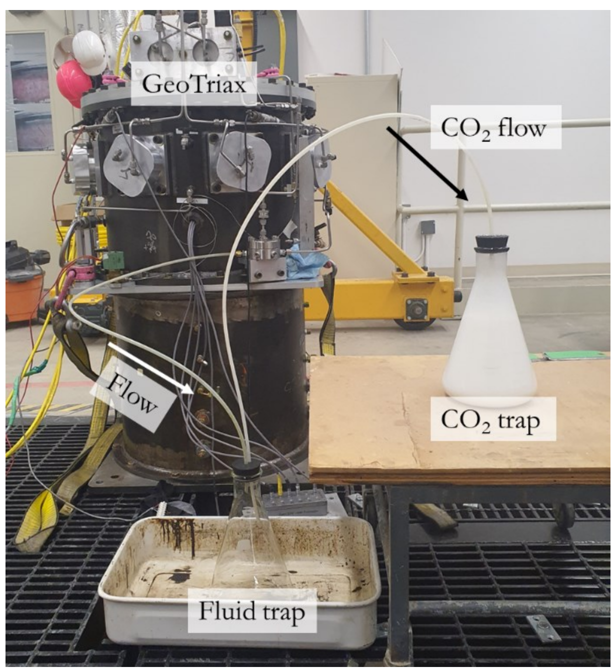

Fig 11-1. Setup and CO_2 trap

During this test, the CO_2 flush was done successfully following the SOP for saturation. After it, the saturation with water was initiated and the most of the CO_2 evacuated from the sample. However, after

2 hours of saturation, the pressure of the upper chamber and the main chamber begins to get equalized until both of them were in equilibrium, which means that some kind of leak occurred and the fluids scaped from the main chamber.

At this point, the test was stopped, and the cell opened for inspection (Fig 11-2-right). It was found that the upper chamber that should be dry (Since it contains just pressurized nitrogen) was "flooded".

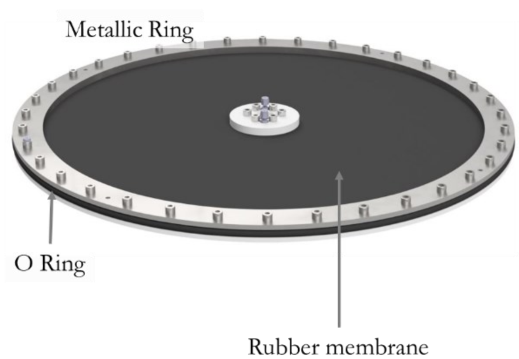

Fig 11-2. (left) Diagram of the membrane and its parts. (right) Upper chamber during after the failed test.

As it can be seen in the description of the membrane (Fig 11-2-left), the sealing is done by an o-ring that goes all the way around the metallic ring. The performance of this o-ring relies on a tight contact against the metal wall of the cell. After inspecting the cell, it was found that during the saturation, the membrane slightly tilted over the sample leading to the reduction of the contact area for the o-ring.

To solve this issue, it is important to keep the membrane as horizontal as possible. To achieve that, a set of bolts were placed in the metallic ring. It way, when the membrane tries to tilt, the bolts at the opposite side will prevent the movement because they are pushed back by the top lid of the cell (Fig 11-3).

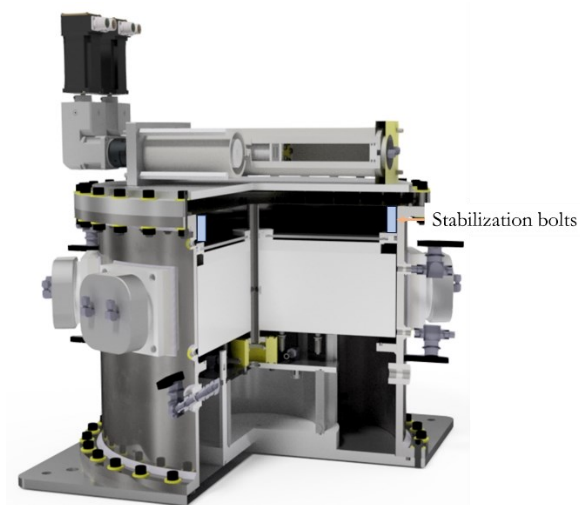

Fig 11-3. GeoTriax and the position of the Stabilization bolts

Try 2 – Infiltration by the wellbore.

In this test, the stabilization bolts were already in place. The saturation SOP was followed but during the saturation with water and after the first step of vertical stress was applied, the pressures inside the main chamber and the main chamber entered in connection through a leak and the pressure from the upper chamber contribute to the pore pressure. To assess the cause of this, the test was stopped, and the cell was opened. The membrane showed a convex deflection due to the accumulation of nitrogen beneath it (**Fig *11-4*** left). A second observation is that the membrane is dry, which means that the stabilization bolts helped to prevent the inclination of the membrane. Finally, a close look at the membrane reveals a set of microcrack or stretching masks in the membrane (**Fig *11-4*** right).

Fig 11-4. (Left) Membrane in a convex form. (Right) Micro cracks in the membrane.

To solve this issue, an extra layer of silicone seal (blue mark in the **Fig *11-4***) was applied in the crack and around the edges between metal parts and the rubber membrane. This procedure allowed better sealing in the coming tests.

Appendix E

Appendix E:

Printer Issues

In this appendix, some of the main issues regarding the printing process that resulted in imperfect samples are presented.

1. Samples with protuberances

This appendix descriptives the multiple issues and procedures regarding the quality of the printings.

Before carrying out the printing process of the sample, several prints are made allowing to get an assessment of the printing quality and some sample for other projects of the group. Those preliminary prints were carry out with layers of 250 μm, 20% of saturation, room humidity between 24-28%, and D_{50} of 175μm. Under such conditions, a competent sandstone is obtained, it means a cohesive rock.

Fig 12-1 shows the samples printed. Most of them are designed for triaxial tests with dimension of 6 cm by 3 cm of diameter. From both pictures, it is evident than there is a region of the jobbox that is producing low/poor quality samples meanwhile a set of samples during the same printing have a an aceptable/good quality to be considered 3D printed sandsotones.

Fig 12-1. Quality of different samples sorted by their position into the job-box.

The poor quality of the samples in this case relies on the irregular shape of the samples. Ideally, all the samples should be a perfect cylinder, this is one of the advantages of 3D printing [1]. A zoon up of the irregular protuberances on the samples is shown below:

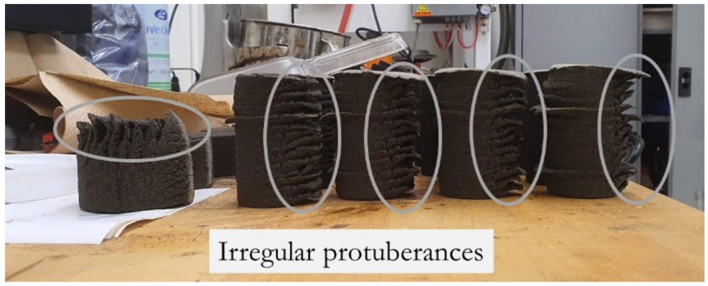

Fig 12-2. Zoom up to poor quality samples.

From Fig 12-1, it is evident that the source of the problem is regarded with the hardware. A software issue was excluded since several samples (located in the same region of the job-box) have a good quality, which means that it is not a systematic problem that could affect every sample from a software problem.

Aditional to this implication, an observation of the printing showed a drag phenomenon when the roller and recoater come back to their initial position (Fig 12-3).

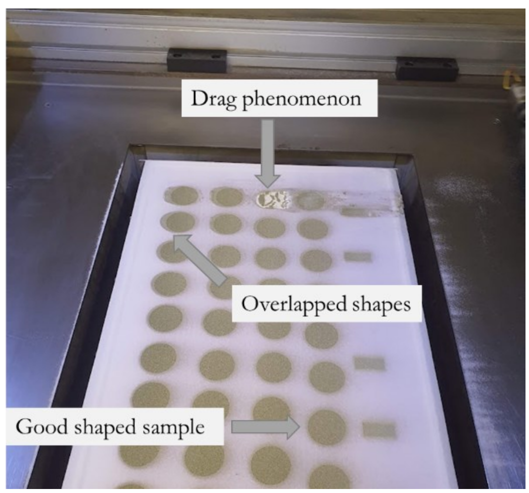

Fig 12-3. Dragging and overlapping during the print process.

After a general instection to the printer to find out the cause of the protuberances on the samples, a slight tilt is found in the roller. It means that everytime the roller passes over the sample, there is an area of higher surface contact and force where the fresh binder is squeezed. To sort out this issue, an alightment of the roller was done, leving the surface of it with the job-box.

References

[1] L. Kong, S. Ishutov, F. Hasiuk, and C. Xu, "3D Printing for Experiments in Petrophysics, Rock Physics, and Rock Mechanics: A Review," SPE Reservoir Evaluation & Engineering, vol. 24, no. 04, pp. 721–732, 2021.